Soil Structure Interaction of High-Speed Trains Over Soil Metal Bridges

by

Alaa Metwally

Submitted in partial fulfilment of the requirements
for the degree of Master of Applied Science

at

Dalhousie University
Halifax, Nova Scotia
December 2023

Dalhousie University is located in Mi’kma’ki, the
ancestral and unceded territory of the Mi’kmaq.
We are all Treaty people.

TABLE OF CONTENT

LIST OF TABLES iv
LIST OF FIGURES v
ABSTRACT viii
LIST OF ABBREVIATIONS AND SYMBOLS USED ix
ACKNOWLEDGEMENTS xiii
CHAPTER 1 INTRODUCTION 1
  1.1 Research Background 1
  1.2 Problem Description 6
  1.3 Research Objectives 6
CHAPTER 2 LITERATURE REVIEW 8
  2.1 Soil Metal Bridges 8
    2.1.1 Terminology and Standardization 9
    2.1.2 The Significance of Geotechnical Investigations 11
    2.1.3 The Structural Resilience of Corrugated Metal Bridges 14
    2.1.4 CHBDC Design Criteria 27
    2.1.5 Dynamic Methods of Analyses 32
    2.1.6 Eurocode Approach 32
  2.2 Cellular Confinement Systems CCS 42
CHAPTER 3 SOIL-STRUCTURE INTERACTION OF HIGH-SPEED TRAINS OVER SOIL METAL BRIDGES 64
  3.1 Introduction 64
  3.2 The Considered Field Study 66
  3.3 Finite Element Model Development 68
    3.3.1 Soil Profile and Compaction Procedures Techniques 68
    3.3.2 Compaction Measures and Procedures 71
    3.3.3 Compaction Simulation 75
  3.4 Corrugated Steel Plates Modeling 77
  3.5 Model Validation 81
  3.6 Soil Cover Impact on Dynamic Train Loads Parametric Study 84

3.6.2 Soil And Material Properties 88
3.7 Parametric Study Results 92
3.7.1 Crown Deformation 92
3.7.2 Thrust Force 103
3.7.3 Bending Moment 105
3.8 Conclusion 108
CHAPTER 4 SOIL-STRUCTURE INTERACTION OF HIGH-SPEED TRAINS OVER GEOCELL REINFORCED SOIL METAL BRIDGES 110
4.1 Introduction 110
4.2 Three-Dimensional Modeling in Analyzing Culvert Behavior 111
4.3 Numerical Modelling 118
4.3.1 Geocell Numerical Modelling 118
4.3.2 Numerical Modeling of Honeycomb Geocell 121
4.4 Parametric Modeling and Conditions 123
4.5 Results and Discussions 126
4.5.1 Crown Deformation 126
4.5.2 Crown Accelerations 132
4.5.3 Thrust Force 139
4.6 Conclusion 142
CHAPTER 5 CONCLUSION 145
REFERENCES 147

LIST OF TABLES

Table 2.1 Soil classification based on ASTM D2487 2006. 12

Table 2.2 Secant modulus of soil values for various soil groups and different Standard Proctor densities in accordance with ASTM D698 (2007). 13

Table 2.3 The variables α, β, and μ based on Elsameili (2013) calculation......................... 19

Table 2.4 Restrictions on conditions and factors related to material resistance. 28

Table 2.5 $K4$ values for live load calculations. 31

Table 2.6 Damping values based on SS-EN 1991-2:6.4.6.3.13 35

Table 2.7 Train model HSLM-A base on SS-EN1991-2:6.4.6.1.14 37

Table 3.1 Employed soil Material properties in Webb 1999 field test. 67

Table 3.2 Equivalent plate material properties. 80

Table 3.3 Soil Material Properties. 89

Table 3.4 Properties of a UIC 60 rail. 91

Table 4.1 Weak soil material properties 124

LIST OF FIGURES

Figure 1.1 Baltic Road Arch at Trans Canada Highway, Clyde River, PEI 2

Figure 2.1 Train passing over a SMB (A. Andersson et al, 2012) 9

Figure 2.2 Visualization of the terminology related to soil-steel bridges. 11

Figure 2.3 Variation of E_s with Standard Proctor Density for Different Soil Groups 14

Figure 2.4 Definition of span S and Rise D for various conduit shapes. 17

Figure 2.5 Thin steel ring supports relatively large, concentrated load when confined right, but easily flattened when unconfined left. (White and Tayler, 1960) 22

Figure 2.6 Relationships between $Af, H/D, and\ D/S$ 31

Figure 2.7 A additional damping Δζ % as a function of Span length L m based on SS-EN 1991-2:6.4.6.44. 36

Figure 2.8 A representation of geocell reinforced Soil Metal Bridge. 48

Figure 2.9 A representative of a honeycomb Geocell layout. 50

Figure 2.10 Schematic representation of geocells with different pocket shapes. 53

Figure 2.11 Different geocell fabrication patterns. 54

Figure 2.12 A representative illustration of a multi-Geocell reinforced Soil metal bridge........ 59

Figure 3.1 Cross-section view of the Full-scale field test after Webb 1999............................ 67

Figure 3.2 Schematic illustration of the three approaches for simulating compaction effort by McGrath et al 1999. 72

Figure 3.3 Backfill layers compaction sequence. 77

Figure 3.4 5-gauge 5.5-mm corrugated steel profile (CSPI, 2007). 79

Figure 3.5 Deformation-compaction curves of Webb field results and the developed plaxis3D model.. 83

Figure 3.6 Hoop compression curves of Mark C. Webb field results and the developed plaxis3D model. 84

Figure 3.7 CRH 380A profile.. 86

Figure 3.8 Three-dimensional structural representation of plaxis3D model. 88

Figure 3.9 Visual representation of the rail track. 91

Figure 3.10 Soil cover depth impact on the maximum crown deformation for various train traveling speeds. 94

Figure 3.11 Cross-sectional deformation of the Soil-Metal Bridge SMB at a speed of 300 km/h for soil cover depths of 2, 3, and 4 m with a scale magnitude of 1000. 96

Figure 3.12 A three-dimensional representation capturing the SMB deformations cycle at different time intervals as a high-speed train travel at 300 km/h over 2 m cover depth. 97

Figure 3.13 A three-dimensional representation capturing the SMB deformations cycle at different time intervals as a high-speed train travel at 300 km/h over 4 m cover depth. 98

Figure 3.14 Deformation of the crown over time as a result of a 100 km/h train crossing over soil cover depths of 2, 3, and 4 m. 100

Figure 3.15 Deformation of the crown over time as a result of a 150 km/h train crossing over soil cover depths of 2, 3, and 4 m. 101

Figure 3.16 Deformation of the crown over time as a result of a 200 km/h train crossing over soil cover depths of 2, 3, and 4 m. 101

Figure 3.17 Deformation of the crown over time as a result of a 250 km/h train crossing over soil cover depths of 2, 3, and 4 m. 102

Figure 3.18 Deformation of the crown over time as a result of a 300 km/h train crossing over soil cover depths of 2, 3, and 4 m. 102

Figure 3.19 The influence of different high-speed trains on thrust forces at soil cover depths of 2, 3, and 4 m... **Error! Bookmark not defined.**

Figure 3.20 The influence of different high-speed trains on Bending Moment at soil cover depths of 2, 3, and 4 m. 106

Figure 3.21 Bending moment corresponding to 300 km/h traveling train speed with a soil cover depth of 2 m. 106

Figure 4.1 Variation of bearing pressure with footing settlement (Davarifard et al., 2015). .114

Figure 4.2 Variation of bearing pressure number with various geocell layers count at different values of settlement (Davarifard et al., 2015). 115

Figure 37 AutoCAD representation of Geocell drafting 122

Figure 4.4 Geocell layout and positioning in accordance with SMBs 124

Figure 4.5 Crown Deformation over time for a traveling train speed of 300km/h 127

Figure 4.6 Honeycomb Geocell top layer Z-direction deformations at 0.3 seconds 130

Figure 4.7 Honeycomb Geocell bottom layer Z-direction deformations at 0.3 seconds........ 131

Figure 4.8 Honeycomb Geocell top layer Z-direction deformations at 1.2 seconds 131

Figure 4.9 Honeycomb Geocell bottom layer Z-direction deformations at 1.2 seconds........ 132

Figure 4.10 Crown Acceleration in Z-direction as a function of time for a traveling train speed of 300km/h 133

Figure 4.11 Crown Acceleration in X-direction as a function of time for a traveling train speed of 300km/h 136

Figure 4.12 Crown Acceleration in Y-direction as a function of time for a traveling train speed of 300km/h 138

ABSTRACT

Soil metal bridges (SMBs) represent a cost-effective and efficient solution for creating pathways over depressions or obstacles. Previous research has underscored the remarkable durability and substantial load-bearing capacity of SMBs under various loading conditions. However, there is a gap in the literature concerning the behavior of these structures under heavy dynamic loads. This thesis employs a three-dimensional finite element methodology to investigate the response of SMBs to dynamic train loads. The primary focus is on understanding the impact of high-speed trains on SMB performance and exploring the potential enhancements through Honeycomb geocell reinforcement. The investigation encompasses analyses of crown deformations, maximum bending moments, and thrust forces. Fifteen 3D models were developed, incorporating five train speeds ranging from 100 to 300 km/h and three distinct soil cover depths of 2, 3, and 4 meters. Simulations were executed using plaxis3D software, with the CRH 380A train model. The study's findings highlight the influence of soil cover depth on the overall performance of SMBs under dynamic train loads, particularly in shallower cover depths. The study underscores the importance of carefully evaluating soil cover depth to guarantee the secure and dependable functionality of soil metal bridges within high-speed rail systems.

LIST OF ABBREVIATIONS AND SYMBOLS USED

AASHTO	American Association of State Highway and Transportation Officials
AISI	American Iron and Steel Institute
ARTC	Australia's Rail Track Corporation
CALTRANS	California Transportation System
CHBDC	Canadian Highway Bridge Design Code
CSA	Canadian Standards Association
CSP	Corrugated Steel Plate
DAFs	Dynamic Amplification Factors
DMRB	British Design Manual
FE	Finite Element
FLS	Fatigue Limit State
HSs	Hardening Soil Model with Small Strains
MDS	Maximum Design Speed
OHBDC	Ontario Highway Bridge Design Code
SCI	Soil-Steel Culvert Interaction
SLS	Serviceability Limit State
SMBs	Soil Metal Bridges
ULS	Ultimate Limit State

Symbols

h_c	Hight of the cover
A_f	A coefficient obtains its values from Figure 2.6, contingent upon the relationships between $H/D\ and\ D/S$.
D_h	Effective span of the metal structure
D_o	Initial diameter of geocell pocket
D_v	Effective rise of the metal structure
E_{50}^{ref}	Secant stiffness in standard drained triaxial test
EI_s	Culvert wall stiffness
E_{oed}^{ref}	Tangent stiffness for primary oedometer
E_s	Secant modulus of soil stiffness
E_{ur}^{ref}	Unloading/reloading stiffness
F_s	Safety factor to guard against the formation of a plastic hinge
H_{min}	Minimum required depth of cover
K_p	Passive earth pressure coefficient
K_u	Young's modulus parameter of unreinforced sand
L_ϕ	Influence line length
M_1	Moment due to backfill to the crown level
M_B	Moment due to backfill above the crown
M_c	Moment due to construction loads
M_{pf}	Factored plastic moment capacity of a corrugated metal section
N_f	Dimension ratio

P_a	Atmospheric pressure
P_{pf}	Factored compressive strength of the corrugated metal section without buckling
R_n	Nominal capacity of the conduit wall or longitudinal seam to withstand axial thrust
T_D	Axial thrust due to unfactored dead load
T_L	Thrust in the conduit wall due to live loads
T_c	Axial thrust due to unfactored construction loads
T_f	Axial thrust due to dead and live loads
p^{ref}	Reference confining pressure
v_{ur}	Elastic unloading-reloading Poisson's ratio
α_D	Load factor for dead loads, typically 1.25 for soil backfill
α_L	Load factor for live loads, typically 1.70 for CHBDC design truck
γ_{bt}	Ballasted tracks acceleration limit
γ_{df}	Ballasted tracks acceleration limit
ε_a	Specific axial strain at soil failure
λ_f	Flexibility number to quantify bending moments caused by backfilling and live loads
φ''	A factor to account for track imperfections
φ'_{dyn}	Dynamic Amplification Factors
ϕ_h	Resistance factor for the plastic hinge in the completed structure
ϕ_{hc}	Resistance factor for the plastic hinge during construction
ϕ_j	Resistance factor for the failure of longitudinal seams
ϕ_t	Resistance factor for the compressive strength of the conduit wall
$\Delta\sigma_3$	Additional confining stress

$\Delta\zeta$	Lower threshold for critical damping.
D	Donduit's rise
E	Modulus of elasticity
EA	Axial stiffness
EI	The flexural rigidity
I	Moment of inertia
S	Effective span of the bridge
A	Cross-sectioned area of the conduit wall/unit length
DLA	The dynamic load allowance
M	Bending moment
N	Thrust/compression force
R	Radius of the culvert
ρ	External soil pressure on the ring
ψ	Dilation angle

ACKNOWLEDGEMENTS

To my beloved Dad, Nasser Metwally, and incredible mother, Mona, I owe the deepest gratitude for being my unwavering pillars of support and endless sources of love, propelling me through every step of my academic journey. Dad, your wisdom and encouraging words not only serve as my guiding light but also as the steady foundation beneath my aspirations. Your strength and warmth fashion a comforting sanctuary that emboldens me to confront challenges with resilience. My dear siblings, Mohamed and Zainab, your presence has been a source of inspiration and joy, adding a special brightness to this journey. Your support and connection have made each step more meaningful and rewarding, turning this academic adventure into a shared family achievement.

A sincere and heartfelt thank you to my exceptional supervisor, Dr. Hany El Naggar. Your consistent support, guidance, and belief in my abilities have truly been the foundation of my success in research. Your mentorship not only guided my academic journey but also played a role in my personal and professional development.

I want to express my deep appreciation to my dear friends who accompanied me on this journey. Your companionship, shared laughter, and unwavering encouragement not only made the challenges more manageable but also added immense joy to the successes. To my family, Dr. Hany El Naggar, and my friends, your collective support has been indispensable, and I am genuinely grateful for the warmth and strength each of you provided throughout this extraordinary journey.

CHAPTER 1 INTRODUCTION

1.1 Research Background

The evolution of bridge design and construction techniques has been pivotal in meeting the demands of modern infrastructure development. As markets evolve, so do the requirements for bridges, necessitating the incorporation of research breakthroughs and computer tools to create more efficient and resilient structures. One notable trend is the increasing complexity and slender designs of bridges to accommodate heavier loads. Composite bridges, which harness the advantages of multiple materials within a single structure, have gained prominence Pipinato and De Miranda, (2016).

Among these composite bridges, Soil Metal Bridges SMBs have emerged as an innovative solution. SMBs are constructed using structural steel plates and engineered soil, creating a symbiotic interaction between these materials. This approach offers a cost-effective and eco-friendly alternative to traditional concrete bridges (Corrugated Steel Pipe Institute & American Iron and Steel Institute, 2007; Safi, 2012; Du, 2015; Du et al., 2018). SMBs provide benefits such as shorter construction times and simplified assembly processes.

The historical roots of SMBs are traced back to as early as 1913 when researchers at Iowa State College, including Marston and Spengler, began exploring these structures. Initially, these structures were designed based on the ring compression theory, primarily driven by the normal force in the wall conduit. However, as the need for larger-span structures with low soil cover grew, there was a reevaluation, particularly in considering flexural capacity (Duncan, 1979; White and Layer, 1960).

Figure 1.1 Baltic Road Arch at Trans Canada Highway, Clyde River, PEI

This reevaluation was instrumental in the development of specifications for large-span culverts, with recommended modifications subsequently incorporated into design methods like AASHTO AASHTO, (2012). The Swedish Design Method SDM, rooted in the principles of soil-culvert interaction, emerged in 2000 and was further refined through field testing (Pettersson and Sundquist, 2014; Pettersson et al., 2015). Design codes, such as the Ontario Highway Bridge Design Code (2019) and the Canadian Highway Bridge Design Code (2014), have evolved to accommodate SMBs, aligning with advances in construction techniques and corrugation development (CSA Canadian Standards Association, 2014).

Recent years have witnessed a surge in interest in SMBs due to their economic use of materials, rapid construction, and elimination of expansion joints (Wadi, 2019). Research has flourished, focusing on various aspects, including load analysis static, dynamic, and seismic, construction phase stress, bearing capacity, groundwater influence, and utilization on sloping terrain (Bayoglu Flener, 2010; Maleska & Bęben, 2021; Łydżba et al., 2017; Wadi et al., 2015). Both real-scale tests and theoretical models have played pivotal roles in advancing understanding (Pettersson et al., 2015).

Numerical analysis has emerged as a powerful tool, offering the potential for substantial cost savings by optimizing design parameters like shell shape and backfill cover (Sobótka, 2020; AbdelSayed and Salib, 2002; Esmaeili et al., 2013; Machelski and Antoniszyn, 2005; Maleska and Bęben, 2019). However, challenges remain in accounting for construction phases, implementing frictional interface models, and establishing constitutive relations for plastic behavior of backfill soil (Kunecki, 2014; Sobótka, 2014; Sobótka and Łydżba, 2019).

Critical to the performance of SMBs is the interaction between the shell and surrounding soil during backfilling. Proper shell pre-tensioning through uplift during backfilling and subsequent stress reduction during operational loads are key considerations (Kunecki, 2014; Maleska and Bęben, 2019; Mańko and Bęben, 2005; Pittino and Golser, 2006; Taleb and Moore, 1999).

Moreover, the behavior of SMBs under moving loads, characterized by a hysteresis effect, is an intriguing area of study. This phenomenon involves distinct hysteresis loops for shell displacements during vehicle passage and return, with the shell's deformation returning to its initial state after each loading cycle (Sobótka, 2014; Machelski, 2014). Understanding these dynamics is pivotal for accurate modeling of SMBs behavior.

In addition, recent research has focused on the influence of shell ballasting during backfilling on results during the operational phase, particularly under vehicular moving loads. Ballasting, achieved by applying additional loads to the shell during backfilling, aims to achieve beneficial prestressing effects. Practical implementations often involve placing concrete slabs on the shell to limit excessive uplift. Strain gauge measurements have been employed to validate finite element analysis results, improving alignment between measurements and modeling outcomes (Sobótka et al., 2020).

In recent investigations, researchers have embarked on an extensive exploration of the intricate dynamics associated with dynamic loading on bridges and structures, with a specific focus on SMBs (Yeau et al., 2009). A remarkable revelation defied conventional wisdom, as it became evident that deflections induced by moving trucks were counterintuitively lower than those resulting from the static loading by the same vehicles. Moreover, Yeau and colleagues unveiled a non-linear relationship between the depth of soil cover and SMBs deflection, where shallower soil covers exhibited more pronounced deflections. This discovery instigates a reevaluation of long-standing assumptions and highlights the pivotal role of soil cover depth in mitigating deflections induced by dynamic loading.

Expanding upon this line of inquiry, the effects of dynamic loading by scrutinizing Dynamic Amplification Factors DAFs resulting from truck passages over SMBs was also investigated. The study's findings unveiled that both displacements and strains experienced heightened magnitudes during dynamic loading when compared to static loading conditions (Beben, 2012). Of paramount significance, Beben's work identified the span length of SMBs as a critical factor influencing DAFs, with longer spans yielding higher DAF values. This underscores the vital importance of considering bridge span length when anticipating dynamic loading scenarios. Furthermore, Beben extended the inquiry to encompass the dynamic impact of service trainloads on SMBs, emphasizing the necessity of understanding dominant frequencies below 6 Hz to mitigate resonance phenomena and inform structural adjustments.

Shifting the research focus to integral bridges and culverts, a comprehensive investigation conducted by Flener (2004) ventured into the determination of Young's modulus while simultaneously comparing various calculation methods. Notably, this study has highlighted a direct correlation between soil cover depth and the bending moments induced by soil load. However, this relationship has been shown to exhibit non-linearity, thereby prompting a strong recommendation for the incorporation of nonlinear soil models to provide a more precise representation of dynamic loading effects. Furthermore, dynamic tests carried out on a steel culvert railway bridge in the same year have illuminated the intricacies associated with predicting dynamic loading outcomes, revealing significant deviations between measured moments and theoretical calculations, even when considering safety factors.

In a case study conducted by Mellat (2012), the dynamic behavior of an SMBs under diverse trainloads underwent scrutiny through advanced finite element models. Mellat introduced the concept of an elastic soil modulus as a dynamic parameter, acknowledging the transient nature of dynamic loading effects. This innovative approach permitted the selection of higher modulus values, aligning with the dynamic response of the soil. The study revealed variations in the effects of soil modulus, particularly concerning soil density and its influence on ballast acceleration. Mellat advocated prioritizing direct integration methods for their reliability, while also acknowledging the utility of modal analysis in predicting resonance behavior.

1.2 Problem Description

Corrugated steel plate CSP has established itself as a reliable construction material for culverts and storm sewers in North America and various other countries, with a history dating back to 1896. CSP has consistently demonstrated its ability to provide long service life in installations accommodating diverse soil and water conditions. Extensive studies have been conducted to assess CSP behavior concerning both the soil side and the effluent side, affirming its remarkable durability, particularly in resisting soil-related effects. This study addresses this gap by investigating the behavior of soil steel arch bridges subjected to significant vertical loads, specifically examining the influence of train speed on the deformation of the bridge crown, considering varying soil cover depths. The primary objective of this study is to identify effective methods to enhance the crown deformation performance of shallow-depth soil steel arch bridges. To accomplish this, finite element analysis, utilizing a 3D model representation of the metal bridge through Plaxis3D, was employed as the analytical method.

Key findings from the study underscore the critical role of cover depth above the culvert crown in influencing the maximum deformation under different train speeds. Additionally, the research reveals that dynamic loading effects are more pronounced when dealing with shallow-depth structures. In summary, the choice of an adequate cover depth is pivotal in the construction of metal soil bridges to ensure optimal structural performance and minimize the risk of failure.

1.3 Research Objectives

The primary objective of this research is to comprehensively investigate the dynamic behavior of SMBs constructed with corrugated steel plates under heavy dynamic loads, particularly those induced by train traffic. The specific research goals are as follows:

- Employ finite element analysis, utilizing a 3D model representation of the metal bridge through Plaxis3D, to simulate and predict the deformation response under different loading scenarios.
- Analyze and quantify the deformation patterns of soil steel arch bridges when subjected to dynamic loading caused by trains, with a specific emphasis on crown deformation.
- Examine the relationship between train speed and crown deformation, identifying the critical thresholds where deformation becomes significant.
- Investigate the influence of varying soil cover depths above the culvert crown on deformation behavior and assess the optimal cover depth for minimizing deformation.
- Explore the feasibility and effectiveness of using Geocell as a soil reinforcement technique for enhancing the structural performance and load-bearing capacity of SMBs.

CHAPTER 2 LITERATURE REVIEW

2.1 Soil Metal Bridges

Over the years, the field of civil engineering and bridge construction has seen the development of different types of bridges. Among these is the Soil Metal Bridge SMBs as shown in Figure 2.1, a structure that aims to offer economical and efficient solutions for bridging gaps and enabling transportation. Also referred to as Soil-Steel Structures, Soil Metal Bridges have become increasingly popular due to their versatility and cost-effectiveness, providing an alternative to conventional bridge designs. This chapter delves into the realm of Soil-Steel Bridges, examining their construction, advantages, and important design factors. Featuring a shell of curved corrugated steel plates, SMBs is a distinct structure. It's enveloped by a specially engineered soil, typically composed of well-graded granular soil, which forms a well-compacted backfill around the steel shell. The combination of soil and metal gives rise to a sturdy and unyielding bridge that can span numerous distances and resist environmental elements. Conduits, whether for transportation or water flow, comprise the adaptable structure of SMBs. These structures not only function as bridges but also as culverts for water conveyance. Tailoring the number of conduits to the intended use, SMBs can facilitate a single passageway or multiple avenues. One of the key advantages of Soil-Steel Bridges is their cost-efficiency, especially for spans of up to 25 m. In comparison to conventional bridge designs like concrete slab bridges and slab-on-girder bridges, Soil-Steel Bridges offer significant cost savings. In North America, for instance, Soil-Steel Bridges are typically around 30% cheaper than their conventional counterparts. This affordability has made them an attractive choice for various infrastructure projects.

Figure 2.1 Train passing over a SMB (A. Andersson et al, 2012)

2.1.1 Terminology and Standardization

Despite their long history of use, Soil-Steel Bridges have not seen standardized terminology across the industry. The Ontario Highway Bridge Design Code OHBDC introduced the term "soil-steel structures" in 1979, which is now often referred to as "soil-steel bridges." However, the term "structure" was preferred over "bridge" to acknowledge that these versatile constructions are not limited to vehicular bridges but also serve in other applications, such as avalanche protection. To better understand Soil-Steel Bridges as shown in Figure 2.2, let's explore some widely used terms associated with these structures:

Arching: The transfer of vertical pressure between adjoining soil masses above and adjacent to the conduit.

Bedding: The prepared portion of engineered soil where the conduit invert is placed.

Compaction: The process of soil densification through mechanical or manual means.

Conduit: The bridge opening in a Soil Metal Bridge.

Crown: The highest point of the conduit.

Deep/shallow Corrugations: Structural plate corrugations with specific dimensions.

Depth of Cover: The vertical distance between the roadway and the crown.

Engineered Soil: Selected soil with known properties placed around the conduit.

Foundation: The ground on which the Soil Metal Bridge is constructed.

Haunch: The portion of the conduit wall between the springline and the top of the bedding.

Invert: The portion of the conduit wall contained between the haunches.

Rise: The maximum vertical clearance inside a conduit.

Shoulder: The portion of the conduit wall between the crown and springline.

Span: The maximum horizontal clearance inside a conduit.

Springline: The horizontal extremities of transverse sections of the conduit.

Transverse Direction: The direction perpendicular to the conduit axis.

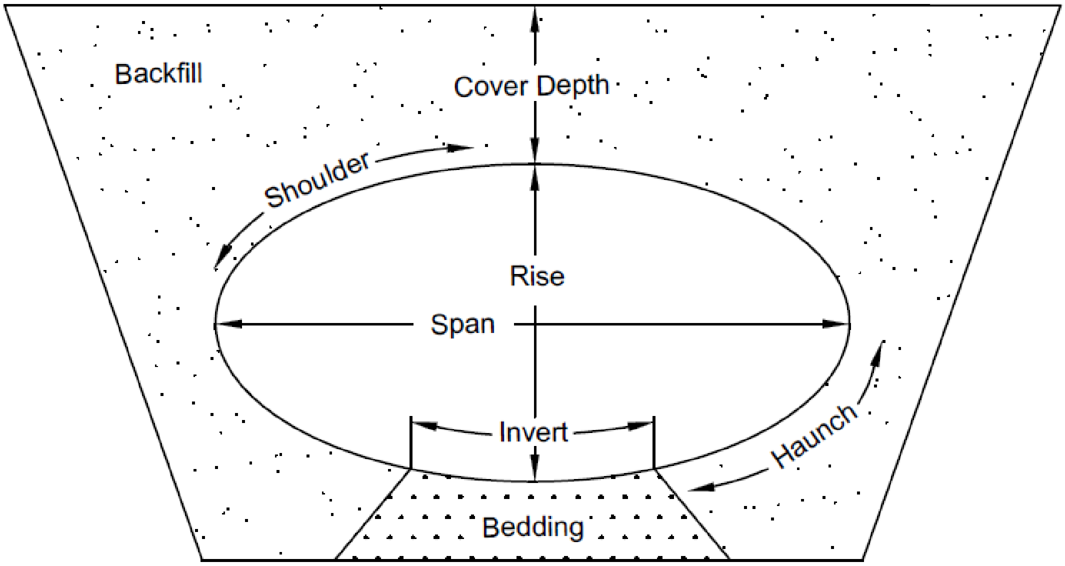

Figure 2.2 Visualization of the terminology related to soil-steel bridges.

2.1.2 The Significance of Geotechnical Investigations

Before the first steel plate is laid or the initial scoop of backfill is deposited, meticulous geotechnical investigation is imperative. This in-depth examination of the site's subsurface conditions is akin to laying the foundation for the project's success. Geotechnical investigations involve a series of tests and assessments aimed at determining soil properties, bearing capacity, and any potential challenges the site may present. These investigations are especially vital when prior knowledge of the area's subsurface conditions is lacking. They serve as the bedrock upon which decisions about site suitability and risk mitigation are made.

The engineered backfill is the unsung hero of Soil-Metal Bridges. Composed primarily of well-graded granular soils, this backfill provides the necessary support and stability for the bridge structure. The selection of the right soil for this purpose is a decision that reverberates throughout the bridge's lifespan. Engineered backfill suitability is classified according to ASTM D2487

(2006), as presented in Table 2.1. This classification system categorizes soils based on their properties and compaction characteristics. Engineers rely on these guidelines to ensure that the selected soils meet the stringent criteria for stability and compaction, laying the foundation for a robust structure.

The secant modulus of soil stiffness, represented as E_s, is a key parameter that varies depending on soil type and compaction level. This value provides insights into how a soil's stiffness evolves under different compaction conditions, a vital aspect of Soil-Steel Bridge design. CHBDC (2006) outlines specific E_s values for different soil groups and various Standard Proctor densities defined by ASTM D698 2007, as seen in Table 2.2. These values serve as a compass for geotechnical engineers, guiding their decisions during design and construction.

Table 2.1 Soil classification based on ASTM D2487 2006.

Soil Group	Grain Size	Soil type
I	Coarse	Well graded gravel Well sandy gravel Poorly graded gravel Poorly sandy gravel Well graded sand Well gravelly sand Poorly graded sand Poorly gravelly sand
II	Medium	Clayey gravel clayey-sandy gravel Clayey sand clayey gravelly sand Silty sand silty gravelly sand

Table 2.2 Secant modulus of soil values for various soil groups and different Standard Proctor densities in accordance with ASTM D698 (2007).

Soil Group	Standard Proctor Density %	Secant modulus of soil E_s MPa
I	85	6
	90	12
	95	24
	100	30
II	85	3
	90	6
	95	12
	100	15

The importance of E_s values cannot be overstated, yet it's imperative to acknowledge their dynamic nature. These values undergo changes depending on factors such as soil group and compaction density. To harness the power of these values, they are often graphically represented against Standard Proctor densities, as seen in Figure 2.3. Geotechnical analysis using E_s values aids in understanding how the soil will behave under different loading conditions. This knowledge is pivotal for predicting settlement, evaluating bearing capacity, and assessing lateral earth pressure. Armed with this information, engineers can make informed decisions, ensuring the structural integrity of the soil metal bridges.

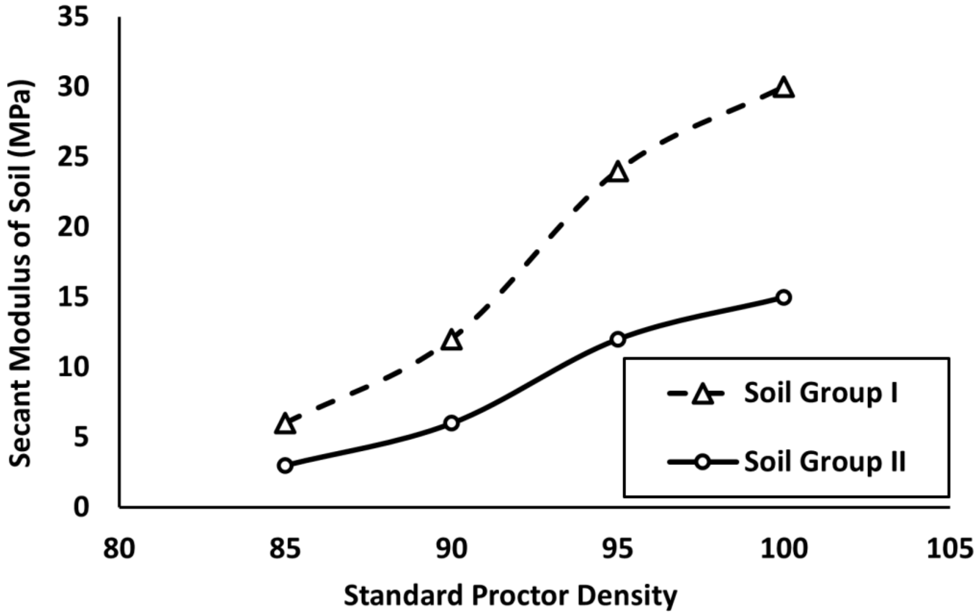

Figure 2.3 Variation of E_s with Standard Proctor Density for Different Soil Groups

2.1.3 The Structural Resilience of Corrugated Metal Bridges

During the construction phase of corrugated metal bridges, the initial assembly involves securing corrugated metal plates using bolts. This early stage reveals the structure's inherent flexibility and susceptibility to deformations. The primary challenge faced by these metal structures is the phenomenon of global buckling. However, their flexibility allows them to interact with the surrounding backfill soil, a characteristic that proves crucial in ensuring their stability.

As engineered fill is systematically introduced on both sides of the structure, the sidewalls initially experience inward deformations due to the forces exerted by the backfill. However, as the fill progresses towards the haunch zones and eventually reaches the crown of the culvert, the weight of the soil exerts downward pressure. This triggers an attempt at outward deformation, countering the bending moments generated during initial construction. The compacted backfill effectively restrains this outward movement, transforming the structure from a pliable form into a rigid one.

This dynamic interaction enhances global stability and bolsters the required loading capacity, often allowing the corrugated metal plate to approach its material strength limits without encountering issues of stability failure or excessive deflection.

To reinforce the structural capacity of SMBs, the incorporation of stiffening ribs is a common practice. This strategy aims to augment both bending capacity and structural rigidity (Abdel Sayed et al., 1993). While these structures typically feature corrugated plates with shallow profiles, the option of utilizing deep corrugated plates, especially in steel structures, presents itself. These deep corrugations, approximately three times deeper than those in shallow profiles, offer increased strength (Corrugated Steel Pipe Institute, 2002). The introduction of deep corrugations by the Canadian industry has expanded the potential span of Soil-Steel Bridges to as much as 24 m, offering even greater flexibility in their application.

Traditionally, L-shaped stiffeners were applied to the crest of each corrugation to maximize their effectiveness. However, their asymmetrical cross-sectional configuration, with a substantial metal portion at the top of the vertical leg, rendered them susceptible to lateral buckling under compressive forces, limiting their efficiency. Laboratory experiments conducted by Newhook and Ford 2010 faithfully replicated this phenomenon of buckling, highlighting this challenge.

Recent advances in stiffener design have led to the approval of innovative designs for aluminum boxes by ASTM B864M. These novel stiffeners adopt a closed-shaped, symmetrical configuration when securely attached to the corrugated plate. This refined design not only provides superior resistance to buckling but also allows for the full utilization of the stiffener's plastic moment capacity during the design phase. The research conducted by Newhook and Ford (2010) showcases that these closed-shaped stiffeners have the potential to provide strengths up to 25% higher than their equivalent L-shaped counterparts. This represents a substantial advancement in structural performance. This pioneering stiffener design delivers a 66% increase in flexural strength compared to the currently endorsed L-shaped stiffeners featured in ASTM B864M.

2.1.3.1 Static Methods of Analyses

2.1.3.2 Minimum cover depth

A core challenge in soil-metal bridge design stems from the soil structure interaction between soil pressures and the conduit wall's response. A paramount concern in this design process is mitigating soil failure risks, particularly when inadequate soil coverage exists above the steel conduit. In response to this challenge, regulatory frameworks have been established to ensure the structural integrity of soil-metal bridges. Prominent among these are the Canadian Highway Bridge Design Code CHBDC and the American Association of State Highway and Transportation Officials' AASHTO. These guidelines mandate a requisite minimum depth of soil cover over the conduit crown to avert soil failure caused by shear and tension.

The evolution of these design standards reflects the maturation of engineering practices. Originally rooted in experiential insights and practical knowledge, these standards underwent refinement with the integration of advanced methodologies. Finite element analysis emerged as a transformative computational tool, enabling engineers to precisely tailor the minimum cover depth criteria. As a testament to this rigorous analysis, CAN/CSA-S6-14 – Canadian Highway Bridge Design Code (2014) specifies that the minimum cover depth 'h' should be calculated as the greater of S/6 or 0.6 m. In this context, 'S' denotes the effective span of the bridge, while 'D' signifies the conduit's rise as illustrated in Figure 2.4.

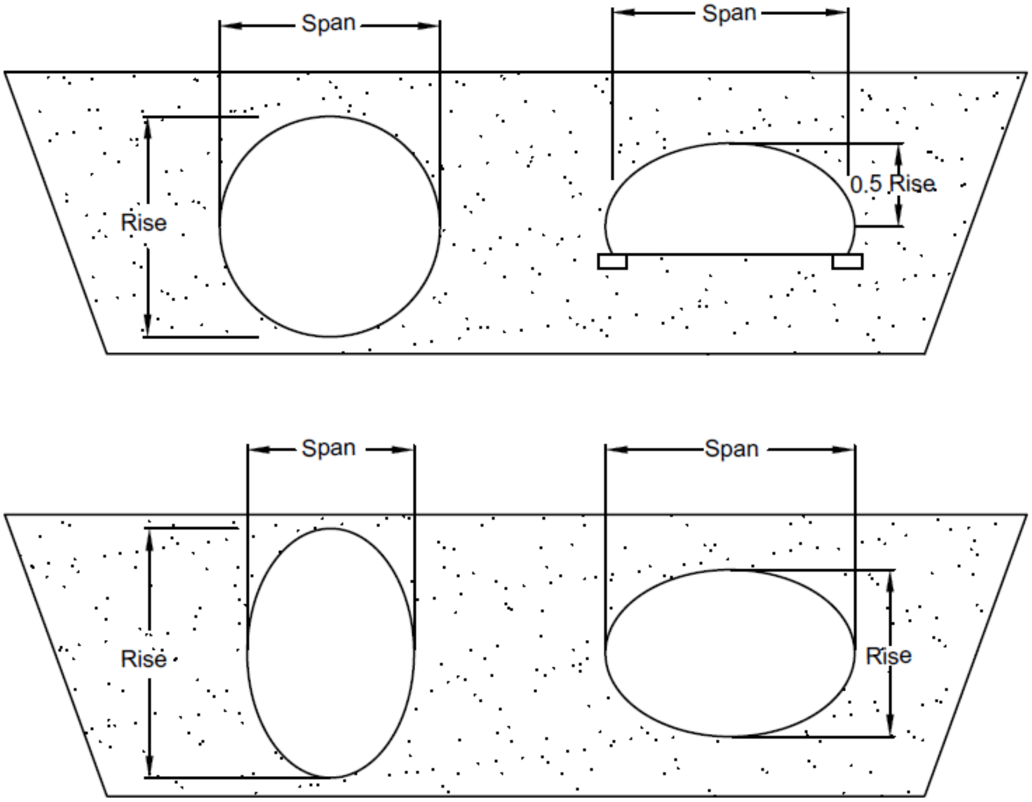

Figure 2.4 Definition of span S and Rise D for various conduit shapes.

Designing soil-metal bridges is a nuanced endeavor due to the intricate interplay between soil pressures and the conduit wall's response. The bridge's geometry, span, and load-bearing capacity constitute pivotal factors in ensuring structural stability. The predominant challenge lies in mitigating the risks of soil failure, especially when inadequate soil coverage exists over the steel conduit. Recognizing the critical significance of this aspect, a plethora of regulatory frameworks have been established. Noteworthy among these are the California Transportation System CALTRANS, British Design Manual DMRB, American Iron and Steel Institute CSPI and AISI, and the American Association of State Highway and Transportation Officials AASHTO. These regulations prescribe a minimum depth of soil cover over the conduit crown to safeguard against soil failure, an outcome often precipitated by shear and tension forces.

The assessment of minimum allowable soil cover depth has transitioned significantly. Initially rooted in empirical practices, these requirements were defined as fractions of the bridge span S in codes and standards. Subsequently, ASTM A796 (2017) introduced a more complex model that considered parameters such as axle load AL, eccentric distance d, elastic modulus E, and the moment of inertia I of the corrugated steel plates. Australia's Rail Track Corporation ARTC also contributed by recommending specific values for the minimum depth of cover for different railway track classes.

The watershed moment in the evolution of minimum soil cover depth assessment came with the incorporation of finite element FE analysis. OHBDC (1991) was among the pioneers in modifying empirical formulas based on FE analysis results, which considered both the geometric shape of the metal structure and the axle load of a truck. This marked a significant departure from empirical methods and ushered in a more precise approach.

Present-day standards, like the Canadian Highway Bridge Design Code (2006), specify the minimum required depth of cover H_{min} as the greater of 0.6 m, $D_h/6$, or $\left(\frac{D_h}{D_v}\right)^{0.5}$. Where, D_h and D_v represent the effective span and rise of the metal structure, respectively. This empirical-based formula is widely adopted for calculating the depth of cover for both highway and railway bridges.

Esmaeili (2013) highlights that the existing minimum depth of cover requirements for soil-steel bridges are primarily based on vehicle loads and geometrical factors. He addresses the need for re-evaluation, particularly for spans over 8 m, incorporating stiffened panels under railway loads. By conducting 2D and 3D finite element analyses on various bridge types, Esmaeili introduces new formulas for determining the minimum soil cover depth. Esmaeili (2013) key findings indicated that as spans increased, the minimum cover depth followed an exponential growth pattern.

Additionally, enhancing the rigidity of wall panels significantly reduced the required cover depth, especially for longer spans. The structural geometry of box bridges and low-profile arches influenced different trends in minimum cover depth. Elsameili (2013) basic equation to calculate the minimum depth is given by:

$$H_{min} = \alpha {N_f}^{\beta} e^{\mu Dh} \tag{1}$$

$$N_f = \frac{E_s D_h^3}{EI} \tag{2}$$

In the equation, N_f represents the dimension ratio, E_s stands for the secant modulus of the backfill, which is influenced by backfill quality, compaction, and depth of cover, E represents the modulus of elasticity of the corrugated plates, and I symbolize the moment of inertia of the conduit wall per unit length of the bridge. The variables α, β, and μ in Equation 1 are unknown constants. To establish accurate values for these constants, separate calculations were performed for boxes and low-profile arches. The least-squares method was employed to identify the optimal fit for each function. The final set of parameters can be found in Table 2.3.

Table 2.3 The variables α, β, and μ based on Elsameili (2013) calculation.

Parameter	Box culvert	LPA culvert
α	0.0139	0.0139
β	0.25	0.25
u	0.34	0.34

Flener et al. (2009) examined the actual dynamic response of a long-span corrugated steel culvert railway bridge, a type of soil-steel composite structure with an 11 m span. Through comprehensive tests that measured strains, displacements, vertical ballast accelerations, and braking forces during locomotive passages at varying speeds, the researchers uncovered significant insights. The findings revealed that speed plays a crucial role in influencing displacements, thrusts, and moments. Dynamic displacements and thrusts measured during the tests were up to 20% larger than the corresponding static responses, exceeding values specified in bridge design codes.

2.1.3.3 Ring Compression Theory

The origins of the ring compression theory can be traced back to research and observations dating as far back as the 1940s. During this time, researchers came to understand that the structural integrity of flexible culverts is primarily reliant on the application of normal compression forces within the culvert walls. This ingenious design effectively harnesses the surrounding soil as a form of natural support. Consequently, this realization underscored the critical importance of soil quality in ensuring the proper performance of culvert installations. As a result, the careful selection of high-quality, frictional soil for various aspects such as the culvert bed, backfilling, and cover soils became imperative. This perspective sheds light on the historical evolution of the theory and its tangible implications for practical engineering.

White and Layer (1960) provided a compelling physical example to demonstrate the ring compression theory. The illustration fits brilliantly with a standard 1-lb coffee can that has had the bottom and top removed. Although this model can be broken with the hand, it is strong enough to be installed in the ground as a small conduit. It can support a man's weight if it is set up in earth that has been compacted around the edges and covered with roughly 1 inch of the same material. The important aspect is not how much force exactly must be applied to cause the installed structure to collapse in compression and surpass the moment strength of the coffee can model. The importance of the model lies in the strength disparity and the way that this narrow ring supports the pressure. Despite its diminutive size and lack of material, the model shows how a small thin ring can hold a considerable amount of weight and sustain sizable pressures. This demonstrates the usefulness and potency of the ring compression theory and provides a concrete illustration of how it might be put to use in practical settings.

White and Layer brought the ring compression theory to life by utilizing a 2x4 wood clamp to mimic the effect of earth fill as shown in Figure 2.5. This demonstration is not focused on numbers and figures but rather on the qualitative aspect, where the wooden clamp serves as a near-perfect representation of an earth fill and is not suitable for mathematical analysis. However, it provides a clear illustration of the relationship between fill and structure.

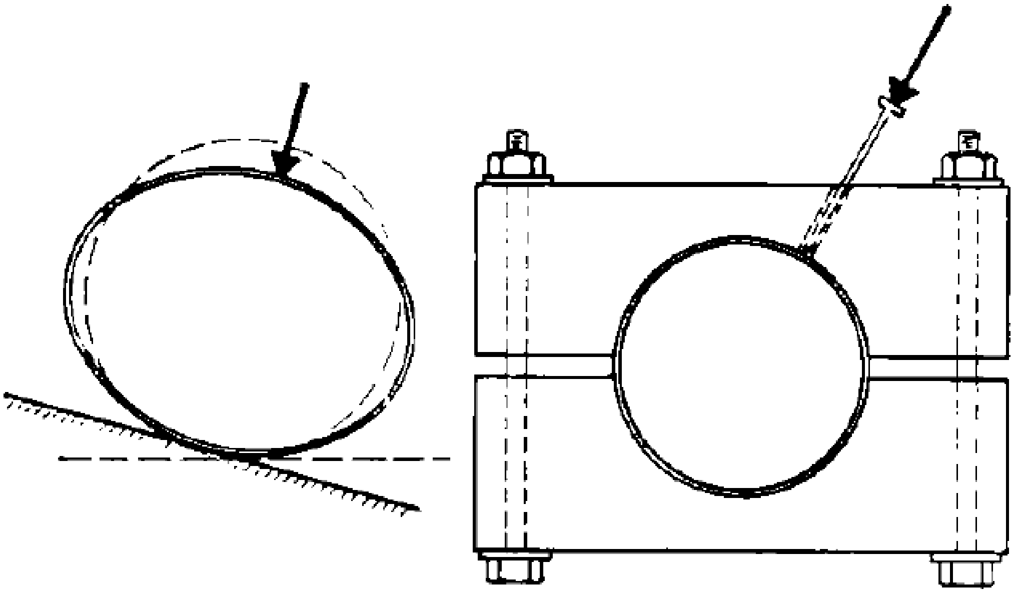

Figure 2.5 Thin steel ring supports relatively large, concentrated load when confined right, but easily flattened when unconfined left. (White and Tayler, 1960)

The moment strength of the model conduit can be observed when placed on a table and an attempt is made to drive a nail through it. But when the same model is nestled within the wooden clamp, simulating a flawless earth backfill, it holds its round shape even as the load on the nail increases. Even when the nail is driven through the metal with a hammer, the shape of the can remains unchanged, indicating that no moment strength was used to resist the concentrated load of the driven nail point. This serves to highlight that the structure can only maintain its round shape under heavy concentrated force if heavy radial forces are applied all around its periphery. In the case of the can within the wooden clamp, these forces are generated by the interaction between the can and the wooden clamp, and in the ground, similar reactions are achieved by the combination of active and passive earth load vectors. This example is a creative way to explain the ring compression theory, demonstrating how the shape of the structure is retained under stress when there are balanced forces on the periphery.

The ring compression theory, as explained in the provided Figure 2.5, is a concept used in the design and analysis of flexible culverts. It involves understanding how these structures distribute and carry loads, mainly through normal compression forces within the culvert wall.

The theory is encapsulated in a mathematical formula that relates the intensity of compression within the culvert ring to the normal pressure and the radius of the structure. This mathematical relationship is the opposite of the formula used to calculate hoop tension in a pipe under uniform internal pressure. Specifically, for round structures, the compression Forces N is determined by multiplying the radius of the culvert R by the external soil pressure ρ on the ring (White and Tayler, 1960). This provides a quantitative understanding of how the culvert structure behaves under load. White and Tayler equation can be expressed as:

$$\rho = \frac{N}{R} \tag{3}$$

The theory emphasizes that flexible metal conduits interact with the surrounding soil to achieve their load-carrying capacity. When a load is applied to the top of the culvert, the top sinks, and the sides move outward, mobilizing soil pressure. A well-confined flexible ring is capable of carrying large concentrated loads. This perspective underscores the importance of soil-structure interaction in culvert design, particularly the role of ring compression in load bearing. In the ring compression theory, it is assumed that the loads imposed on the soil-steel structure are carried by normal forces only. This assumption simplifies the analysis but remains a key aspect of the theory. Equilibrium of thrust forces in the culvert wall is achieved because of the low bending stiffness of the culvert wall. However, a minimal amount of bending stiffness is required to bridge irregularities in soil properties. This perspective highlights the theoretical assumptions and the balance between normal forces and bending stiffness in the analysis.

To calculate the thrust N in the culvert wall, the theory suggests using the weight of the soil prism on top of the culvert. This weight is defined by the height of cover h_c and the culvert span S. This approach simplifies the determination of thrust forces and provides a practical method for engineers designing culvert installations The thrust equation (White and Tayler, 1960) is given as:

$$N = \frac{\rho \, h_c \, S}{2} \tag{4}$$

2.1.3.4 Soil culvert interaction method

The Soil-Steel Culvert Interaction SCI method is an advanced and comprehensive approach used in civil engineering for the design and analysis of soil-steel culverts. The SCI method focuses on understanding and optimizing the intricate interaction between these culverts and the surrounding soil, aiming to improve their reliability and safety Duncan, 1978.

At the core of the SCI method are finite element calculations, which involve the use of advanced numerical simulations. These simulations are instrumental in modeling the behavior of soil metal culverts under a wide range of conditions. By breaking down the complex structure into smaller, manageable elements, finite element analysis allows engineers to gain insights into how these elements interact and respond to various forces and loads. To capture the realistic behavior of soils, the SCI method incorporates a non-linear, stress-dependent soil model. This means that the model accounts for the fact that soil properties change in response to different levels of stress. This consideration provides a more accurate representation of how the soil behaves under varying loading conditions, which is crucial for designing culverts that can withstand real-world challenges. Furthermore, the SCI method takes into account the construction sequence of the culvert. It involves step-by-step modeling of the gradual addition of soil layers during installation. This dynamic approach ensures that the analysis considers the evolving interaction between the culvert and the backfill as the construction process progresses. Live loads, such as vehicles or trains passing over the culvert, are a critical aspect of culvert design. The SCI method addresses this by employing back-calculation techniques. It determines an equivalent line load that mimics the vertical pressure at the crown level due to live loads, employing the Boussinesq elastic theory to achieve this representation accurately.

In comparison to traditional ring compression theory, the SCI method often yields different results, frequently predicting larger normal forces acting on the culvert. This divergence arises from factors such as considering a more extensive volume of soil in calculations and recognizing the impact of negative arching, where the soil supports the culvert in unexpected ways. The method introduces the concept of a flexibility number λ_f to quantify bending moments caused by backfilling and live loads. This parameter relates the stiffness of the soil E_s to that of the culvert wall EI_s, aiding in the analysis and design of bending effects. flexibility number after (Duncan, 1978) is given by:

$$\lambda_f = \frac{E_s D}{EI_s} \tag{5}$$

While recognizing the importance of soil stiffness, the SCI method explores its integration into culvert design. However, selecting the appropriate soil modulus can be challenging due to the non-linear behavior of soils. In-depth stress state assessments around the culvert in finite element calculations provide valuable information, such as the relationship between the minor and major principal stresses and soil modulus values at specific points, informing decisions about soil stiffness based on overburden depth.

Duncan study conducted a thorough investigation into the stress distribution around soil-steel culverts through finite element calculations. The findings revealed that the minor principal stress was approximately 30% of the major principal stress Duncan, 1979. Additionally, it was observed that the soil modulus near the so-called conduit quarter points closely matched the average modulus within the surrounding soil fill. Based on these insightful observations, the study proposed specific values for the soil modulus, depending on the overburden depth, particularly around the quarter point level of the culvert.

In the context of culvert design, Duncan emphasized the importance of considering bending moments, especially in situations with low cover heights. These low cover height culverts were defined as those with a cover height less than one-quarter of the span. For cover heights exceeding one-quarter of the span, it’s recommended focusing solely on calculating normal forces. However, it's noteworthy that Duncan also highlighted the need for further research to precisely delineate the conditions under which buckling failure might occur.

In the framework of designing culverts with limited cover depth, Duncan proposed the application of a safety factor F_s to guard against the formation of a plastic hinge. This safety factor was expressed through an N-M interaction design equation in the following manner:

$$\left(\frac{F_s N_d}{N_u}\right) + \left(\frac{F_s M_d}{M_u}\right) = 1 \tag{6}$$

where M stands for the bending moment, while d and u indicate the design and ultimate capacities, respectively. The suggested safety factor was 1.65. However, it's important to note that in statically indeterminate systems, where two or more plastic hinges are needed for a collapse mechanism, the actual factor of safety would be even higher.

The presentation of the Soil-Steel Culvert Interaction SCI method provides a straightforward and logical approach to consider various types of backfill materials and degrees of compaction when calculating the culvert's capacity. (Duncan, 1983) introduced a design procedure for flexible culverts based on the SCI method. This procedure hinges on the critical assumption that culvert failure due to buckling is not a concern and can be summarized into key steps, including checking the capacity to resist backfilling loads formation of a plastic hinge, ensuring seam capacity to resist axial forces in the culvert wall, and verifying the capacity to withstand imposed live loads, particularly relevant for culverts with lower cover heights.

2.1.4 CHBDC Design Criteria

The design and construction of soil-steel bridges are critical aspects of civil engineering projects, ensuring the safe and reliable transport of people and goods. The Canadian Highway Bridge Design Code CHBDC (2006) provides comprehensive guidelines for the design and construction of soil metal bridges. The CHBDC (2006) mandates the consideration of both ULS and SLS in the design of soil metal bridge conduit walls. These limit states ensure that the bridges can withstand extreme conditions while maintaining functionality. Table 2.4 provides a detailed list of the various limit states, along with corresponding material resistance factors. For the ULS, the conduit wall and longitudinal seams of the soil metal bridges must meet specific requirements, as described by Equation 7. This equation incorporates the axial thrust due to dead and live loads, represented by T_f in Equation 8.

$$\phi_t R_n \geq T_f \tag{7}$$

$$T_f = \alpha_D + \alpha_L (1 + DLA) T_L \tag{8}$$

Where,

ϕ_t : Resistance factor for the compressive strength of the conduit wall.

R_n: Nominal capacity of the conduit wall or longitudinal seam to withstand axial thrust.

T_f : the axial thrust due to dead and live loads.

DLA : The dynamic load allowance, which changes in accordance with the depth of the cover starts at 0.4 for no cover depth and decreases linearly to 0.1 at a cover depth of 2.0 m. For cover depths exceeding 2.0 m, the DLA remains constant at 0.1.

α_D : Load factor for dead loads, typically 1.25 for soil backfill.

α_L : Load factor for live loads, typically 1.70 for CHBDC design truck.

T_L : Thrust in the conduit wall due to live loads.

Table 2.4 Restrictions on conditions and factors related to material resistance.

Corrugation Type	Limit state	Component of resistance	Material resistance factor
Shallow Corrugation	ULS	Compression Strength	$\phi_t = 0.80$
	ULS	Plastic hinge during construction	$\phi_{hc} = 0.90$
	ULS	Strength of longitudinal seams	$\phi_j = 0.70$
Deep Corrugation	ULS	Compression strength	$\phi_t = 0.80$
	ULS	Plastic hinge	$\phi_h = 0.85$
	ULS	Plastic hinge during construction	$\phi_{hc} = 0.90$
	ULS	Strength of longitudinal seams	$\phi_j = 0.70$

In the case of soil metal bridges featuring either shallow or deep corrugations, it is imperative that, throughout all phases of construction, the combined impacts of bending moments and axial thrust generated by the unmodified dead load and prescribed construction machinery meet the following criteria as mentioned in Equation 9.

$$\left(\frac{P}{P_{pf}}\right)^2 + \left|\frac{M}{M_{pf}}\right| \leq 1.0 \qquad (9)$$

Where,

P : $T_D + T_c$, in which T_D, axial thrust due to unfactored dead load; T_c, the axial thrust due to unfactored construction loads.

P_{pf}: factored compressive strength of the corrugated metal section without buckling.

M: $M_1 + M_B + M_c$ in which M_1, is the moment due to backfill to the crown level; M_B, is the moment due to backfill above the crown; M_c, is the moment due to construction loads.

M_{pf} : factored plastic moment capacity of a corrugated metal section.

The Moment due to backfill to the crown M_1, above the crown M_B, and due to construction loads M_c can be calculated as follows:

$$M_1 = K_{M1}\, R_B\, \gamma\, D_h^3 \tag{10}$$

$$M_B = -K_{M2}\, R_B\, \gamma\, D_h^2\, H_c \tag{11}$$

$$M_c = K_{M3}\, R_L\, \gamma\, D_h L_c \tag{12}$$

In which:

$$\begin{aligned} K_{M1} &= 0.0046 - 0.001\, log_{10}(N_F),\ \ N_F \leq 5000 \\ &= 0.0009,\ \ N_F > 5000 \end{aligned} \tag{13}$$

$$\begin{aligned} K_{M1} &= 0.018 - 0.004\, log_{10}(N_F),\ \ N_F \leq 5000 \\ &= 0.0032,\ \ N_F > 5000 \end{aligned} \tag{14}$$

$$\begin{aligned} K_{M1} &= 0.012 - 0.018\, log_{10}(N_F),\ \ N_F \leq 100{,}000 \\ &= 0.030,\ \ N_F > 100{,}000 \end{aligned} \tag{15}$$

$$R_B = 0.67 + 0.87\left(\frac{D_v}{2D_v} - 0.2\right), 0.2 \leq \left(\frac{D_v}{2D_v}\right) \leq 0.35 \tag{16}$$

$$R_B = 0.80 + 1.33\left(\frac{D_v}{2D_v} - 0.35\right), 0.35 \leq \left(\frac{D_v}{2D_v}\right) \leq 0.50 \tag{17}$$

$$R_B = \left(\frac{D_v}{D_v}\right), \left(\frac{D_v}{2D_v}\right) > 0.50 \tag{18}$$

$$R_L = \frac{0.265-0.053log_{10}N_F}{\left(\frac{H_C}{D_h}\right)^{0.75}} \leq 1.0 \tag{19}$$

$$L_C = \frac{A_C}{K_4} \tag{20}$$

$$N_F = \frac{E_S 1000 {D_h}^3}{EI} \tag{21}$$

Dead thrust loads on conduit can be obtained by Equation 22, as outlined in the (CHBDC, 2006).

$$T_D = 0.51.0 - 0.1C_sA_fW \tag{22}$$

$$C_s = \frac{E_S D_v}{EA} \tag{23}$$

In which,

A_f: A coefficient obtains its values from Figure 2.6, contingent upon the relationships between $H/D \text{ and } D/S$. In this context, H signifies the depth of soil covering above the crown, while D and S are specified in Figure 2.4.

W: the nominal dead weight of the column above the conduit.

C_s: Axial stiffness parameter defined as in Equation 23.

E_S: secant modulus of soil.

E: Modulus of elasticity of conduit wall material, which can be assumed to be $2.0\ x10^6\ MPa$.

D_v: dimension relating to the cross-section of the conduit wall.

A: cross-sectioned area of the conduit wall/unit length

Table 2.5 K_4 values for live load calculations.

Depth of cover m	Two wheels per axle	Four wheel per axle	Eight wheels per axle
0.3	1.3	1.5	2.6
0.6	1.6	2.0	2.8
0.9	2.1	2.7	3.2
1.5	3.7	3.8	4.1
2.1	4.4	4.4	4.5
3.0	4.9	4.9	4.9
4.6	6.7	6.7	6.7
6.1	8.5	8.5	8.5
9.1	12.2	12.2	12.2

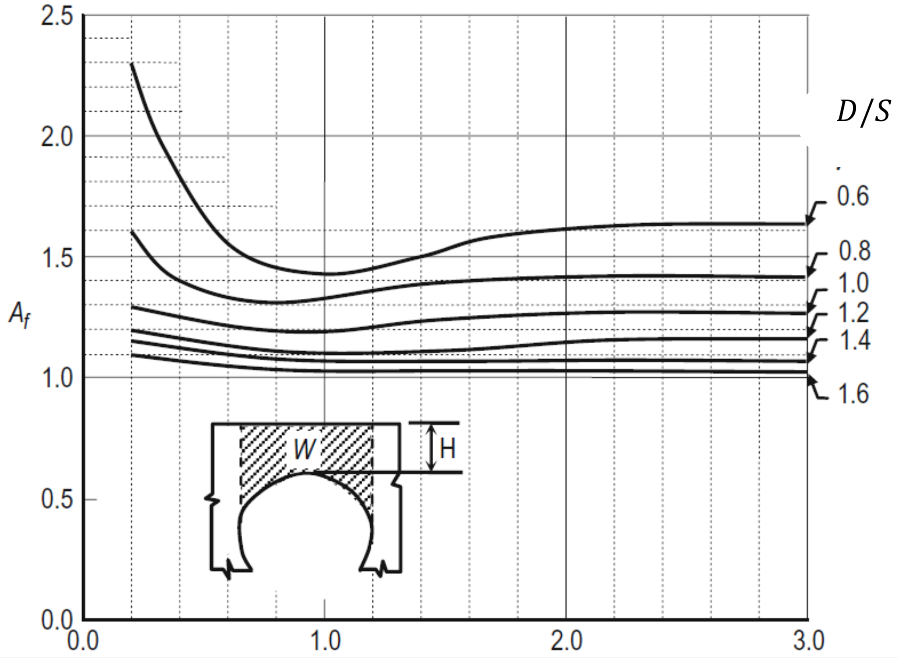

Figure 2.6 Relationships between $A_f, H/D, and\ D/S$

2.1.5 Dynamic Methods of Analyses

The Eurocode framework provides a comprehensive approach to addressing dynamic effects. It starts with determining whether a dynamic analysis is necessary, guided by a decision-making flowchart. If required, a thorough dynamic analysis is prescribed, with Dynamic Amplification Factors DAFs introduced to incorporate dynamic effects. Criteria for assessing dynamic effects' frequency are provided, though more complex structures may necessitate customized analysis. In serviceability limit state design, acceleration limits are crucial for upholding structural integrity, with distinct limits for ballasted and un-ballasted tracks to prevent issues like ballast instability.

2.1.6 Eurocode Approach

The Eurocode design approach, as outlined in SS-EN 1991-2:6.4, provides a comprehensive methodology for addressing dynamic effects in structural design. It initiates with a fundamental consideration, the determination of whether a dynamic analysis is required. SS-EN 1991-2:6.4.4 offers a decision-making flowchart to assist engineers in making this determination. This flowchart guides the assessment of whether a full dynamic analysis, involving the evaluation of bending and twisting modes is necessary. If a dynamic analysis is deemed necessary, the Eurocode prescribes a thorough dynamic analysis. In choosing between a static and dynamic analysis, the Eurocode acknowledges that a static analysis, while simpler, may not fully account for dynamic forces. To bridge this gap, the concept of Dynamic Amplification Factors DAFs is introduced. DAFs are multiplicative factors applied to static loads to incorporate dynamic effects adequately. This ensures that dynamic influences on the structure are appropriately considered. The Eurocode also provides specific criteria for assessing the frequency of dynamic effects. These criteria are initially derived from simpler structures, such as simply supported bridges and tensioned slabs, where dynamic effects can be relatively straightforward to evaluate. However, the Eurocode recognizes that more complex structures, like soil metal bridges SMBs, may not readily align with these criteria. As such, SMBs may require a more detailed and customized dynamic analysis that considers factors like bending and twisting mode shapes.

To determine Dynamic Amplification Factors DAFs φ'_{dyn} for railway tracks that are well-maintained, the Eurocode provides a formula represented by Equation 24 as outlined in SS-EN 1991-2:6.4.5.2. An essential element of this computation revolves around establishing the determining length for the influence line L_{ϕ}, a critical parameter. While the Eurocode doesn't offer specific directives for soil metal bridges SMBs, it permits designers to estimate L_{ϕ} by scrutinizing the influence line pertaining to the deflection of the specific structural component in question. Frequently, engineers employ finite element modeling to facilitate this analytical process. Additionally, the Eurocode permits a reduction in dynamic factors for specific design scenarios. For example, vault-bridges with cover depths exceeding 1.0 m may benefit from such reductions. This provision is detailed in Equation 25 within SS-EN 1991-2:6.4.5.4 and enables a more favorable assessment of dynamic effects, assuming that the structural criteria are met.

$$\varphi'_{dyn} = \frac{1.44}{\sqrt{L_{\phi}}-0.2} + 0.82\ 1.00 \leq \phi \leq 1.67 \tag{24}$$

$$\varphi_{red} = \varphi'_{dyn} - \frac{h-1}{1.67} \geq 1 \tag{25}$$

It is important to recognize that there are limitations on applying this reduction. Notably, the Eurocode stipulates that the reduction of dynamic factors cannot be implemented when more than one track is situated at the railway embankment. This restriction underscores the commitment to maintaining safety as a top priority in designs that involve multiple tracks.

2.1.6.1 Serviceability limit state

Within the framework of serviceability limit state code design, SS-EN 1990:A2.4.4.2.1 takes a crucial role in establishing specific limitations on accelerations within bridge superstructures. These limitations serve as a linchpin in upholding the structural integrity of the designed bridges. Notably, there are distinct acceleration limits based on whether the tracks are ballasted or unballasted. For ballasted tracks, the set acceleration limit stands at $\gamma_{bt} = 3.5\, m/s^2$, while un-ballasted tracks adhere to a stricter limit of $\gamma_{df} = 5\, m/s^2$. These prescribed limits are meticulously determined to forestall issues like ballast instability in the case of ballasted tracks or the potential lift-off of the bearing in unballasted tracks.

The adherence to these acceleration limits is of paramount importance and is particularly emphasized within a specific frequency range, as determined by the highest value among $30, 1.5f_1, f_3$ Hz. In this context, f_1 and f_3 correspond to the frequencies of the first and third bending modes, respectively. The meticulous selection of this frequency range underscores the significance of precisely managing accelerations within the structure. Notably, the Eurocode does not provide explicit recommendations regarding where the analysis of acceleration in SMBs should be conducted. Therefore, the focus of assessing acceleration limits primarily centers on the crown of SMBs structures and the ballast-level. This approach strategically targets the crown as a critical point in managing acceleration and effectively treats it as the superstructure of the SMBs.

In line with the analysis of mass for dynamic considerations, as stipulated in SS-EN 1991-2:6.4.6.3.22, special attention is given to the mass associated with the ballast. This analysis recognizes two ultimate cases, providing essential insights into the mass involved. The mass considerations are meticulously detailed, presenting values for both the maximum and minimum scenarios, ensuring a comprehensive approach to dynamic analysis.

The stiffness or Young's modulus of the SSCB and the surrounding soil emerges as an important factor influencing the resonance speed of the structure. An accurate estimation of stiffness is paramount, as an overestimation can result in an exaggerated resonance speed. It's crucial to highlight that the Eurocode does not prescribe specific methodologies for estimating the Young's modulus in the context of SMBs structures. This complexity arises from the composite nature of SMBs, where both the steel plate and the surrounding soil contribute to the overall stiffness, making it a dynamic and multifaceted consideration.

Another critical facet in designing structures for maximum dynamic response is the incorporation of damping. Damping plays a vital role in mitigating dynamic forces and ensuring structural stability. SS-EN 1991-2:6.4.6.3.13 offers valuable guidance on how to estimate damping for a diverse range of structures, including casted beams, reinforced concrete, prestressed concrete, steel, and composite structures. The Eurocode's recommendations for damping predominantly assume a linear damping model is represented in Table 2.6. However, this guidance recognizes that exceptions exist.

Table 2.6 Damping values based on SS-EN 1991-2:6.4.6.3.13

Bridge Type	ζ Lower limit of percentage of critical damping %	
	Span $L < 20$m	Span $L \geq 20$m
Steel and Composite	$\zeta = 0.5 + 0.12520 - L$	$\zeta = 0.5$
Prestressed concrete	$\zeta = 1 + 0.0720 - L$	$\zeta = 1$
Filler beam and reinforced concrete	$\zeta = 1.5 + 0.0720 - L$	$\zeta = 1.5$

In scenarios where the span of a bridge is shorter than 30 m, Eurocode affords designers a degree of flexibility. Designers can opt to increase damping as per Equation 26 or opt for a dynamic analysis of the interaction between train and the bridge. This flexibility acknowledges that when shorter spans are involved, the interactive mass effects between train and the bridge can curtail the maximum response during resonance. The value of $\Delta\zeta$ represents the lower threshold for critical damping, as defined in Eurocode, SS-EN 1991-2:6.4.6.44. The total damping available for the designer's use is computed through Equation 27, with the damping provided by $\Delta\zeta$ visually elucidated in Figure 2.7. This multifaceted approach to damping acknowledges the dynamic complexity of structural design and seeks to strike an optimal balance between stability and responsiveness.

$$\Delta\zeta = \frac{0.0187L - 0.00064L^2}{1 - 0.0441L - 0.0044L^2 + 0.000255L^3} \tag{26}$$

$$\zeta_{total} = \zeta + \Delta\zeta \tag{27}$$

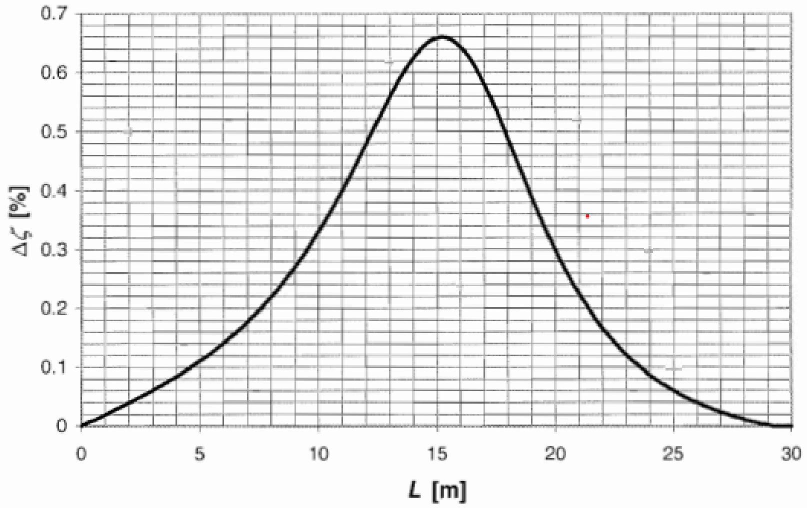

Figure 2.7 A additional damping Δζ % as a function of Span length L m based on SS-EN 1991-2:6.4.6.44.

The method employed for simulating high-speed traffic in compliance with Eurocode involves the utilization of HSLM train, consisting of two universal trains: HSLM-A and HSLM-B. For the specific dynamic analysis in question, we focus solely on HSLM-A. HSLM-A is composed of ten reference trains and serves as the basis for dynamic train signatures. Notably, for simply supported structures, the performance of HSLM-A is instrumental in determining the midspan upper bound acceleration.

Table 2.7 provides an overview of the load model HSLM-A. Each set of reference trains, denoted as A1 to A10, varies in terms of coach length, the number of coaches, bogie-distance, and point force. The highest chosen speed for analysis is guided by Eurocode, specifically SS-EN 1991-2:6.4.6.21, which dictates it should be 1.2 times the Maximum Design Speed. Importantly, this factor of 1.2 does not account for any potential future speed increases. Hence, Eurocode recommends that the designer introduce an additional factor to accommodate any such speed enhancements during dynamic analysis.

Table 2.7 Train model HSLM-A base on SS-EN1991-2:6.4.6.1.14

Universal Train	Numbers of Coaches	Length of Coach m	Length of Bogie m	Point force KN
A1	18	18	2.0	170
A2	17	19	3.5	200
A3	16	20	2.0	180
A4	15	21	3.0	190
A5	14	22	2.0	170
A6	13	23	2.0	180
A7	13	24	2.0	190

A8	12	25	2.5	190
A9	11	26	2.0	210
A10	11	27	2.0	210

For the purposes of dynamic analysis, Eurocode advises that only one track be considered for the application of loads, as stipulated in SS-EN 1991-2:6.4.6.1.23. The chosen track should be the one that results in the most unfavorable conditions. To accurately capture resonance peaks at different speeds during analysis, Eurocode suggests choosing a small speed increment.

When conducting a dynamic analysis, one key aspect to address is the Dynamic Amplification Factor DAF, represented as φ'_{dyn}. This factor is determined by evaluating the ratio between dynamic and static displacements, as outlined in Equation 28 in accordance with SS-EN 1991-2:6.4.6.53. φ'_{dyn} is instrumental in characterizing the overall dynamic behavior of the structure when subjected to dynamic loads. Notably, the calculation of φ'_{dyn} relies on a finite element solution, enabling a comprehensive and accurate assessment of the SMB's dynamic response. This approach ensures that the DAF accurately reflects the specific dynamic characteristics of the SMB and its interaction with high-speed train loads.

$$\varphi'_{dyn} = \max\left|\frac{y_{dyn}}{y_{stat}}\right| \tag{28}$$

In dynamic analysis, a Dynamic Amplification Factor DAF is employed to account for the dynamic response compared to the static response. For comparative purposes, an additional DAF is evaluated by calculating the ratio between dynamic and static moments at the crown of the SSCB, as shown in Equation 29. This additional DAF assessment aims to discern if DAF values differ based on the entity for which they are determined.

$$\varphi'_{dyn,M} = \max\left|\frac{M_{dyn}}{M_{stat}}\right| - 1 \tag{29}$$

When calculating DAFs for real trainloads and for fatigue limit states, the approach adheres to the guidelines provided in Appendix C of SS-EN 1991-2. In the case of carefully maintained track, the formulation follows Equation 30. It applies the DAF to the static response, and if a dynamic stress signal is available, it excludes the factor φ'_{dyn} in Equation 30. To account for track imperfections, the factor φ'' is applied, as defined in Eurocode by Equation 31.

$$1 + \varphi = 1 + \varphi'_{dyn} + 0.5\,\varphi'' \tag{30}$$

$$\varphi'' = \frac{\alpha}{100}\left(56e^{-\left(\frac{L_{\emptyset}}{10}\right)^2} + 50\left(\frac{L_{\emptyset} n_0}{80} - 1\right)e^{-\left(\frac{L_{\emptyset}}{10}\right)^2}\right) \geq 0 \tag{31}$$

Where,

$$\alpha = \left\{\begin{array}{cc} \frac{v}{22} & v \leq 22\,m/s \\ 1 & v > 22\,m/s \end{array}\right\} \tag{32}$$

For fatigue analysis in the context of SSCB, it is assumed that the track is carefully maintained. The design value derived from dynamic analysis is determined using Equation 33 following SS-EN1991-2:6.4.6.53. The ultimate design value for the bridge must be determined by selecting the least favorable outcome between Equation 31 and Equation 33, while also ensuring compliance with the acceleration criteria specified in SS-EN 1990:A2.4.4.2.14P.

$$\left(1 + \varphi'_{dyn} + 0.5\,\varphi''\right)x\begin{pmatrix} HSLM_L \\ or \\ RT \end{pmatrix} \qquad (33)$$

2.1.6.2 Fatigue Limit State

The Fatigue Limit State FLS in the context of Soil Metal Bridges SMBs is a critical consideration in the structural analysis and design process. FLS analysis becomes necessary because the repetitive loading imposed by dynamic train traffic can initiate crack propagation within the structure, ultimately leading to rupture. The susceptibility to fatigue rupture is influenced by two primary factors: stress variations and the number of cycles these stress variations undergo. Fatigue cracks typically originate in regions where stress concentrations are prominent, such as at the crest or valley of the corrugations or around bolt holes. However, cracks may also develop at free surfaces due to microstructural irregularities within the steel plate.

Analyzing for FLS requires an assessment of multiple locations within the SMBs that may experience significant stress concentrations. There are two frequently employed methods for FLS analysis: the Lambda method and the Palmgren-Miner rule. Both methods are detailed in Eurocode, providing designers with flexibility in selecting the most appropriate approach for their specific scenario. In the context of FLS analysis, the TRVK Bro: B.3.2.1.4j clause outlines that if mixed traffic occurs on the railway line under design, the designer is only obligated to design for FLS up to the Maximum Design Speed MDS specified for the railway line in accordance with SS-EN 1991-2:6.9.

The Palmgren-Miner rule is a methodology employed for assessing the cumulative damage and fatigue life of a structure subjected to repetitive loading, such as the dynamic stress experienced by Soil Metal Bridges SMBs due to train traffic. This rule involves a multi-step process.

First, a stress collective is computed, which entails determining the contribution of each stress range to the overall fatigue damage. This step is essential in understanding how different stress levels, occurring under various conditions, impact the structure's fatigue life. The choice to utilize the Palmgren-Miner rule is justified by recommendations in SSEN 1991-2:6.4.6.6. This rule accommodates complex scenarios by considering additional factors, including the effects of free vibrations, stress amplitudes during resonance from moving loads, and the influence of extra stress cycles generated by dynamic loading at resonance.

Furthermore, the analysis encompasses studying a range of speeds, including speeds up to the highest nominal speed Maximum Design Speed. This approach aims to identify the stress collective that best represents the cumulative damage based on the dynamic stress-time history. By examining various speeds, the analysis captures how different operating conditions affect fatigue damage accumulation. If the dynamic stress-time history is derived from a finite element model, it's important to apply amplification factors, as specified in Equation 34. These factors ensure that the analysis accounts for the entire stress signal during a single passage of the applied trainload, considering all relevant stress variations.

$$\gamma_{Ff}\Delta\sigma_i = \gamma_{Ff}\Delta\sigma_i\,(1+\varphi) = \gamma_{Ff}\Delta\sigma_i\; 1 + 0.5\varphi'' \tag{34}$$

In addition, when applying the Palmgren-Miner rule to SMBs structures subjected to HSLM-trains, an estimation of future train traffic is necessary. The rule's formulation for cumulative damage is typically defined in Equation 35. To estimate the total lifetime of the bridge, one must calculate the total cumulative damage over the course of a year, as detailed in Equation 36. This step provides insight into how fatigue accumulates over time and helps assess the structure's long-term durability.

$$D_d = \sum_i^n \frac{n_{Ei}}{N_{Ri}} \tag{35}$$

$$Lifetime = \frac{1}{D_{d,year}} \tag{36}$$

2.2 Cellular Confinement Systems CCS

Working with weak foundation soil presents a formidable challenge for engineers due to its limited bearing capacity and high compressibility. Prior to constructing superstructures, these problematic soils require treatment, prompting the development of various techniques aimed at improving soil properties and behavior. The choice of a suitable method hinges on factors like soil type and structural design requirements. Among the array of techniques available, soil reinforcement stands out as a global favorite due to its simplicity and cost-effectiveness (Vidal, 1969; Binquet et al., 1975; Paul, 1988).

The essence of soil reinforcement involves embedding load-bearing elements with robust tensile strength and stiffness into the soil. Even when dealing with soil's inherent weakness in tension, these reinforcing materials effectively absorb significant tensile stress. In the early days, materials like straws, reeds, and bamboo served as initial forms of soil reinforcement. However, the practical use of geosynthetic products for reinforcement has been recognized since the 1970s. These products, primarily composed of polymeric materials like HDPE, come in various shapes, such as planar sheets, bars, and strips, and have proven to be effective soil reinforcement solutions (Jones, 1996). Notably, among these options, cellular systems are particularly appealing due to their three-dimensional structure, setting them apart from planar geosynthetic reinforcements (Mhaiskar et al, 1996; Latha et al, 2007; Sireesh et al., 2009b; Tafreshi et al., 2013; Biswas et al. 2013; Tanyu et al., 2013). One such innovative solution is the geocell, a honeycomb-structured polymeric cellular system connected by joints (Bush et al,1990; Dean, 1990; Cowland et al., 1993; Lambert et al., 2011). The name "geocell" combines "geo" referring to soil or earth and "cell" indicating its cellular structure. Geocells encapsulate weaker materials like soil and stones within their 3D framework, offering comprehensive confinement. When geocell and the fill material work in tandem, they form a reinforced composite with enhanced stiffness and strength compared to unreinforced soil. Furthermore, this composite system excels in evenly distributing applied loads across a wider area, effectively preventing lateral material spread. In essence, geocell technology is reshaping the field of soil reinforcement, providing an innovative solution to the challenges posed by weak foundation soil.

2.2.1.1 Revolution of geocell

The concept of cellular confinement systems, which led to the development of geocells, can be traced back to the work of the US Army Corps of Engineers in the late 1970s (Webster et al., 1977). The initial geocells were constructed using materials such as paper, aluminum, and wood (Meyer, 2000; Rea et al., 1978). These early geocells were primarily designed for the transportation of military vehicles over weak subgrades. An early version, known as "sandgrids," made of plastic or aluminum, was used at the US Waterways Experimentation Station in Vicksburg, MS, USA, in 1979 (Webster, 1977). The modern form of geocells began to take shape in the 1980s, marking a significant departure from their early counterparts. Unlike planar textiles and grids, modern geocells consist of three-dimensional networks of cells filled with soil, offering several advantages, including all-round confinement through hoop stresses and a beam effect resulting from their stiff-mat configuration (Rajagopal, 1999; Leshchinsky et al., 2013; Latha et al., 2021). These advancements in design paved the way for the widespread adoption of geocells in geotechnical engineering. The inclusion of geocells in various structures has led to a range of benefits, including improved stability, climate resilience, enhanced resistance to cyclic loads, erosion control, basal support, and savings in time and cost (Rajagopal, 1997; Leshchinsky et al., 2013; Latha et al., 2021; Gedela et al., 2021). Geocells find applications in pavements, slopes, foundations, embankments, and reinforced earth RE walls. In recent years, geocells have even been utilized in heavy-duty highways and high-speed train tracks (Leshchinsky et al., 2013; Latha et al., 2021). Understanding the mechanisms behind geocell reinforcement is crucial to their effective utilization. In a network of geocells, each cell is surrounded by neighboring cells, all of which are filled with soil. External loads applied to the soil inside the geocells result in the development of additional confining stress along the cell walls (Rajagopal, 1997; Leshchinsky et al., 2013; Latha et al., 2021; Gedela et al., 2021; Bathurst et al., 1993). This increased confinement translates into apparent cohesion, enhancing the shear strength of the soil and preventing lateral spread (Garcia et al., 2021).

Moreover, the interconnected network of geocells acts as a cushion or stiffened mattress, distributing external loads over a wider area, thereby reducing stresses on the underlying soil (Zhang et al., 2009). This beam action also hinders the propagation of failure surfaces into the underlying soil, contributing to enhanced stability (Dash et al., 2007). At larger displacements, the geocell layer functions as a tensioned membrane, offering resistance to applied loads and further reducing stresses on the underlying soil (Zhang et al., 2009).

Historically, geocell layers were constructed on-site using planar geosynthetics such as geotextiles and geogrids, with cells strategically connected and filled with granular soils (Bush et al., 1990). Over the years, the geometric shape of geocells has undergone significant transformations, progressing from square, circular, rectangular, diamond, and hexagonal shapes to the current honeycomb configuration. The honeycomb design maximizes infill while minimizing the perimeter of cells, making it an ideal choice for various geotechnical applications (Gedela et al., 2021).

The materials used in geocell manufacturing have also witnessed substantial evolution. Initially fabricated from paper, aluminum, and wood (Meyer et al., 2002), geocells have transitioned to contemporary polymers. Presently, high-density polyethylene HDPE and novel polymeric alloy NPA are the commonly used polymers for geocell construction (Pokharel et al., 2010). Notably, NPA has gained popularity due to its flexibility, thermo-plasticity, and surface texture.

Modern honeycomb geocells are manufactured with surface texture to enhance their ability to mobilize greater interfacial shear strength when in contact with soils (Gedela et al., 2021). Importantly, the junctions of these geocells remain intact, even when localized straining and buckling occur in geocell walls (Dash et al., 2004; Tafreshi et al., 2016). Perforations present on geocell walls serve a dual purpose. They facilitate easy drainage, dissipating pore pressures within the cells, and provide interlocking between infill soils of adjacent geocells. This interlocking effect transforms the geocell-reinforced soil into a stiffened composite mass. Moreover, these perforations promote root growth within the cells, making them suitable for vegetation growth on geocell walls and slopes.

2.2.1.2 Configurations and Factors

This section of the chapter focuses on the factors governing the reinforcement efficiency of geocells in geotechnical engineering. The reinforcement efficiency of geocells is primarily influenced by the geocell configuration, material properties, and soil properties. The key configuration factors explored include height H, overall width b, pocket shape, pocket opening size d, pattern of arrangement for geocells made of geogrids, embedment depth u, and the number of geocell layers N. The interplay of these factors is analyzed concerning their impact on geocell performance, especially in enhancing soil strength through friction and interlocking. Additionally, the influence of geocell configuration on geocell efficiency under different levels of external loads on weak soils is discussed.

2.2.1.3 Geocell Hight

Numerous studies have explored the correlation between geocell height and its impact on performance. They consistently reveal that, as geocell height increases up to an optimal threshold, the performance of geocell-reinforced structures undergoes significant improvement. Beyond this point, the enhancement either stabilizes or diminishes. With the elevation of geocell height, the surface area of geocells also expands, resulting in heightened frictional resistance that hinders soil settling. This amplified frictional interaction between the geocell, and the soil significantly contributes to improving the effectiveness of reinforcement (Pokharel et al., 2010; Dash et al., 2001). The greater geocell height allows the geocell-reinforced soil to function as a composite unit, furnishing anchorage as shown in Figure 2.8. This composite behavior bolsters the bending and shear rigidity of geocell-reinforced structures due to an increase in the moment of inertia. Consequently, the load gets distributed over a more extensive area, ultimately leading to an enhanced load-bearing capacity and a reduction in soil settlements below (Gedela et al., 2021; Dash et al., 2001; Sitharam et al., 2005; Thallak et al., 2007; Lal et al., 2017).

Taller geocells provide increased rigidity, confining the infill soil effectively. This confinement prevents lateral movements, thereby augmenting the overall structural stability (Sitharam et al., 2005; Thallak et al., 2007; Tafreshi, 2010; Sherin et al., 2017). The resistance at the interface between soil and geocell intensifies with the height of the geocells. This heightened interlocking resistance proficiently counteracts the downward forces exerted during external load application (Dash et al., 2004; Thallak et al., 2007). Nonetheless, it is crucial to acknowledge that once a specific height is attained, local buckling and deformation of geocell walls can hinder the increase in flexural and shear rigidity. Consequently, loads are inadequately transferred through the geocell layer, resulting in performance degradation (Sitharam et al., 2005; Thallak et al., 2007; Lal et al., 2017; Dash et al., 2008; Muthukumar et al., 2019; Shin et al., 2017).

Increasing geocell height introduces challenges related to field compaction, which may lead to a reduction in the infill soil's density (Sherin et al., 2017; Tafreshi, 2009). Studies have demonstrated that geocells with lesser heights typically exhibit flexural behavior. As height increases, they transition into deep beam behavior, contributing to enhanced performance (Madhavi et al., 2008). Taller geocells can mobilize tensile strength through membrane action, effectively resisting tensile forces, further enhancing overall performance. This membrane action of geocells boosts their load-bearing capacity and stability (Dash et al., 2008). When geocells of lesser height bear a load, a linear strain distribution is observed along the geocell's depth, with the highest strain at the bottom. This behavior is analogous to a centrally loaded thin beam, where compressive strains dominate at the top, and tensile strains are prevalent at the bottom (Mhaiskar et al., 1996). Intriguingly, as geocell height increases, the strain distribution pattern undergoes a reversal. For taller geocells, the maximum strain is observed at the top of the geocell structure, decreasing progressively towards the bottom, akin to the behavior of deep beams in structural engineering.

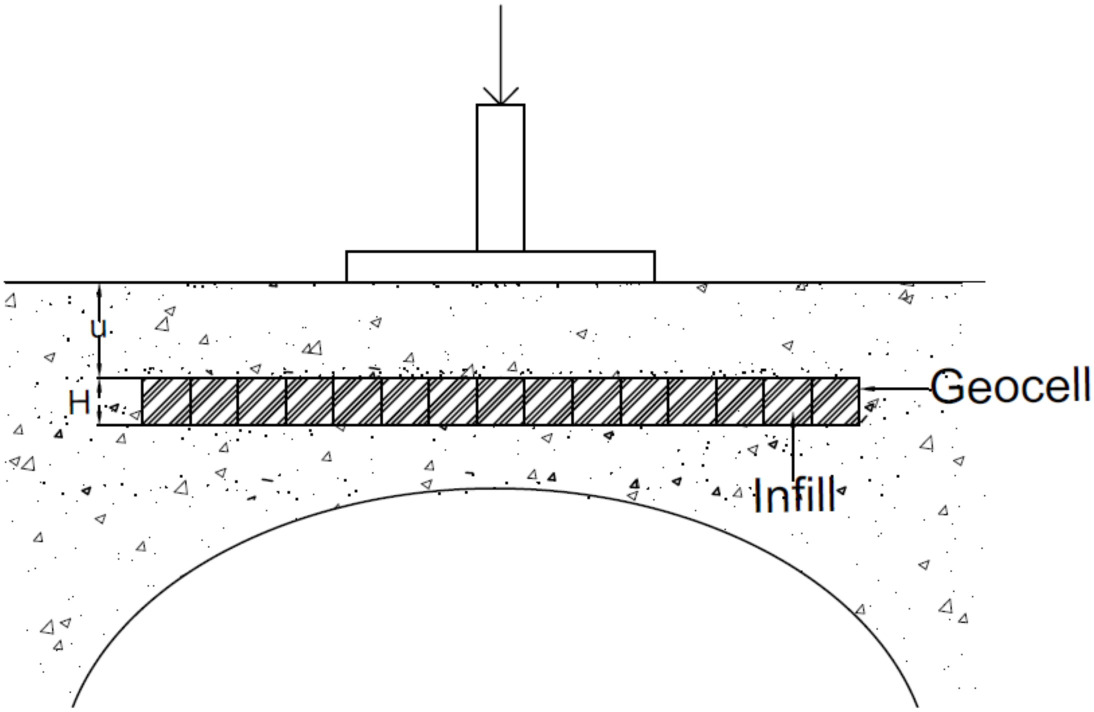

Figure 2.8 A representation of geocell reinforced Soil Metal Bridge.

2.2.1.4 Pocket size

The size of geocell pockets is a key factor in determining the confining stresses that develop within the infill soil. Researchers like Gedela (2021) and Sherin et al. (2017) have observed that there's an inverse relationship between pocket size and confining stresses. When the pocket size decreases, it boosts the additional confining stresses exerted by the geocells per unit volume of soil. This, in turn, leads to an improvement in apparent cohesion, as witnessed in studies by Mhaiskar et al. (1996) and Hegde et al. (2015). Consequently, the geocell pockets effectively contain the infill soil, resulting in controlled settlements and heaves in geocell-reinforced structures (Latha et al., 2009; Dash et al., 2001; Sherin et al., 2017). Regarding the ideal pocket size, the intuitive assumption that reducing it consistently enhances geocell performance is contradicted by prior research. Dash et al. (2008) and Kargar et al. (2017) have shown that the performance of geocell-reinforced structures improves as the pocket size decreases, but only up to a certain optimal threshold. Beyond this point, the performance enhancement stabilizes or even declines. This highlights the significance of fine-tuning the pocket size to achieve the desired performance in geocell applications.

Reducing the pocket size of geocells results in an expansion of their surface area. This, in turn, augments the active lateral pressure within the geocell wall, thus enhancing the overall rigidity of the geocell-reinforced soil composite (Dash et al., 2008; Kargar et al., 2017). However, it's crucial to acknowledge that beyond a certain point, the performance improvement becomes marginal. This is due to the development of opposing membrane stresses along the geocell walls, which can lead to local buckling and straining, ultimately diminishing the flexural and shear rigidity offered by the geocells (Dash et al., 2007). The effectiveness of geocell-reinforced beds typically improves as the height of geocells increases or their pocket size decreases. While elevating the aspect ratio of geocells, which represents the ratio of their height to pocket size, may seem like it would boost overall performance, it doesn't consistently guarantee continuous enhancement. Different pieces of literature offer conflicting insights into the ideal aspect ratio. For example, Dash et al. (2001) conducted plate load tests on foundations and suggested that the optimal aspect ratio for geocells is around 1.67. Their study found that this aspect ratio resulted in the highest load-bearing capacity and minimal settlement, indicating efficient use of geocells in foundation applications. In contrast, Krishnaswamy et al. (2000) performed embankment model studies and proposed that the optimum aspect ratio is close to 1. Their research demonstrated that nearly equal height and pocket size of geocells led to optimal performance in embankment applications. The variations in observed optimum aspect ratios can be attributed to several factors, including geocell configuration, geocell type, foundation properties, and loading conditions, as highlighted by Dash et al. (2001). These factors interact in complex ways, resulting in different performance outcomes for geocells with varying aspect ratios.

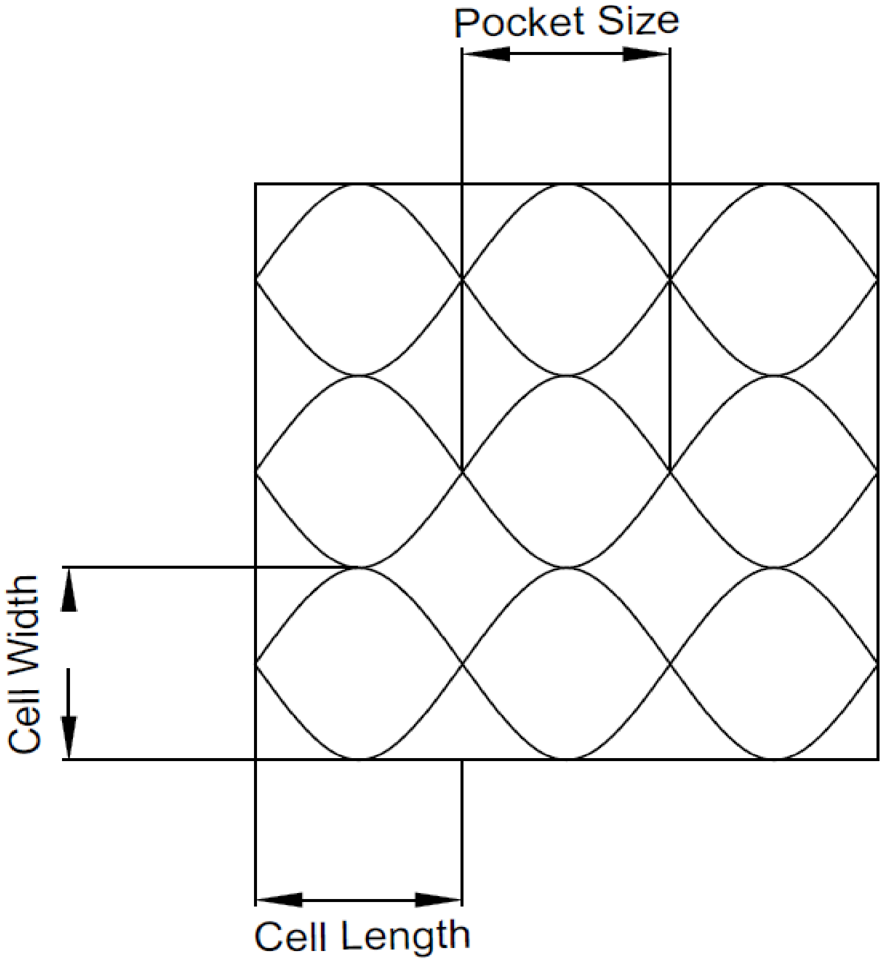

Figure 2.9 A representative of a honeycomb Geocell layout.

2.2.1.5 Width of the geocell

The utilization of geocell reinforcement layers plays a central function in the redistribution of stresses induced by applied loads within the soil. This phenomenon extends the influence of these stresses well beyond the loaded region, thus establishing robust anchorage and cohesion with the stressed soil zone. Research findings consistently suggest a positive correlation between the effectiveness of geocell-reinforced structures and the width of the geocell layer. However, this correlation holds true only up to a certain optimal width, beyond which further improvements become marginal.

Concerning the enhancement of structural rigidity, the expansion of the geocell width contributes significantly to increased rigidity. This is achieved by capitalizing on the enhanced end-bearing resistance resulting from the improved confinement of the geocell-infilled soil composite. (Dash et al., 2004; Sitharam et al., 2005; Kargar et al., 2017) support this notion. Consequently, this increased rigidity leads to a more efficient distribution of external loads across a larger portion of the underlying soil, reducing localized stress concentrations.

One notable advantage of geocell-reinforced structures is the limitation of the zone of influence. In contrast to unreinforced soil, where this zone extends to approximately twice the width of the loaded area, geocell-reinforced structures subtly curtail the extent of influence just beneath the geocell layer. This characteristic effectively minimizes surface heaving and encourages uniform settlement patterns (Dash et al., 2001; Sitharam et al., 2005; Dash et al., 2008; Kargar et al., 2017).

Expanding the width of geocell layers offers distinct advantages by encompassing a greater number of cells, thus contributing to an enhanced reinforcement effect, as documented by (Saride et al. 2009). However, it is crucial to acknowledge that wider geocell layers, while advantageous for load distribution and settlement control, present certain challenges. Notably, the phenomenon of local buckling and straining of geocell walls induced by larger widths may mitigate the benefits derived from the flexural and shear rigidity of the geocells, as highlighted by (Sitharam et al. 2005). Additionally, examinations of geocells post-load tests reveal higher strains and deformations of the buckling type, primarily in areas under and surrounding the loaded zone, while sections of the geocell mattress distant from the load remain structurally intact (Sitharam et al., 2005; Dash et al., 2007). Moreover, extending geocells beyond the influence zone of footings offers an added advantage by creating secondary anchorage through frictional and passive resistance at the interface between the soil and the geocell (Dash et al., 2001; Lal et al., 2017; Kargar et al., 2017).

2.2.1.6 Geocell Pocket Shape

Geocell technology has undergone substantial advancements, not only in terms of material composition but also in the geometric design of geocell pockets. These pocket shapes have evolved through various configurations, including square, circular, rectangular, diamond, and hexagonal, before culminating in the widely adopted honeycomb shape. In Figure 2.9, it provides a schematic representation of the diverse pocket shapes employed in earlier studies, while Figure 2.10 showcases photographs of geocells featuring distinct pocket shapes. Research findings, as elucidated by (Sherin et al. 2017), suggest that whether geocell pockets take on square or circular configurations and are constructed with identical materials, they exhibit comparable improvements in soil reinforcement, provided that the material quantity remains consistent. This underscores the significance of considering both pocket shape and material quantity when optimizing geocell performance.

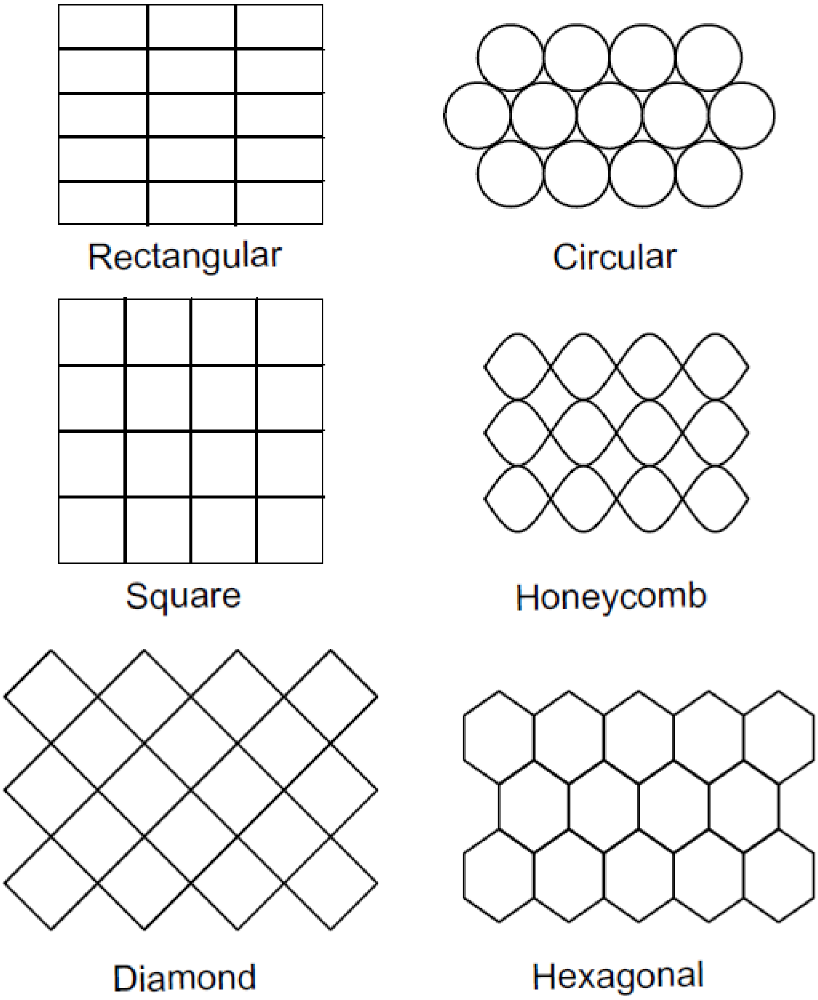

Figure 2.10 Schematic representation of geocells with different pocket shapes.

The incorporation of the honeycomb configuration in geocell pocket designs, driven by the objective of maximizing infill material containment while minimizing cell perimeter (Gedela et al., 2021), not only enhances load-bearing capacity but also offers practical advantages, including efficient storage, handling, and transportation.

Vertical load stability has emerged as a critical attribute of honeycomb-shaped geocells, as evidenced by their ability to maintain structural integrity under vertical loads, a fundamental characteristic that significantly enhances their effectiveness in soil reinforcement (Leshchinsky et al., 2013). This stability plays a pivotal role in preventing deformation and ensuring consistent geocell performance. Moreover, the honeycomb shape excels in controlling both vertical and horizontal deformations of geocells, even when they are filled with less stable soils (Leshchinsky et al., 2013). This capability is essential for preserving the structural integrity of geocells and sustaining their long-term performance.

2.2.1.7 Pattern Arrangement

When contemplating geocell design, the arrangement pattern of these cellular structures significantly influences their performance and effectiveness. Geocells can be designed in two primary configurations: the diamond and chevron patterns, each with its unique advantages and implications for soil reinforcement. Schematic depictions of these patterns can be found in Figure 2.11. In both cases, the manufacturing process starts with erecting geogrid strips vertically along the transverse direction. Subsequently, diagonal strips are added between the transverse grids using bodkin joints to ensure the structural integrity of the geocell (Dash et al., 2001; Krishnaswamy et al., 2000).

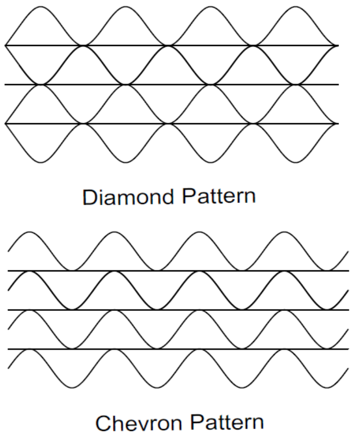

Figure 2.11 Different geocell fabrication patterns.

When deciding between the diamond and chevron patterns, several considerations significantly impact geocell performance. These factors include joint density, enhanced rigidity, and flexural rigidity, each of which requires careful analysis. Regarding joint density, the chevron pattern stands out as the preferred choice due to its higher joint density. This configuration offers a distinct advantage over the diamond pattern as it ensures that the failure of some joints does not lead to the failure of the entire geocell structure. This redundancy in joint connections strengthens the overall reliability of the geocell mattress, providing a robust and resilient reinforcement solution. Moving on to enhanced rigidity, the chevron pattern proves superior, especially when considering the same plan area of geocells. The increased rigidity in the chevron arrangement is a direct result of its higher joint count. Moreover, forming joints in the chevron pattern is a simpler process, involving the connection of only two vertical surfaces. In contrast, the diamond pattern requires connections with three grids, making it a more intricate and labor-intensive option (Krishnaswamy et al., 2000). This ease of assembly and enhanced rigidity make the chevron pattern an attractive choice for soil reinforcement projects.

Finally, flexural rigidity becomes a crucial factor in geocell performance, especially in scenarios involving significant settlements. Empirical studies highlight the chevron pattern's effectiveness in this regard. When soil experiences shear failure during substantial settlements, the surrounding soil deforms and rises to the surface, reducing the geocell infill density. In such conditions, a significant portion of the applied load is supported by the geocell walls. In this context, the chevron pattern, with its elevated flexural rigidity, provides substantial support for loads compared to the diamond pattern (Dash et al., 2001). This attribute is particularly valuable when considering geocell-reinforced foundations subjected to significant settlements, ensuring the structural integrity of the geocell system remains intact.

2.2.1.8 Embedment depth of geocell

The importance of embedment depth cannot be overstated when assessing the performance of geocells. While situating the geocell layer just below the rail track might seem like a straightforward choice, it can result in the accumulation of higher localized stresses within the geocell walls, potentially leading to buckling failure (Sherin et al, 2017). Additionally, placing geocells at shallower depths imposes limitations on the ability to effectively confine soil within the geocells and maintain the desired friction at the upper and lower boundaries of the geocell layer. This limitation arises due to a reduction in normal stress resulting from the overburden (Tafreshi et al, 2010; Yang et al, 2010; Mehdipour et al, 2013; Sitharam et al, 2006).

Understanding the role of the soil cushion in conjunction with geocells is essential, viewing it as an integral part of a larger system. The soil cushion, positioned between the footing and the geocell layer and between two geocell layers, plays a significant role in enhancing the overall system's performance. It facilitates the development of effective frictional interactions at the interfaces between geocells and the soil, functioning as a rigid system that helps distribute the load over a broader area of the underlying soil (Dash et al, 2007; Thallak et al, 2007; Tafreshi et al, 2010; Davarifard et al, 2015).

The load dispersion mechanism, supported by the sand cushion, is crucial in comprehending the behavior of geocell-reinforced systems. Research has indicated that when the geocell layer is situated at the optimal depth, horizontal strains along the geocell wall's height gradually decrease from top to bottom (Dash et al, 2007). This underscores the effectiveness of the soil cushion in shielding the geocell layer from direct load application. Moreover, the soil cushion serves a crucial role in facilitating drainage during the consolidation of soft soil beneath it (Sitharam et al, 2005;

Thallak et al, 2007). This drainage capability assumes particular significance under cyclic loading conditions (Bagli, 2022).

The depth at which geocells are embedded has far-reaching consequences for their performance. Placing geocells at depths lower than the optimum results in an insufficient depth for the soil cushion to mobilize frictional resistance against shearing, leading to inadequate geocell reinforcement (Thallak et al, 2007; Sherin et al, 2017). Conversely, embedding geocells at depths exceeding the optimum diminishes their composite beam-like behavior, causing the upper cushion and the geocell-reinforced soil to act as separate entities. This leads to the shearing of the upper soil cushion and lateral displacement of the soil between the footing and the geocell-reinforced soil composite. Consequently, the reinforcement effect is nullified, and the geocell-reinforced soil behaves similarly to unreinforced soil (Dash et al, 2007; Dash et al, 2001; Sherin et al, 2017). Furthermore, at greater embedment depths, a substantial portion of the geocell-reinforced soil composite lies beyond the influence zone of the applied load, further diminishing the effectiveness of geocell reinforcement (Thallak et al, 2007; Tafreshi et al, 2010; Khalaj et al, 2015; Mehdipour et al, 2013).

It's worth noting that in specific situations, especially when dealing with cohesive soils, placing the footing load directly on the geocell mattress without any soft soil cushion can be advantageous. This approach helps mitigate the lateral compression of cohesive soil, which could otherwise compromise the performance of geocell reinforcement (Sitharam et al, 2005).

2.2.1.9 Number of layers

Multiple layers of geocells are often employed in geotechnical applications to maximize their interactions with the surrounding soil as illustrated in Figure 2.12, An exemplar depiction of a soil metal bridge reinforced with multiple geocells. This approach is rooted in the belief that increased layers can lead to enhanced stability and load-bearing capacity. However, it is essential to critically assess this assumption and consider the research findings that have shed light on this matter.

Numerous benefits arise from the utilization of multiple geocell layers, one of the primary benefits of increasing the number of geocell layers is the enhancement of soil-geocell contact area. This expansion of contact area can lead to a substantial increase in frictional resistance, which is essential for stabilizing the soil metal bridge. The greater contact area also promotes a more effective confinement effect, preventing lateral soil movement beneath the geocells. This effect is further accentuated by the homogeneous stress distribution that multiple geocell layers provide below the railtrack (Mehdipour et al., 2013; Davarifard et al., 2015). With the addition of more geocell layers, the volume of soil subjected to reinforcement grows. This increase in the reinforced soil volume results in an overall improvement in stiffness, contributing to the stability and load-bearing capacity of the soil (Pokharel, 2010; Tafreshi et al., 2016). The enhanced stiffness can help distribute loads more evenly, reducing the risk of settlement and structural damage. Multiple geocell layers below the loaded area can effectively encase the entire pressure bulb within the ground. This encasement arrests both lateral and vertical deformations, ensuring that the foundation remains stable and resilient under various loading conditions (Tafreshi et al., 2015; Davarifard et al., 2015).

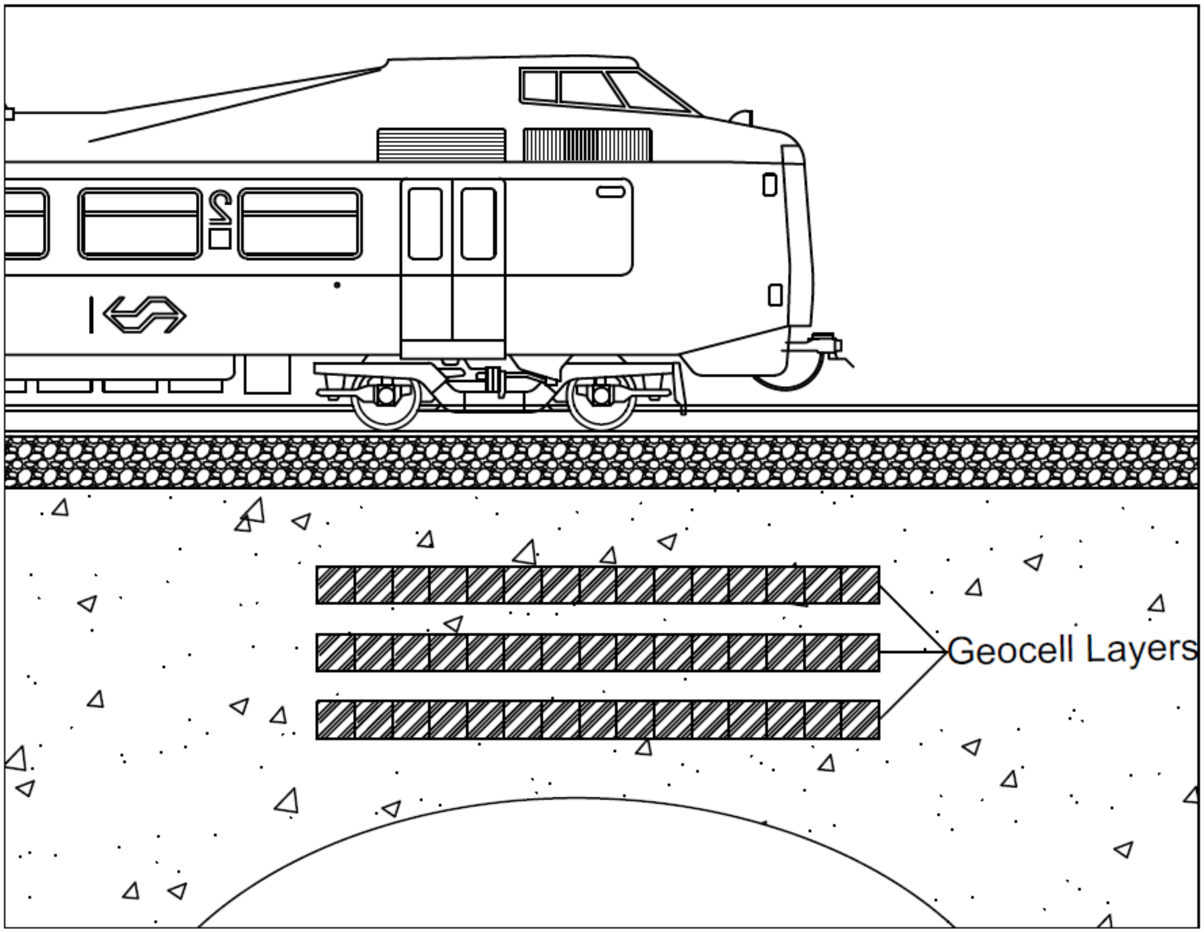

Figure 2.12 A representative illustration of a multi-Geocell reinforced Soil metal bridge.

Exploring the utilization of multiple geocell layers opens a critical discussion about the inherent limitations and essential considerations that must be thoroughly assessed. The previously conducted research suggests that the benefits of geocell reinforcement do not increase linearly with the number of geocell layers beyond a certain limit determined by the applied load. Beyond this point, the contributions of additional layers to overall strength and stiffness improvement become minimal (Tafreshi et al., 2015). Therefore, designers must carefully assess the specific project requirements to determine the optimal number of layers. To maximize the effectiveness of geocell layers, they should be strategically placed within the influence zone of the applied loads (Tafreshi et al., 2012). Geocell layers located outside this zone do not experience significant stresses from the load, resulting in minimal contributions to strength and stiffness improvement. The resilient characteristics of geocells, such as accumulated plastic strains and total settlement reduction, reach their peak improvement at a particular optimum number of geocell layers. Beyond this point, further increases in layer count have minimal influence (Khalaj et al., 2015). This is similar to static loading conditions. Under cyclic loading conditions, the rate of improvement provided by additional geocell layers becomes insignificant at higher numbers of load cycles for heavily reinforced systems. This contrasts with static loading conditions, where higher settlement levels yield greater improvement (Tafreshi et al., 2010; Yang, 2010; Sitharam et al., 2006; Davarifard et al., 2015).

In an extensive study by (Kargar and Hoessini 2017), the impact of geocell layering on soil reinforcement was thoroughly investigated. Surprisingly, their research uncovered a counterintuitive outcome - an increase in the number of geocell layers did not consistently lead to improved performance. Specifically, it was observed that the inclusion of additional layers resulted in a decrease in the strength and stiffness characteristics of soil beds reinforced with geocells. This phenomenon was particularly pronounced in two-layered geocell configurations, where tensile strains at the lower section of the geocells not only disrupted the continuity of the cells but also caused them to separate into distinct units. This disruption within the geocell layers posed challenges in achieving integrated performance and effective stress transfer to the underlying soil depths (Tafreshi et al., 2012). Similarly, in the context of four-layered geocell configurations, researchers encountered a different set of challenges. Tensile strains within the geocells were found to be inadequately mobilized, resulting in a less-than-expected improvement in the soil's strength and deformation characteristics. These observations contradicted prior research that had favored the utilization of multiple geocell layers separated by a layer of soil. However, it's important to note that while Kargar and Hoessini's study shed light on the potential disadvantages of increasing the number of geocell layers without vertical spacing, a more comprehensive perspective is needed. Different scenarios and objectives can yield divergent outcomes. To illustrate this point, (Mehdipour et al. 2013) conducted numerical simulations to explore the influence of varying geocell layer counts in slope stability, specifically focusing on the factor of safety FOS. Their findings presented an alternative viewpoint - an increase in the number of geocell layers could, in fact, enhance the FOS of geocell-reinforced slopes. This improvement in FOS was attributed to the heightened rigidity of the slope, which effectively pushed the slip surface away from the slope. Notably, the initial geocell layer played a significant role in resisting bending and shear deformations, while the subsequent layers primarily contributed to mitigating lateral deformations.

2.2.1.10 Geocell Properties

The stiffness of the geocell material is a fundamental property that underpins its performance and behavior in various applications. It is essential to understand how stiffness influences geocells, especially concerning their ability to counteract membrane stresses and provide enhanced load support. One of the primary functions of geocells is to distribute loads effectively and prevent the development of excessive membrane stresses within the cell walls. To achieve this, the stiffness of the geocell material must be adequate.

Surface roughness is another fundamental property of geocells that has garnered significant attention in recent research studies. The roughness of geocell walls has been found to have a substantial impact on their performance, and several studies have explored this aspect in depth (Garcia et al, 2021; Gedela et al, 2021; Hegde et al, 2015). The findings from these studies highlight the importance of surface roughness in influencing the behavior of geocell-reinforced structures. Research conducted by Hegde et al. (2015) and Biabani et al. (2016) demonstrated that an increase in the roughness of geocell walls leads to a corresponding increase in the angle of interface friction between the cell walls and the infill soil. This increase in frictional resistance is significant because it resists the applied load and redistributes it over a larger area. In practical terms, this means that geocells with rough surfaces can effectively enhance the stability and load-bearing capacity of the soil they are reinforcing. However, that extreme roughness of geocell surfaces may not always yield positive results. Zhang et al. (2009) reported that extremely rough surfaces could have a weakening effect on the strength and deformation characteristics of geocell-reinforced structures. Therefore, there exists a delicate balance between surface roughness and performance, and it is essential to consider the specific project requirements and soil conditions when designing geocell-reinforced structures.

The studies conducted on geocells present an interesting perspective on the importance of surface roughness. While some studies emphasize its role in enhancing performance, others, such as Hegde et al. (2017), suggest that the surface roughness of geocell walls is not as critical as the tensile strength of the geocells. This divergence in viewpoints highlights the complexity of geocell behavior and the need for a holistic approach to design and analysis.

One intriguing aspect is the influence of wall roughness on analytical models used to predict the strength and deformation characteristics of geocells. Zhang et al. (2009) and Maheshwari et al. (2017) observed that in models where interface friction is considered, the computed deformations of geocells were generally less than in models where interface friction was omitted. This underscores the importance of incorporating surface roughness into analytical models for accurate predictions.

In addition to surface roughness, the stiffness of geocells is a critical property that significantly affects their performance in various geotechnical applications. Geocells possess unique tensile and bending stiffness due to their three-dimensional honeycomb-like structure, which sets them apart from traditional planar geosynthetics. Studies conducted by Pokharel (2010) and Sherin et al. (2017) have highlighted the exceptional tensile and bending stiffness exhibited by geocells. This stiffness is a direct result of their geometric configuration, which allows them to distribute loads effectively and resist deformations. Compared to planar geosynthetics, geocells offer superior stiffness characteristics.

The high stiffness of geocells has significant implications for their load-bearing capacity. Yang (2010) and Wang et al. (2013) have shown that geocells, due to their increased stiffness, provide greater load-bearing capacity and reduce lateral deformations under both static and cyclic loading scenarios. This property is invaluable in applications where structural integrity and stability are paramount. Another critical aspect related to stiffness is the enhancement of confining stresses along the walls of geocells. (Tafreshi et al. 2015, Hegde et al. 2017, and Sireesh et al., 2009) have documented how the stiffness of geocells contributes to the development of confining stresses, which, in turn, improve their performance in various geotechnical applications.

CHAPTER 3 SOIL-STRUCTURE INTERACTION OF HIGH-SPEED TRAINS OVER SOIL METAL BRIDGES

3.1 Introduction

An open channel conveying water beneath a road is the typical design of a metal culvert, a man-made construction. Metal culverts are common in urban areas and aid with stormwater management, erosion control, and the preservation of a city's water system. Early travellers were concerned due to these structures generated noises as they vibrated beneath their weight, nevertheless. These worries are now a thing of the past owing to the development of metal culverts over the years. Corrugated steel plate CSP has been successfully used in the construction of culverts and storm sewers in North America and other countries since 1896. It keeps delivering a long service life in installations that handle a wide range of soil and water conditions. As the concept developed, wider span SMBs evolved. Several studies have been conducted to investigate the behavior and performance of SMBs. El-Sawy's (2003) research highlights the limitations of 2D Models in analyzing SMBs and proposes the use of 3D FE-modelling to improve accuracy in design and analysis. Flener's (2003) study involves field instrumentation on a long-span steel arch railway bridge, measuring strains and displacements to provide insights on the performance and behavior of SMBs under different loading conditions. Abdel-Sayed and Salib (2002) used ABAQUS plain-strain FE-analysis to investigate the minimum soil cover depth required for SMBs to prevent failure under loading conditions. Sutubadi and Khatibi (2013) utilized PLAXIS to study the variation of soil properties in parametric studies with 2D finite element models according to Mohr-Coulomb theory. They investigate various soil parameters, including cohesion, Young’s modulus, internal friction angle, Poisson ratio for soil, and dilatation angle to determine their impact on SMBs strength and load-carrying capacity. Yeau et al.'s (2013) parametric study investigates the effects of different soil cover depths on SMBs behavior and performance under loading conditions. The study concludes that normal forces and deflections decrease as the soil cover depth increases, and crown deflections depend more on the SMB shape than the span length.

Numerous other studies have been done on the behaviour of SMBs on both the soil side and the effluent side (Bakht 1980; Webb 1995; Mai 2013). These investigations have demonstrated that SMBs typically offers remarkable durability with great load-bearing capacity under various loadings conditions. However, studies focusing on understanding the behavior of these structures under heavy dynamic loads has not been widely investigated. The performance of these structures is different when subjected to dynamic loads from the passing of heavy trains. This dynamic loading can cause significant deformation, stress, and strain on the bridge structure, which may lead to reduced safety and serviceability.

To better understand the behavior of SMBs, a validation three-dimensional model has been developed using finite-element analysis to investigate the nonlinear response of both the structure and soil during backfilling. Plasticity-based procedure utilizing the action compaction method introduced by Ezzeldin and El Naggar (2022) has been used to simulate the effect of soil compaction on the metal bridge response during backfilling. The results of the model were then compared to the actual field study results conducted by Webb (1999) to validate the developed model. Following the successful validation of the initial model, the present study aimed to further investigate the behavior of soil metal bridges SMBs under dynamic train loads. To thoroughly examine the performance of SMBs, a total of 15 3D models were created using varying soil cover depths ranging from 2 to 4 m, which were subjected to a range of train speeds including 100, 150, 200, 250, and 300 km/h. The dynamic effects of these loads on the SMBs behavior were evaluated using advanced finite element techniques, with the analysis focusing on key factors such as crown deformations, bending moments, and thrust forces. The main goal of this investigation is to provide meaningful viewpoints regarding the pivotal function of soil cover depth in guaranteeing the secure and reliable operation of soil metal bridges in high-speed railway systems.

3.2 The Considered Field Study

The implementation of the structural plate metal arch culvert in an end-to-end arrangement within a pre-excavated trench is a standard construction technique frequently utilized in transportation and drainage projects. It is generally recognized as a soil metal bridge. As mentioned earlier, the monitoring results of the well documented field study by Webb (1999) is used in this study to validate the developed numerical model. In this case study, the SMB was situated with it top approximately 0.6 m 2 ft above the existing ground surface, thereby providing a level surface width of about 15 m 50 ft over the entire span of the metal bridge. To ensure stability, the structure was founded on reinforced concrete strip footings with elastic modulus of 30 GPa and Poisson's ratio of 0.3, with reinforced concrete blocks employed at the outer end of the SMB to contain the backfill and prevent it from spreading. The metal bridge utilized in the experiment was of the Type 108A30 nongalvanized corrugated steel arch variety, with a span of 9.50 m 31 ft 2 in. at the footings and a total rise of 3.7 m 12 ft 1 in. as shown in Figure 3.1. The culvert was fashioned from structural plates with 152 × 51 mm 6 × 2 in. corrugations, with a plate thickness of 5.5 mm 0.218 in., specified as 5 gauge. Unlike conventional metal arch culverts that are reinforced with longitudinal thrust beams and circumferential stiffeners to enhance their strength, the metal bridge employed in the experiment was subjected to testing without these supplementary supports. The trench was filled with backfill material, and a shallow earth embankment was erected over the SMB in a layered fashion. Existing site material excavated from the trench was employed for backfilling the SMB and constructing the embankment. The backfilling material comprised well-graded sand with gravel and had one percent fines, per ASTM D 2487 (2017). The soil material properties are presented in Table 3.1. The construction process involved compacting the structural backfill and constructing an embankment over the culvert. A 1.8 m 5.9 ft soil cover was then added to the top of the embankment.

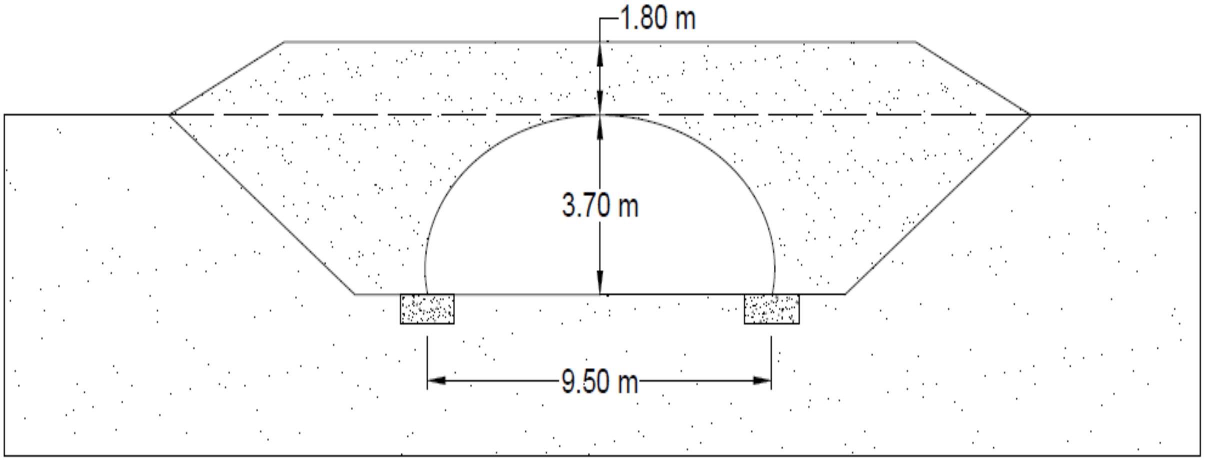

Figure 3.1 Cross-section view of the Full-scale field test after Webb 1999.

Table 3.1 Employed soil Material properties in Webb 1999 field test.

Property	Loose	Dense	Native	Unit
Soil Model	Hardening Soil	Hardening Soil	Hardening Soil	-
Type	Drained	Drained	Drained	-
$\boldsymbol{\gamma_{unsat}}$	20	18.5	20	kN/m^3
$\boldsymbol{\gamma_{sat}}$	20	18.5	20	kN/m^3
E_{50}^{ref}	6700	14.3E3	20.0E3	kN/m^2
E_{oed}^{ref}	6700	14.3E3	19.71E3	kN/m^2

E_{ur}^{ref}	20.1E3	42.9E3	60.0E3	kN/m^2
v_{ur}	0.2	0.2	0.2	-
m	0.5	0.5	0.5	-
c'_{ref}	1	1	1	kN/m^2
φ phi	34	38.5	43	°
ψ psi	0	0	0	°

During the backfilling process, the structural backfill material was spread in a manner that aligns with the culvert's longitudinal axis placed and compacted with precision to ensure ideal density. This was accomplished using either a walk-behind vibratory plate compactor or a ride-on vibratory roller, with the objective of reaching 95% of AASHTO T-99 maximum dry density. During the compaction process, an issue emerged wherein the crown of the structure experienced peaking, primarily as a consequence of lateral forces exerted during the placement of soil layers approximately 2.4 to 2.7 m 8 to 9 ft of backfill on the sides. In response to this problem, a remedial approach was implemented. To counteract the peaking deformation, a practical solution was devised involving the top-loading of the soil metal bridge. This was achieved by adding weight to the top of the structure. Specifically, concrete blocks were positioned atop the crown, creating a concentrated weight-bearing point.

3.3 Finite Element Model Development

3.3.1 Soil Profile and Compaction Procedures Techniques

Webb (1999) field test has been modelled after the HSS profile. To simulate the behavior of many soil types, including both soft and stiff soils, Shanz (1998) developed the Hardening Soil model. Soil exhibits a diminishing stiffness and simultaneously develops irreversible plastic stresses when subjected to primary deviatoric loading. The observed relationship between the axial strain and the deviatoric stress can be well approximated by a hyperbola in the special case of a drained triaxial test. Kondner (1963) first proposed such a link, which was then applied to the well-known hyperbolic model Duncan and Chang (1970). However, the Hardening Soil model vastly outperforms the hyperbolic model, by first switching out the theory of elasticity for the theory of plasticity, then by accounting for the soil's dilatancy, and last by introducing a yield cap. The constitutive law of soils is described by a collection of mathematical equations in the Hardening Soil model. The Plaxis3D Material Models Manual (2022) includes an extensive presentation of the constitutive equations. Conventional triaxial compression tests on the soil can be used to determine the model parameters required for the Hardening Soil model. The Secant stiffness in standard drained triaxial test E_{50}^{ref}, Unloading/reloading stiffness E_{ur}^{ref}, the tangent stiffness for primary oedometer E_{oed}^{ref}, the elastic unloading-reloading Poisson's ratio v_{ur}, the angle of dilation ψ, and the Mohr-Coulomb strength parameters c and φ are the fundamental parameters of the Hardening Soil model.

For primary loading, the stress-strain behavior exhibits a strong nonlinearity. A primary loading stiffness modulus that is dependent on confining stress is the value E_{50}. For little strain, E_{50} is utilized instead of the initial modulus E_0 as it is more challenging to determine tangent modulus experimentally. The other stiffness parameter is the stress dependent stiffness modulus for unloading and reloading stress paths E_{ur}. The plastic soil stiffness parameter E_{50}^{ref} and E_{ur}^{ref} are calculated as:

$$E_{50} = E_{50}^{ref} \left(\frac{\acute{c} \cos \acute{\varphi} - \acute{\sigma}_3 \sin \sin \acute{\varphi}}{\acute{c} \cos \acute{\varphi} + p^{ref} \sin \acute{\varphi}} \right)^m \qquad (37)$$

$$E_{ur} = E_{ur}^{ref}\left(\frac{\acute{c}\cos\varphi - \acute{\sigma}_3 \sin\sin\varphi}{\acute{c}\cos\varphi + p^{ref}\sin\varphi}\right)^{m} \tag{38}$$

Where E_{50}^{ref} is the reference stiffness corresponding to the reference stress p^{ref} which is set as $100\ kN/m^2$ in Plaxis as a default value. E_{ur}^{ref} is the reference modulus for unloading and reloading corresponding to the reference stress $p^{ref} 100\ kN/m^2$. Note that E_{ur}^{ref} equal to 3 E_{50}^{ref} in Plaxis default settings.

To control the amount of the plastic strains that result from the yield cap, another input parameter called the reference oedometer modulus E_{oed}^{ref} is utilized. The oedometer modulus E_{oed}^{ref} follows the stress dependency law similarly to the triaxial moduli:

$$E_{oed} = E_{oed}^{ref}\left(\frac{\acute{c}\cos\varphi - \acute{\sigma}_3 \sin\sin\varphi}{\acute{c}\cos\varphi + p^{ref}\sin\varphi}\right)^{m} \tag{39}$$

The power m indicates the degree of stress dependence. Soos von 2001 reported a range of m values from 0.5 to 1 in different soil types with the values of 0.9-1 for clay soils, in order to approximate a logarithmic stress dependency. In Obrzud & A.Truty (2018) Hardening Soil's Soil handbook, correlations from Hicher (1996) and Viggiani and Atkinson (1995) are also mentioned.

Hicher (1996) Correlation:

$$m = 1.13 - \frac{49}{LL+78} \tag{40}$$

Viggiani and Atkinson (1995) Correlation:

$$m = 1 - \frac{10.83}{P.I+18.7} \tag{41}$$

v_{ur} stands for the poisson's ratio of unloading to reloading. The fact that v_{ur} is not the standard poisson's ratio should be noted. It should be left at the default value of 0.2 in the absence of lab data.

3.3.2 Compaction Measures and Procedures

Action compaction methods and post-compaction methods are the two primary divisions of compaction simulation approaches. These classifications are based on the kind of loading that was utilized to model the compaction loads. Action compaction is the process of simulating the compaction in terms of direct contact with the surface of the backfill layers. On the other hand, simulating the compaction in terms of direct contact with or near the buried structure is a post-compaction approach. Three distinct modelling techniques have been provided by McGrath et al (1999) to simulate the compaction effect of backfill layers on corrugated culverts as shown in Figure 3.2. The first method involved applying vertical loads to each layer to simulate the compactor's weight a technique first proposed by Katona (1978). The second method imitated a squeezing effect by applying vertical loads to the top and bottom of each backfill layer. The third method involved applying horizontal forces directly to the circumference of the culvert to consider lateral stress. The first two modelling techniques are recognized as an action compaction method while the third technique provided by McGrath et al. (1999) is to be considered an example of a post compaction method.

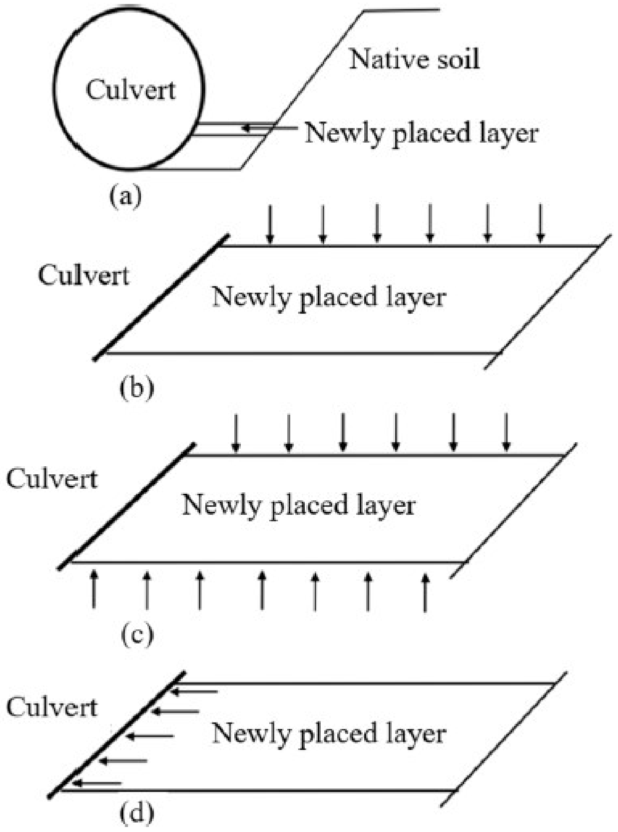

Figure 3.2 Schematic illustration of the three approaches for simulating compaction effort by McGrath et al 1999.

While the methodology proposed by McGrath et al. (1999) displayed some strengths, it's important to note certain limitations. The first and second methods stand out for their ability to simulate the deformation of culverts caused by compaction forces, offering an advantage in this regard. However, they both rely on elastic soil models, which prove inadequate when modeling the backfilling process. The issue arises when compaction loads are removed, as elastic soil models tend to generate a rebound effect in the structure's deformations and internal forces. This is due to the fact that elastic models exhibit significantly increased stiffness at extremely low stresses, which doesn't accurately represent real-world behavior. To address this concern, more precise hyperbolic soil models, such as the hardening soil model with small strains HSs, are recommended. These models can better capture the response of the culvert even after compaction loads have been eliminated. In contrast, the third method, although simpler, is considered less sophisticated because it relies on factors like soil friction angle and the specific properties of the compactor roller in use, making it less accurate in certain scenarios.

Taleb and Moore (1999) proposed an alternative approach to simulate soil compaction, specifically designed to complement elastic-plastic soil models. This method offers a straightforward way to assess the potential consequences of soil compaction on both flexible and stiff culverts. The fundamental concept involves applying the significant horizontal earth pressure that remains within the soil immediately following compaction. This passive earth pressure is akin to the maximum horizontal pressure that a purely frictional soil can withstand.

The distinctive response of flexible and rigid structures to this additional lateral earth pressure is a key aspect of this method. For flexible structures, the application of this horizontal pressure leads to deformation, which in turn alleviates a substantial portion of the increased lateral earth pressure. Conversely, rigid constructions do not deform and continue to be influenced by the changing horizontal ground pressures, particularly in regions near the crown, resulting in variations in thrusts and moments. However, it's essential to note the limitations of this approach. It does not account for the plastic strains that may occur during compaction, as it assumes the maximum post-compaction stress associated with purely frictional material. This approach overlooks the possibility of lateral extension caused by the kneading of the soil, which is a potential source of deviation from real-world conditions.

To further enhance the straightforward method initially introduced by Taleb and Moore (1999), to validate its efficacy through comparative analysis with buried pipe tests, Elshimi and Moore (2013) put forward a novel semi-empirical approach. This approach involves the introduction of an initial horizontal stress equal to the passive earth pressure that Taleb and Moore originally proposed for purely frictional material, but it's multiplied by an empirical factor known as the kneading coefficient Kn. The primary objective of this modification is to specifically account for the influence of soil kneading during the compaction process. In essence, the value of Kn, which can range up to 2, is incorporated into the calculation of the horizontal stress applied to the new soil layer at the ground surface. This adjustment allows for the inclusion of a nonzero cohesion value for the soil without violating the frictional-cohesive soil failure criterion. This semi-empirical approach offers a more comprehensive perspective by considering the impact of soil kneading on the compaction process, which the original method overlooked. It provides a flexible framework for assessing the behavior of buried pipes under various conditions, considering both frictional and cohesive aspects of soil behavior.

The approach of imparting horizontal lateral stresses, as proposed by Ezzeldin and El Naggar in (2022), builds upon the same concept as the technique outlined by McGrath and colleagues in (1999) for applying lateral nodal forces. Rather than utilizing nodal point loads, Ezzeldin and El Naggar's method replicates the compaction load by imposing a horizontal linear ground pressure on the culvert body. Ezzeldin and El Naggar introduced several modifications to the previously mentioned method developed by McGrath et al. These changes encompass the utilization of the HSs soil model, recognized for its accuracy in describing material behavior under small strains. This choice is aimed at addressing issues such as soil model rebound and the development of internal forces that occur when compaction loads are removed. Additionally, Ezzeldin and El Naggar's approach involves categorizing the backfill soil state as either loose or dense based on the compaction modeling method employed. Furthermore, Ezzeldin and El Naggar extended their methodology by incorporating specified horizontal displacements, prescribed horizontal displacements, prescribed horizontal lateral stresses, and prescribed vertical dynamic surface loads. These vertical and horizontal displacements are determined based on the expected deformations resulting from the compaction of loose backfill soil into a thick compacted soil. This comprehensive approach takes into account a wide range of factors, including soil behavior under small strains, compaction load effects, and the states of backfill soil. It provides a more nuanced and adaptable framework for simulating the behavior of culverts and associated soils under various loading conditions.

3.3.3 Compaction Simulation

To safeguard the structural integrity of the SMB metal sheets during construction, a common practice involves applying less compaction effort to the layers near the crown level compared to those in the side backfill. Typically, compaction is achieved through the use of vibratory compactors over a specified number of rounds. However, it's important to note that the magnitude of the surface loads used to simulate compaction by applying vertical surface loads is not fixed. These compaction loads are influenced by both the centrifugal forces generated by the compactor rollers and the deadweight of the compactor itself. The surface pressure resulting from the deadweight of the compactor, which was employed in the modeling of the case studies, is estimated to be approximately in the range of 10 to 15 kilopascals kPa. This value is calculated by dividing the compactor's deadweight by its width. Since specific information regarding the compactors used was unavailable, a trial-and-error approach was adopted to obtain compaction results that closely matched those observed in the examined cases.

The approach employed to simulate the compaction effect, as elucidated by Ezzeldin and El Naggar in (2022), is rooted in the action compaction method. This method entails modeling each layer of backfill initially in a loose state and subsequently converting it to a dense state by changing the material properties in plaxis3D construction stage following the application of a compaction load, as illustrated in Figure 3.3. This simulation process is instrumental in accommodating the alterations in soil properties that transpire during construction, especially concerning the consolidation of soil layers. The modeling sequence procedure for simulating the compaction effect on soil adheres to a systematic, stepwise approach. In the initial step, a loose layer of soil with a depth of 0.3 m is placed as side fill, representing the initial state of the soil. Subsequently, in the ensuing phase, a uniformly distributed load is imposed on top of the loose soil to replicate the compaction impact on the soil. Once this uniform load has been applied, the third phase of the modeling sequence procedure is initiated. During this stage, the uniform load is deactivated, and the soil model transitions from a loose to a dense state. A new soil layer is introduced in a loose state, and the compaction process is iterated. This sequence continues until a backfill height of 2.4 m is attained.

To address the challenges posed by a backfill height of roughly beyond 2.4 to 2.7 m, a vertical load was placed on top of the culvert's crown. At this juncture, a line load is activated along the length of the culvert to account for the crown deformation triggered by lateral soil stress. This load was strategically employed to mitigate the occurrence of peaking deformation rates.

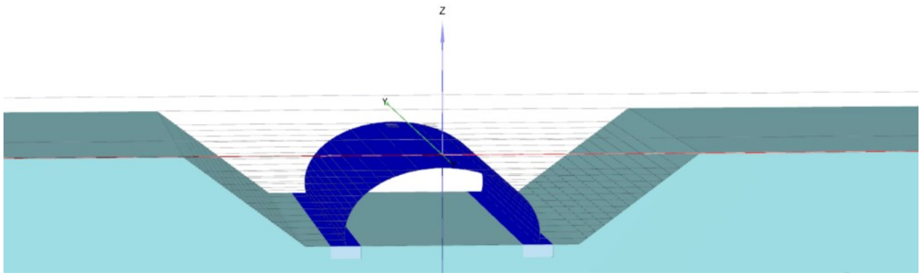

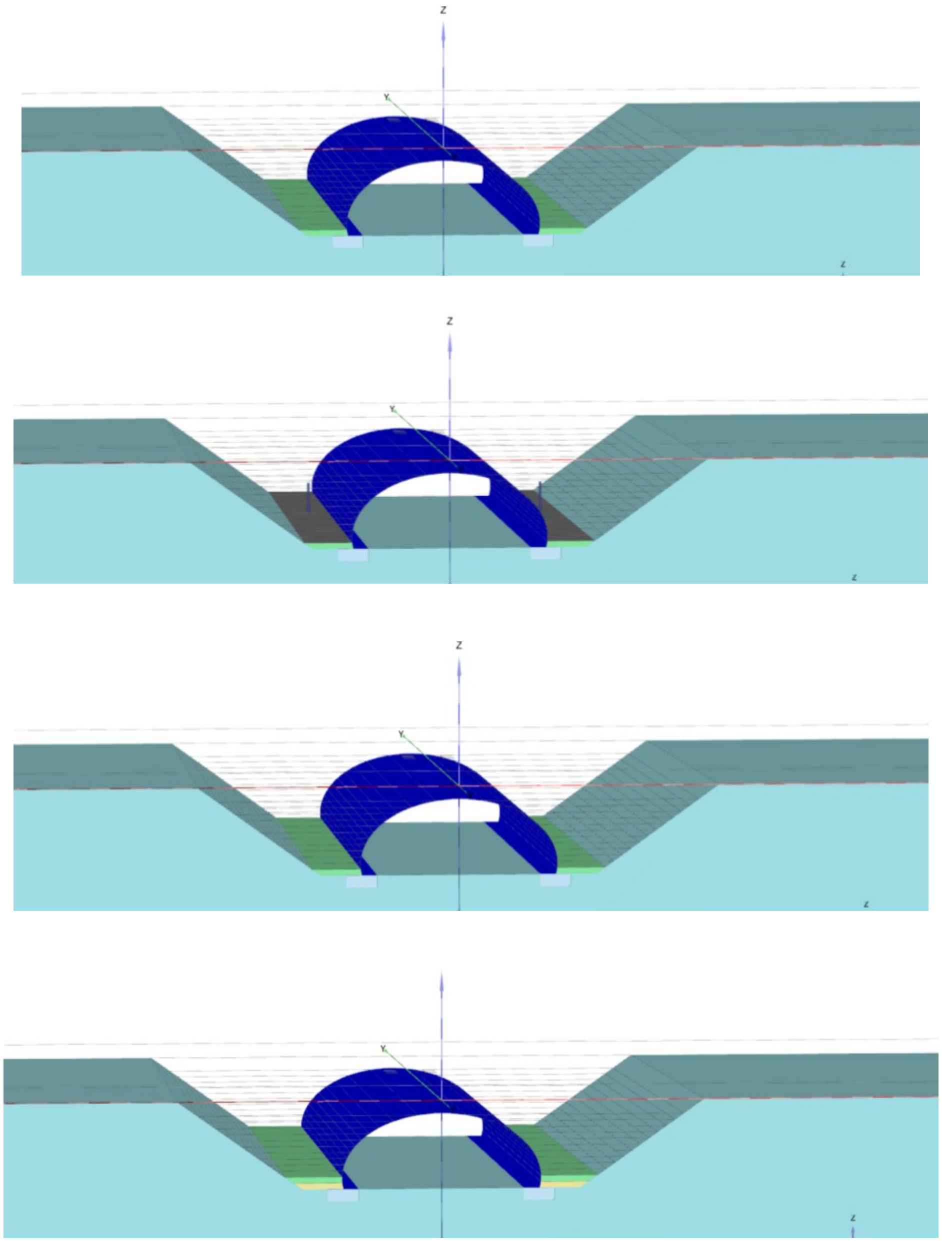

Figure 3.3 Backfill layers compaction sequence.

3.4 Corrugated Steel Plates Modeling

The metal culvert was simulated using plate element, which are essentially shell components and are meant to represent thin, two-dimensional earth constructions with high flexural rigidity. The 6-node triangular plate elements that make up plates have six degrees of freedom per node: three for translation ux, uy, and uz and three for rotation ϕ x, ϕ y, and ϕ z. The Mindlin plate theory is the foundation for the plate elements Bathe, 1982. This hypothesis takes both plate bending and shearing into account. In addition, when an axial force is applied the element can change length. A cross section of the SMB and its main dimensions are shown in Figure 3.1 It is a low profile 5-gauge 5.5-mm corrugated steel plate arch with a 9.5-m span and 3.7-m rise. The structure's foundation is made of concrete. The plate material was characterized using the elastic modulus E of 200 GPa and the Poisson's ratio n of 0.3. The concrete footings were modeled as elastic, with elastic modulus 30 GPa and Poisson’s ratio 0.3. A conventional method of modelling the corrugated plate of the pipe as an "equivalent" plain plate with orthotropic material properties was used. Figure 3.4 Shows the corrugation profile. The flexural rigidity EI and axial stiffness EA of the culvert determine its structural response. The elastic modulus, moment of inertia, and cross-sectional area of the plate are denoted as E, I, and A, respectively. A corrugated plate has distinct values for axial and flexural rigidity in directions perpendicular to the corrugations and parallel to them, respectively. These directions reflect the longitudinal and circumferential directions of the culvert. Geometric features that depend on direction cause anisotropy. The corrugated plate yields the same rectangular cross-section in both directions when converted to a "equivalent" plain plate. The steel plate used in this study had a thickness of 5.5 mm, a wavelength of 150 mm, and a wave height of 55 mm from crest to crest.

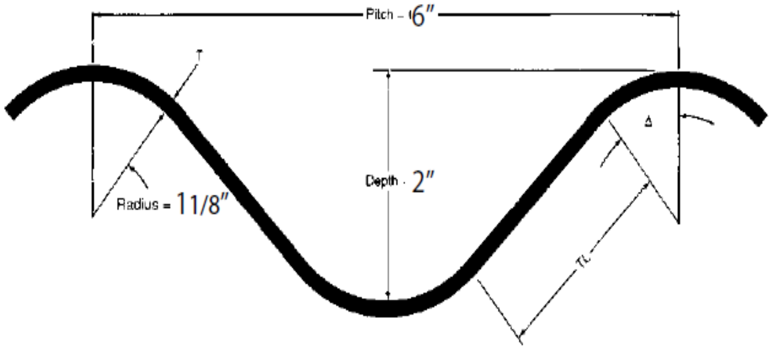

Figure 3.4 5-gauge 5.5-mm corrugated steel profile (Corrugated Steel Pipe Institution, 2007).

The second moment of inertia was to be 0.1269 in^4/in. The area of the original plate was found to be 3.199 in^2/ft. The plate was then modeled as an orthotropic plate in Plaxis3D, with an equivalent thickness d of 61.8 mm based on the second moment of area calculated as for a rectangular cross-section. To calculate the modulus of elasticity in the stiff direction $\bar{E}_\theta$, modulus of elasticity in the weak direction $\bar{E}_L$, unit weight of the plate $\bar{\gamma}$, Circumferential Out-of-plane Shear modulus $\bar{G}_{\theta R}$, circumferential Out-of-plane Shear modulus $\bar{G}_{LR}$, and In-plane Shear modulus $\bar{G}_{\theta L}$, were computed using the equation presented by Aagah & Aryannejad (2014). Table 3.2 provides a summary of these properties.

$$\bar{t} = \sqrt{\frac{12\,I}{A}} \tag{42}$$

$$\bar{\gamma} = \frac{\gamma A}{\bar{A}} \tag{43}$$

$$\bar{E}_\theta = \frac{EI_\theta}{I} \tag{44}$$

$$\bar{E}_L = \frac{EI_l}{\bar{I}} \tag{45}$$

$$\bar{v} = 0 \tag{46}$$

$$\bar{G}_{\theta R} = \frac{\bar{E}_{\theta}}{2(1+v)} \tag{47}$$

$$\bar{G}_{LR} = \frac{\bar{E}_{L}}{2(1+v)} \tag{48}$$

$$\bar{G}_{\theta L} = \frac{\sqrt{\bar{E}_{L}+\bar{E}_{\theta}}}{2(1+v)} \tag{49}$$

Table 3.2 Equivalent plate material properties.

Parameter	Original Plate	Equivalent Plate
Plate thickness	0.218 in	61.8 mm
Unit weight	-	8.75 $\mathrm{kn/m^2}$
Cross- sectional area	3.199 in^2/ft	-
Moment of inertia	0.1269 in^4/in	-
Poisson's ratio	0.3	-
Circumferential elastic modulus	-	150,000 $\mathrm{kn/m^2}$
Longitudinal Elastic modulus	-	22,300 $\mathrm{kn/m^2}$
Circumferential Out-of-plane Shear modulus	-	11,150 $\mathrm{kn/m^2}$
Longitudinal Out-of-plane Shear modulus	-	75,000 $\mathrm{kn/m^2}$
In-plane Shear modulus	-	2436 $\mathrm{kn/m^2}$

3.5 Model Validation

In this research study, the accuracy of the finite element model underwent a rigorous validation process by directly comparing them with the outcomes generated by the experimental results. This numerical model was designed to replicate the behavior of corrugated metal culverts when subjected to identical load conditions as those applied in the physical experiments. The primary focus of this comparative analysis centered on two critical aspects: crown deformation and thrust forces. When scrutinizing the graphical representations of crown deformation Figure 3.5, an alignment became evident between the findings of the current study and those of a previous investigation conducted by Webb (1999). This correspondence between the results from the present research and the prior work by Webb (1999) serves as a compelling argument in support of the suitability and precision of the numerical model utilized in the current study.

The deformation patterns and displacement magnitudes observed at various locations on the culvert's crown, as compared to Webb's earlier work. Both the Plaxis3D model and field measurements exhibit a depth-dependent trend in thrust forces Figure 3.6. As the depth increases, the thrust forces rise, indicating an increasing lateral pressure exerted on the culvert walls. When comparing the general shape of the thrust force profiles, there is a resemblance between the Plaxis3D model and field measurements. Both show a gradual increase in thrust forces with depth, followed by a steeper increase in the deeper layers. In other words, the depth-dependent behavior is consistent between the two cases.

Plaxis3D model consistently predicts lower thrust forces compared to the field measurements. This difference becomes more pronounced with increasing depth. For instance, at a depth of 4.5 m, Plaxis3D model predicts a thrust force of approximately -115.88 kN, while the field measurement reports a slightly higher thrust force of -120 kN. This suggests that the model tends to underestimate the lateral pressure on the culvert walls. As for the shallower layers up to approximately 1.5 m, the Plaxis3D model and field measurements show reasonably good agreement. However, as the depth increases beyond 1.5 m, the model begins to deviate significantly from the field data, consistently producing lower thrust force values.

In the validation of crown deformation, both the field measurements and the Plaxis3D model exhibit an expected pattern where deformation tends to increase as the depth below the surface increases. However, when we closely examine the validation results, disparities in the magnitude of deformation become evident between the field measurements and the Plaxis3D model. In most instances, the model tends to slightly underestimate the amount of deformation when compared to the actual field measurements. For instance, at a depth of 2.4 m, the field measurement records a deformation of 51 mm, while the model predicts a slightly lower value of 49.65 mm. At a depth of 2.7 m, both the field measurements and the model measurements exhibit a reduction in deformation. The field measurements decrease from 63 mm to 48 mm, while the model's deformation values decrease from 62.63 mm to 47.68 mm. This discrepancy may be attributed to the localized influence of concrete blocks in the field scenario, which is not completely replicated in the model. The model attempts to emulate this influence using a line load, but it may not fully capture the intricacies of the actual field conditions. Moving deeper to a depth of 3.9 m, both the field measurement 78 mm and the model prediction 79.14 mm are remarkably similar in value. This suggests that the model performs relatively well at this particular depth. In both cases, the deformation tends to decrease due to the weight of the soil above the crown, with slightly larger values observed in the numerical model compared to the field measurements.

The Plaxis3D model provides a reasonable approximation of the field measurements, especially at greater depths e.g., 3.9 m. However, differences in magnitude persist, and the model's ability to capture localized effects, such as the presence of concrete blocks, remains a challenge. To improve the model's accuracy, it may be necessary to refine the modeling assumptions and parameters, taking into account specific site conditions, material properties, and the exact nature of the concrete block's influence on deformation. Additionally, field measurements and model predictions can be compared at more depths to gain a comprehensive understanding of the model's performance. In essence, this model validation process serves as a cornerstone in ensuring the accuracy and dependability of simulations in studying the behavior of culverts. It not only reaffirms the robustness of the employed numerical model but also paves the way for comprehensive and insightful investigations into the dynamic response of corrugated metal culverts, further enhancing our understanding of their performance in real-world scenarios.

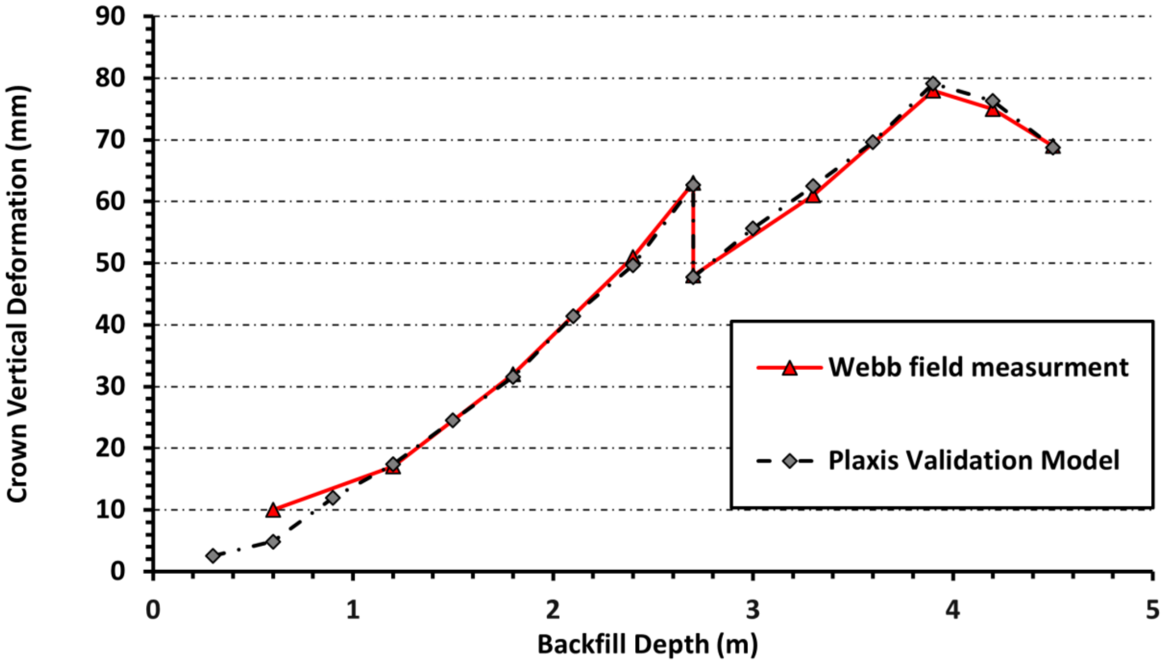

Figure 3.5 Deformation-compaction curves of Webb field results and the developed plaxis3D model.

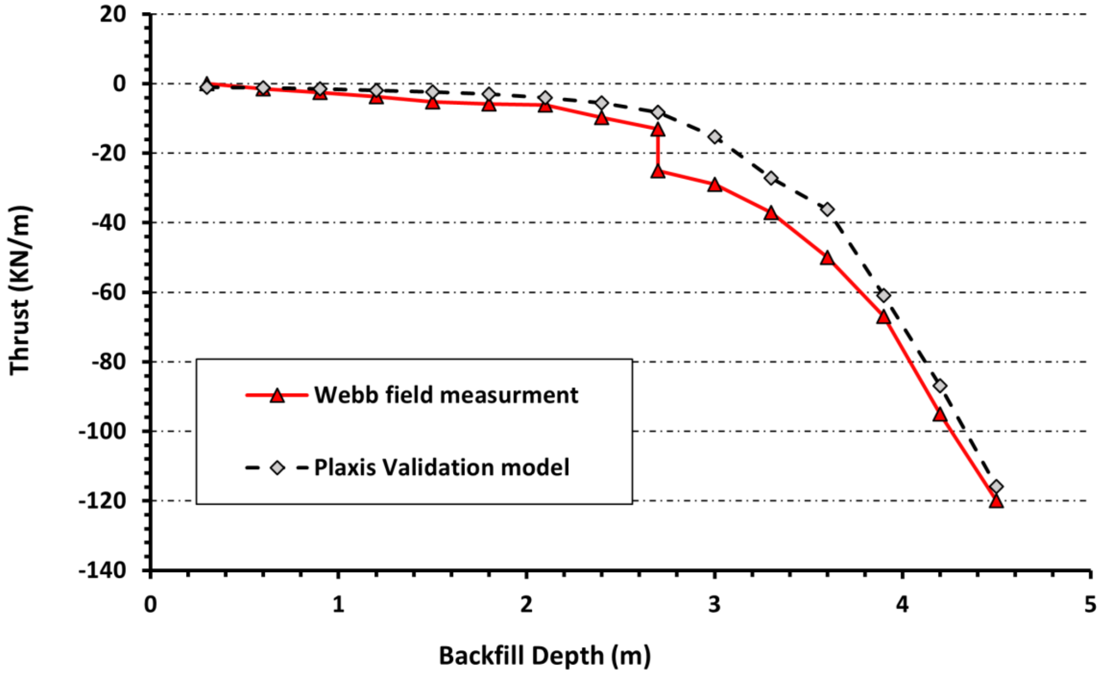

Figure 3.6 Hoop compression curves of Mark C. Webb field results and the developed plaxis3D model.

3.6 Soil Cover Impact on Dynamic Train Loads Parametric Study

A considerable research gap exists in the current body of literature concerning the behavior of soil metal bridges SMBs when exposed to high-speed trains, particularly those traveling at speeds of up to 300 km/h. While previous studies have shed light on various aspects of SMB performance, such as the influence of dynamic loading from passing trucks and the relationship between soil cover depth and bridge deflection, these investigations have primarily focused on scenarios involving road traffic and relatively lower speeds. For instance, Yeau et al.'s research in 2009 provided valuable insights into the behavior of SMBs when subjected to dynamic loading from passing trucks. Their findings indicated that SMB deflection exhibited a non-linear decrease as the depth of soil cover increased. Similarly, Beben's work in 2012 explored dynamic amplification factors DAFs resulting from passing trucks, demonstrating that during dynamic loading conditions, SMBs experienced higher levels of displacements and strains compared to static loading. Beben's (2014) field tests on a corrugated steel plate CSP railway culvert further contributed to our understanding of SMB behavior, highlighting significant deformations at specific locations on the culvert, notably at the crown and quarter points. Additionally, Flener's research in 2004 emphasized the relationship between soil cover depth and bending moments due to soil load, providing valuable insights into the structural response of SMBs. However, the critical research gap pertains to the lack of comprehensive studies addressing how SMBs perform when subjected to the high-speed forces generated by trains traveling at speeds exceeding 300 km/h. This is a crucial area of investigation, especially as transportation infrastructure continues to evolve.

In contrast to the conventional approach recommended by the 2003 Eurocode "Action on Structures," which relies on a simplified factor-based method where static loads are adjusted using factors based on a structure's shape and length to estimate dynamic effects, this research employs a distinct and more advanced methodology. Specifically, the study takes advantage of Plaxis3D dynamic analysis to model dynamic loads in a more comprehensive manner. The focal point of this analysis is the CRH 380A, a high-speed train with a remarkable axle load of 150 tons and the remarkable capability to attain speeds of up to 300 km/h. The CRH 380A is characterized by specific dimensions, with the locomotive measuring 26.5 m in length and the coach measuring 25 m. The train's wheels possess a diameter of 0.86 m and are spaced with a wheelbase of 2.5 m. Additionally, critical parameters such as the center distance between bogies within the same car, measured at 17.5 m, and the center distance between bogies in adjacent cars, measured at 7.5 m, have been meticulously determined. For visual reference and clarity, the profile of the CRH 380A train is thoughtfully presented in Figure 3.7, allowing for a more comprehensive understanding of its dimensions and layout within the context of the dynamic analysis. This methodological departure from the Eurocode's factor-based approach underscores the study's commitment to precision and accuracy in assessing the intricate dynamics imposed by high-speed trains on structures, yielding valuable insights into the structural response under these demanding conditions.

Figure 3.7 CRH 380A profile.

3.6.1.1 Geometry, Mesh and Boundary Conditions

A comprehensive three-dimensional model has been developed and visually represented in a schematic Figure 3.8. The new model shares similarities with its predecessor but incorporates several additional elements to elevate its realism and precision. Notably, the newly introduced components encompass the railway track, which comprises sleepers and rails. Sleepers have been modeled using volumetric elements, while the rails are represented by plaxis3d beam elements.

The study involved the creation of a total of 15 distinct models, each varying in terms of the depth of soil cover, specifically set at 2, 3, and 4 m. These models shared consistent dimensions, with each one measuring 120 m in length, 30 m in width, and 30 m in height. To generate the mesh for each model, a "very fine" global coarseness value was employed, with particular attention given to refining the metal plates' mesh to better capture deformation. This refinement corresponded to relative element size factors of 0.7 in the outer regions of the model and 0.5 near the Corrugated

Metal Plate CMP. Notably, all meshes were automatically generated to ensure consistency and efficiency in the analysis process. In terms of boundary conditions, the study-maintained default settings throughout the analysis. These default conditions encompassed a free upper surface, signifying the absence of constraints applied to the model's top. The sides were typically set to be normally fixed, restricting lateral or horizontal movements, while the bottom was fully fixed, disallowing any vertical movement. Furthermore, the interface between the soil and the Corrugated Metal Plate (CMP) was meticulously modeled using interface elements. Interface elements are a specialized type of finite element used to capture the behavior of contact surfaces between materials with differing properties. In the context of this study, the corrugations of the metal plate were represented by utilizing an equivalent plain plate with orthotropic material properties, a pragmatic approach that effectively captures the structural intricacies without directly modeling the corrugations themselves.

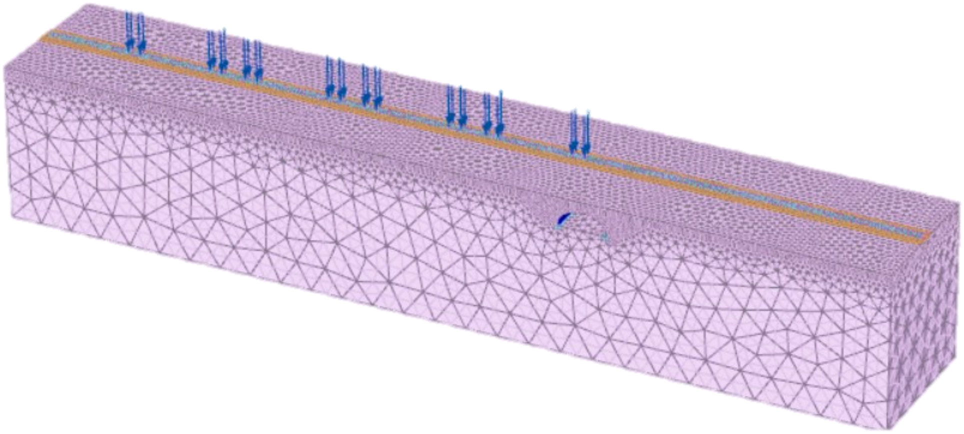

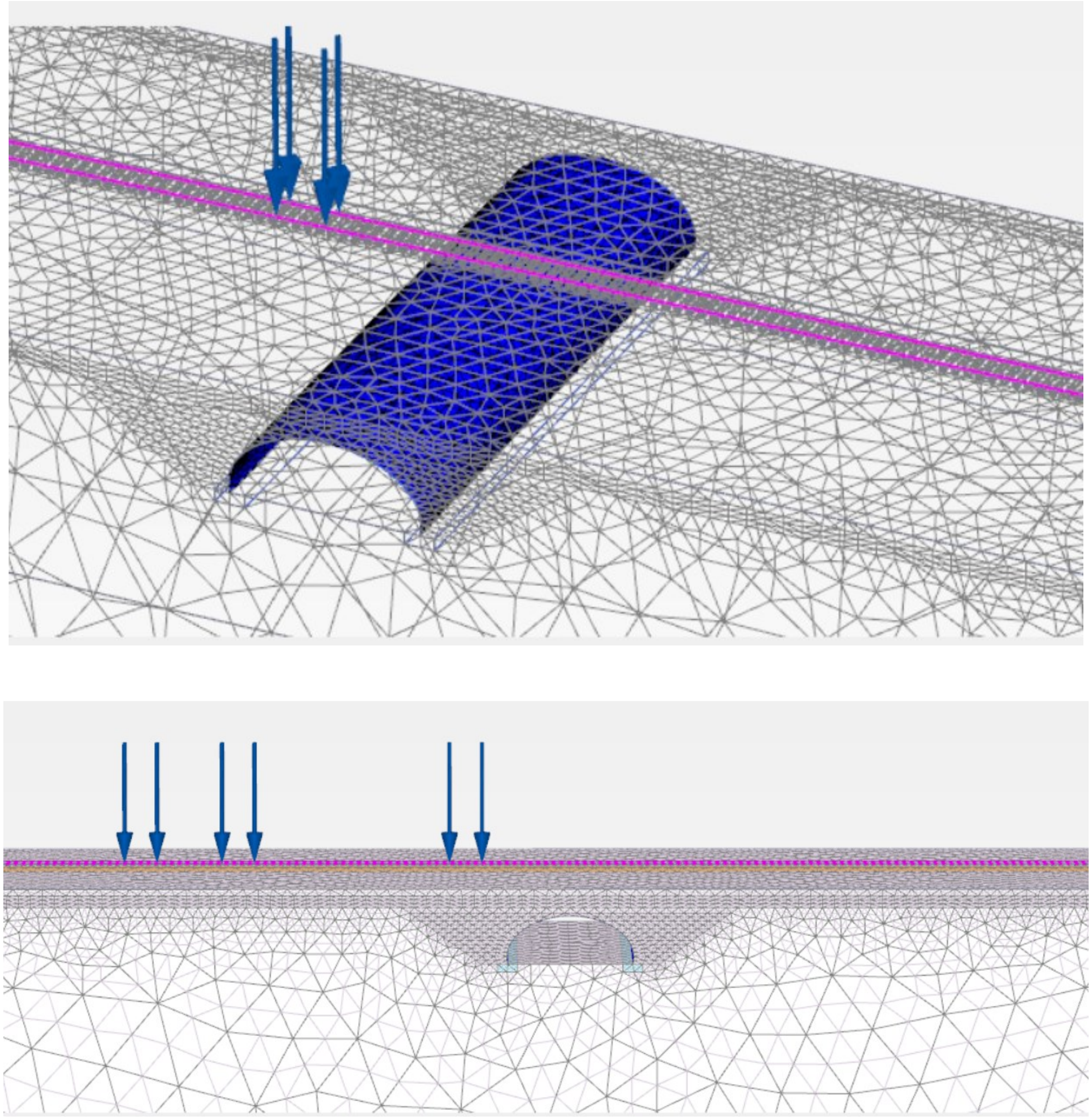

Figure 3.8 Three-dimensional structural representation of plaxis3D model.

3.6.2 Soil And Material Properties

A series of deliberate modifications were executed on the soil parameters. These modifications were undertaken with the specific objective of augmenting the overall tensile strength and rigidity of both the backfill material and the overlying layers. The purpose of these alterations was to enhance the soil's load-bearing capacity, particularly in response to the substantial dynamic loads imposed by passing trains.

Moreover, an additional layer of ballast material was introduced as part of our intervention. This supplementary layer was positioned to function as a load-distribution mechanism, effectively dissipating the substantial loads emanating from the railway track. This placement ensured the uniform distribution of the loads imposed by the trains across the underlying soil matrix, thereby mitigating the risk associated with localized stress concentrations and potential structural integrity issues. A comprehensive delineation of the specific soil properties and parameters that constituted the focal points of our investigation is presented in Table 3.3

Table 3.3 Soil Material Properties.

Properties	Ballast	Foundation soil	Dense	Unit
Soil Model	Hs	HSs	HSs	-
Drainage Type	Drained	Drained	Drained	-
γ_{unsat}	21	22	22	kN/m^3
γ_{sat}	21	22	22	kN/m^3
E_{50}^{ref}	225.0e3	60e3	60e3	kN/m^2
E_{oed}^{ref}	186.9e3	60e3	60e3	kN/m^2
E_{ur}^{ref}	450.0e3	180e3	180e3	kN/m^2
v_{ur}	0.2	0.2	0.2	-
G_o^{ref}	-	121.2e3	121.2e3	kN/m^2
$\gamma_{0.7}$	-	0.11e-3	0.11e-3	-

m	0.5	-	-	-
c'_{ref}	10	0	0	kN/m^2
$\varphi\ phi$	45	40	40	°
ψ psi	5	10	10	°

The rail was modeled with a beam element to simulate its behavior along a 160 m profile in the x-direction. The rectangular cross-section of the beam element was chosen to match the properties of a standard rail UIC 60, as presented in Table 3.4 To ensure a stable and secure connection between the rail and the sleepers, each sleeper was connected to the rail with two rail clips with a thickness of 30 cm. The standard sleeper was modeled as a volume element, and its properties were assigned to accurately simulate its behavior in the model. A total of 266 sleepers were placed in the model with a center-to-center distance of 60 cm to represent a realistic railway track system. Figure 3.9 provides a visual representation of the model, showing the placement of the sleepers and their connections to the rail.

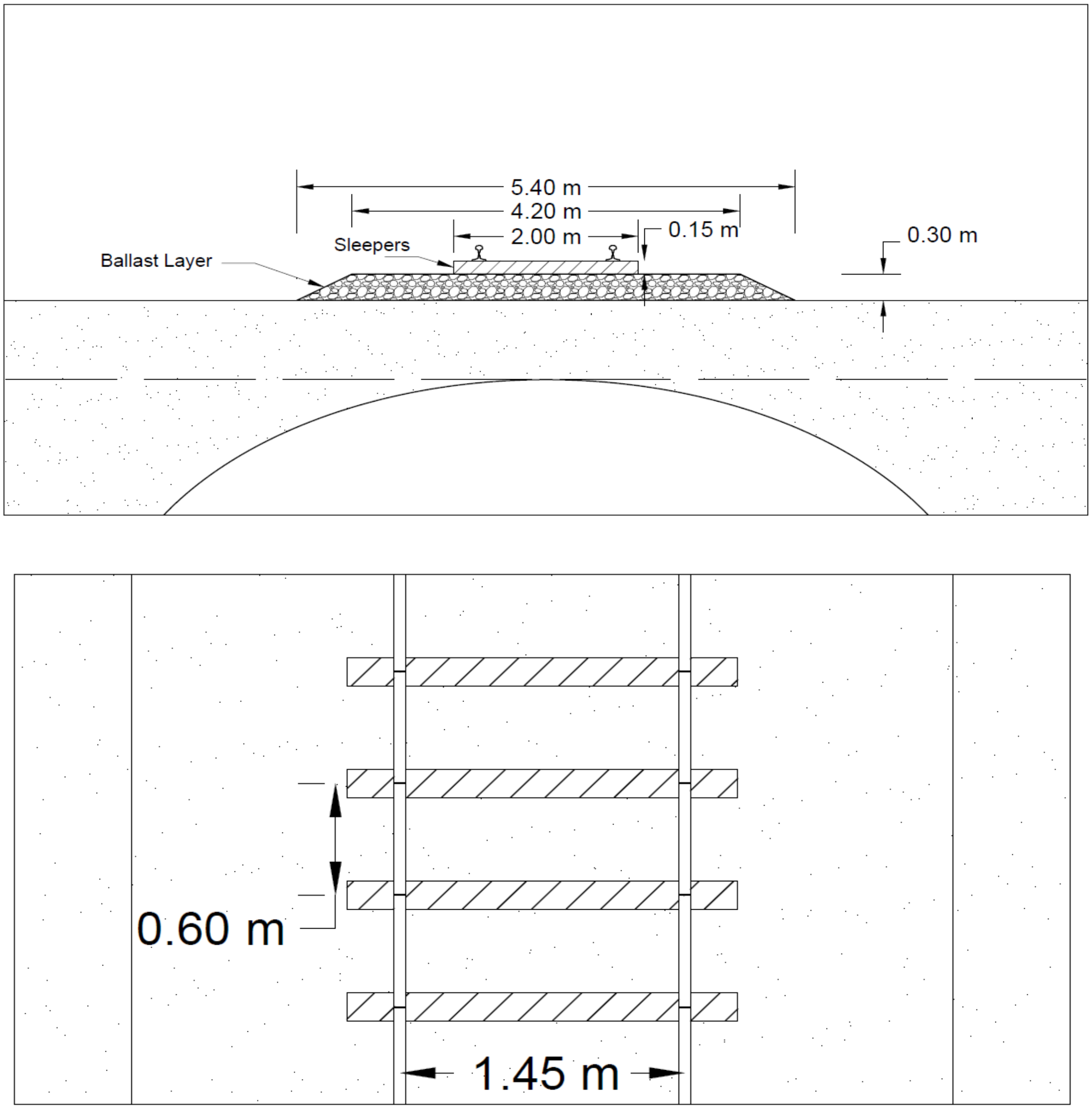

Figure 3.9 Visual representation of the rail track.

Table 3.4 Properties of a UIC 60 rail.

Parameter	Rail	Unit
Cross Section Area	7.7e-3	m^2
Unit weight $\boldsymbol{\gamma}$	78	KN/m^3

Young’s Modulus E	200e6	KN/m^3
Moment of inertia around the second axis I_2	3.055e-6	m^4
Moment of inertia around the third axis I_3	5.13e-6	m^4

3.7 Parametric Study Results

3.7.1 Crown Deformation

The study employed advanced numerical modeling techniques to simulate the behavior of soil-metal bridges under varying conditions of soil cover depth and train speed. The numerical model accurately represents the physical properties of the bridge and the surrounding soil, allowing for a detailed analysis of deformations. Data collection involved assessing deformations at different soil cover depths 2 m, 3 m, and 4 m and various train speeds 100 km/h and 300 km/h. The analysis focused on the impact of these variables on bridge stability. The compelling relationship between soil cover depth and bridge maximum crown deformations is shown in Figure 3.10. Meanwhile, Figure 3.11 provides a detailed visual representation of the cross-sectional profile showcasing the maximum deformations experienced by the metal bridge. This illustration pertains to a scenario in which a train is traveling at a high speed of 300 km/h, and it explores the variations in deformations across three distinct soil cover depths: 2 m, 3 m, and 4 m. Figures 13 and 14 present a three-dimensional representation capturing the deformations that occur as a high-speed train, traveling at 300 km/h over the metal bridge. These visual representations offer a valuable opportunity to delve deeper into the dynamic response of the bridge to the train's motion. Within these illustrations, we can distinctly observe the deformation process unfolding in perfect harmony with the direction of the train's travel. In both scenarios, whether it's the 2 m or 4 m soil cover depth, the bridge's response aligns seamlessly with the left-to-right motion of the train. A particularly noteworthy observation pertains to the discrepancy in deformation between the two cases. In the instance of the shallower 2 m soil cover depth, the deformation appears significantly more pronounced. This disparity serves as a clear indicator of the deeper soil's remarkable capacity to absorb and distribute the stress generated by the moving loads.

Considering the effect of traveling train speed on bridge deformation, a consistent trend emerges. As the train speed increases, the bridge deformation also increases across all three soil cover depths. This is evident in the data where the deformations consistently rise with higher speeds, irrespective of the depth. For instance, at a depth of 2 m, deformations range from approximately -1.01 mm at 100 km/h to -1.85 mm at 300 km/h, indicating an 83 % increase in deformation over this speed range. Similarly, at 3 m depth, deformations vary from approximately -0.63 mm at 100 km/h to -0.99 mm at 300 km/h, with a change percentage of 57 %. Lastly, at a 4 m depth, deformations span from approximately -0.42 mm at 100 km/h to -0.68 mm at 300 km/h, resulting in a 62 % change.

Turning to the influence of soil cover depth, a distinct pattern emerges. Deeper soil cover depths consistently exhibit reduced bridge deformations at all train speeds. This reduction is apparent as we observe deformations decreasing as the depth increases, irrespective of the traveling speed. For instance, at a depth of 2 m, deformations increase with speed, but at 3 m depth, deformations decrease, and at 4 m depth, they decrease even further. This emphasizes the role of deeper soil cover in mitigating bridge deformations, with the reduction being more pronounced as the depth increases.

The reduction in bridge deformations is non-linear with respect to soil cover depth. While deeper depths are associated with reduced deformations, the rate of reduction diminishes as the depth increases. This is indicated by the change percentages, which decrease as we move from 2 m to 4 m depth. This non-linear behavior suggests that there may be an optimal depth at which further increases in depth provide diminishing returns in terms of deformation reduction.

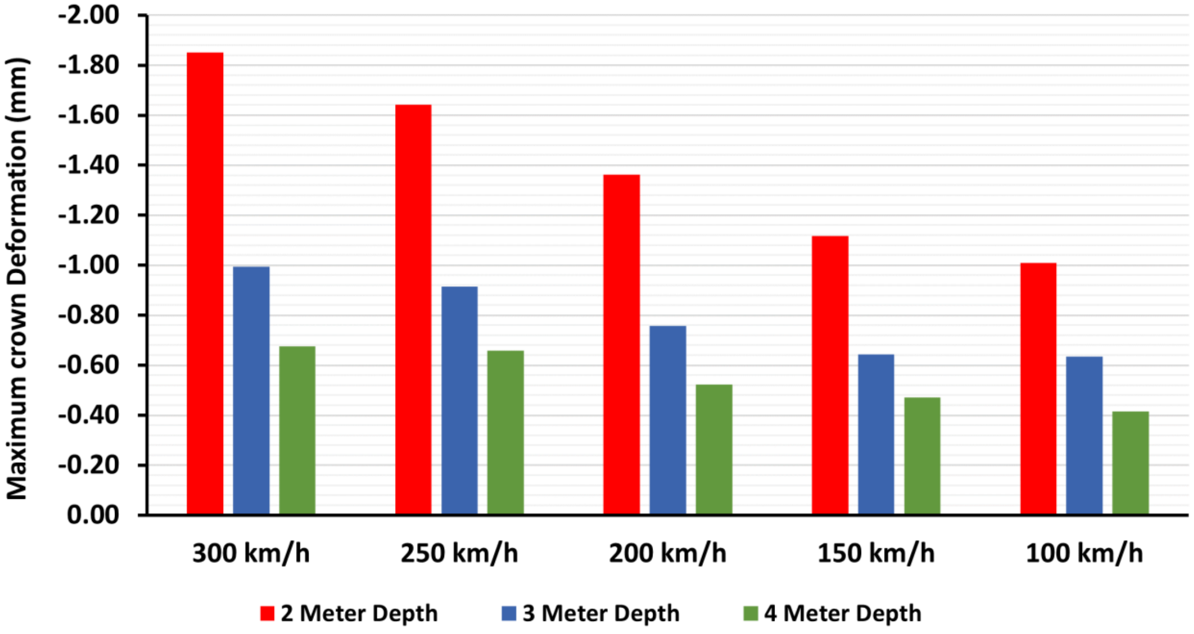

Figure 3.10 Soil cover depth impact on the maximum crown deformation for various train traveling speeds.

When the high-speed train travels across the soil-metal bridge, deformations occur in both the X-direction and the Y-direction. The provided Figure 3.11 illustrates the original cross-sectional coordinates that represent the initial profile of the bridge, while the newly deformed coordinates are the alterations caused by the high-speed train's passage. The deformation is not uniform and displays an asymmetry, which is characteristic of the bridge's response to the train's lateral forces. To gain a deeper understanding of this behavior, we turn our attention to Figure 3.11 as a visual representation of the original cross-sectional coordinates, effectively portraying the bridge's initial profile before the high-speed train's passage. In contrast, the newly deformed coordinates depict the changes that ensue due to the train's rapid transit. What becomes apparent upon closer examination is that these deformations do not conform to a uniform pattern; rather, they exhibit a distinctive asymmetry. This lack of uniformity is a defining characteristic of how the bridge reacts to the lateral forces imparted upon it by the high-speed train. Expanding on these observations, it becomes evident that both the X and Z direction deformations prominently feature this asymmetry, with their behavior primarily dictated by the direction in which the train is traveling. A visual representation, in the form of a graph, underscores the considerable influence of directionality on these deformations. As the train advances from left to right, moving along the positive X-direction, the bridge undergoes substantial alterations in shape. This transformation can be attributed to the lateral forces generated by the high-speed train. These forces, acting perpendicular to the train's forward motion. However, they also induce substantial structural responses within the bridge, most notably materializing as the pronounced asymmetric deformations observed, particularly in the Z-direction.

Figures 3.12 and 3.13 provide a three-dimensional visualization of the deformation cycles for two contrasting scenarios: one with a train speed of 300 km/h over a 2 m soil cover depth and the other with the same speed over a 4 m depth. These figures offer insights into the deformation patterns exhibited by the arch metal bridge under these extreme conditions. Notably, the visual representation highlights that the 2 m depth case demonstrates more pronounced deformations. In both figures, it is evident that the deformations extend over a broader area of the arch metal bridge, encompassing both the x and y directions. This observation underscores the significance of the 2 m depth scenario, where the deformations are not only more substantial but also influence a larger portion of the bridge structure.

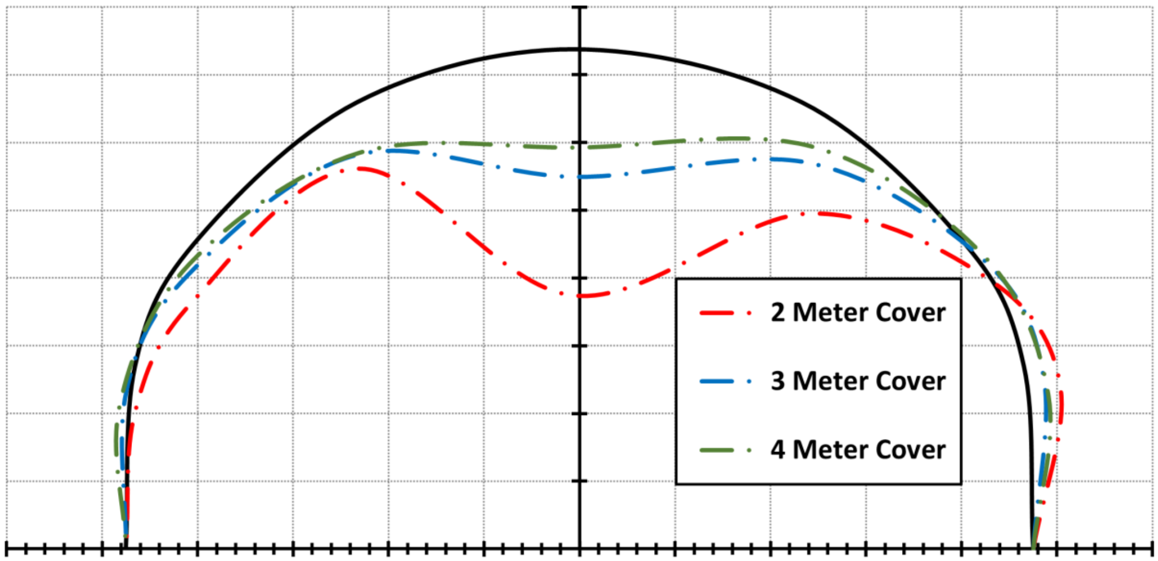

Figure 3.11 Cross-sectional deformation of the Soil-Metal Bridge SMB at a speed of 300 km/h for soil cover depths of 2, 3, and 4 m with a scale magnitude of 1000.

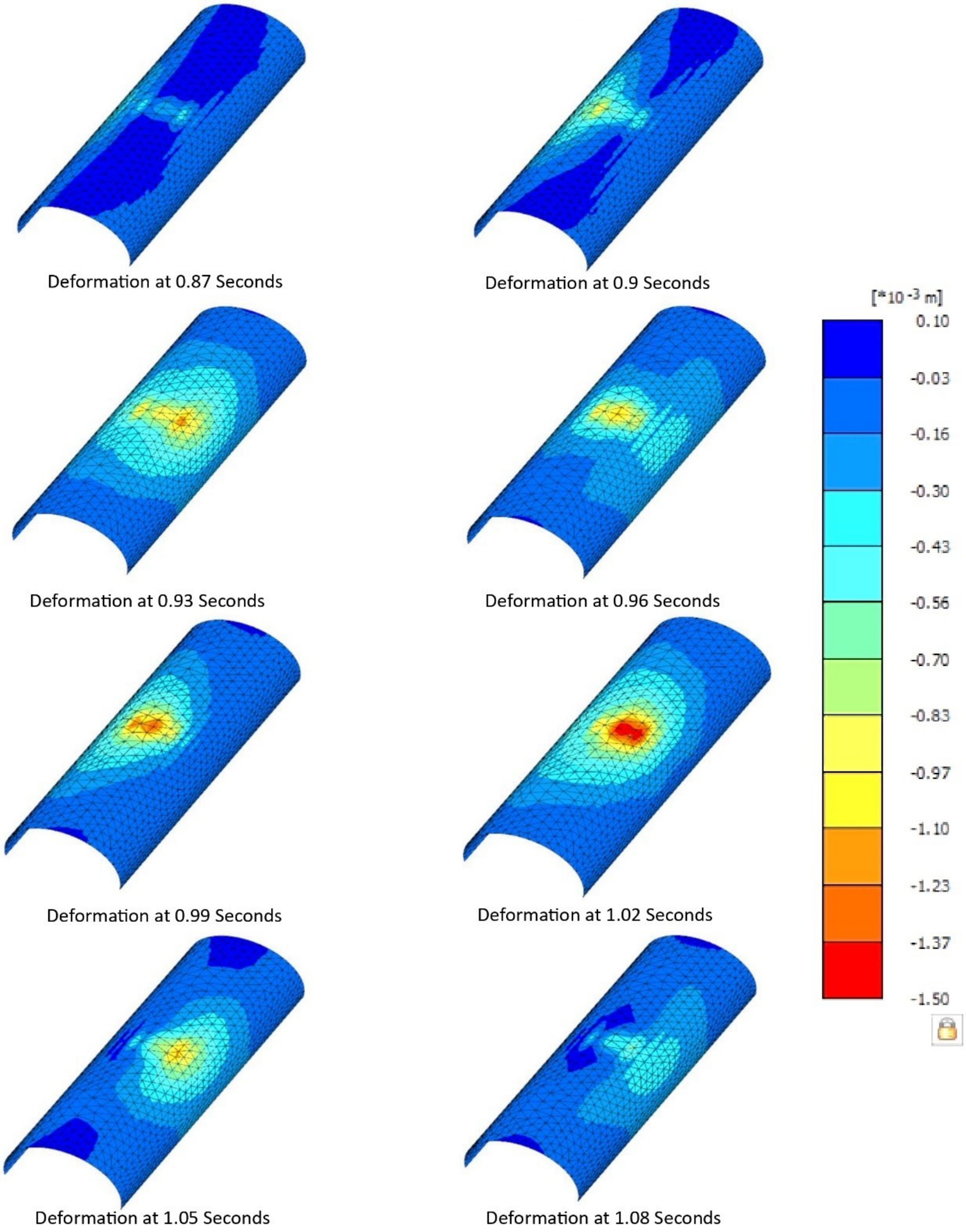

Deformation at 0.87 Seconds

Deformation at 0.9 Seconds

Deformation at 0.93 Seconds

Deformation at 0.96 Seconds

Deformation at 0.99 Seconds

Deformation at 1.02 Seconds

Deformation at 1.05 Seconds

Deformation at 1.08 Seconds

Figure 3.12 A three-dimensional representation capturing the SMB deformations cycle at different time intervals as a high-speed train travel at 300 km/h over 2 m cover depth.

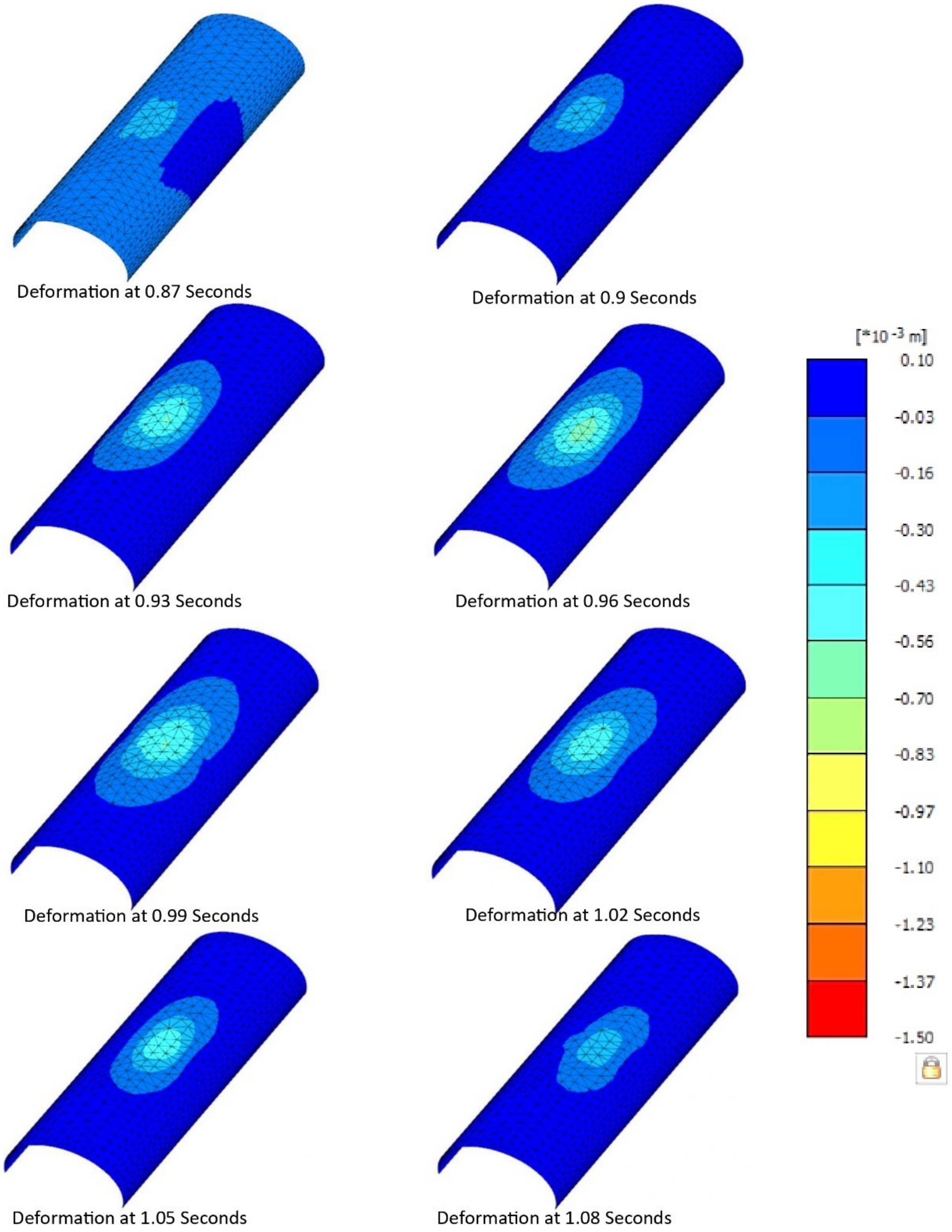

Deformation at 0.87 Seconds

Deformation at 0.9 Seconds

Deformation at 0.93 Seconds

Deformation at 0.96 Seconds

Deformation at 0.99 Seconds

Deformation at 1.02 Seconds

Deformation at 1.05 Seconds

Deformation at 1.08 Seconds

Figure 3.13 A three-dimensional representation capturing the SMB deformations cycle at different time intervals as a high-speed train travel at 300 km/h over 4 m cover depth.

The connection between the deformation of the bridge crown and the passage of a train across a soil-metal bridge is a dynamic process that unfolds progressively. This phenomenon is depicted in Figures 3.14 to 3.18, illustrating the evolution of crown deformations as trains travel at speeds of 100, 150, 200, 250, and 300 km/h across soil cover depths of 2, 3, and 4 m.

This deformation pattern is intricately linked to the relative position of the train's axis concerning the bridge's crown. The primary findings from the analysis can be summarized into five distinct states for illustrative purposes, the analysis focuses on the case of a train traveling at 300 km/h over a 2 m soil cover depth as outlined below:

- **Initial Stable State 0-0.06 seconds:** At the beginning of the simulation, the crown deformation remains relatively stable, with only minor fluctuations observed. This phase corresponds to the period before the locomotive's axis approaches the crown.
- **Crown Deformation Onset 0.06-0.15 seconds:** As the locomotive's axis gets closer to the crown, the crown deformation starts to become more pronounced. The deformation gradually increases in magnitude during this phase, reaching its maximum value when the first axis is directly above the crown.
- **Peak Crown Deformation 0.15-0.39 seconds:** The most significant crown deformation occurs when the first axis is atop the crown, peaking at approximately -1.68 m. This stage corresponds to the moment of maximum downward deformation of the crown due to the concentrated load.
- **Recovery and Oscillation 0.39-1.74 seconds:** Subsequently, as the first axis starts moving away from the crown location, the crown deformation gradually decreases. However, it does not return to its initial stable state. Instead, it exhibits a distinct oscillatory behavior as subsequent coach axes approach and leave the crown location. This oscillation is a

characteristic response of the bridge to the sequential loading and unloading caused by the moving train.

- **Final Steady State 1.74 seconds onward:** The crown deformation eventually stabilizes after the last coach of the train has passed. The bridge settles into a new equilibrium, but with a residual deformation compared to its initial state.

The higher the train speeds, the faster the coaches travel over the bridge. Consequently, the entire crown deformation cycle occurs more rapidly for higher-speed trains. This leads to shorter intervals between successive instances of maximum crown deformation.

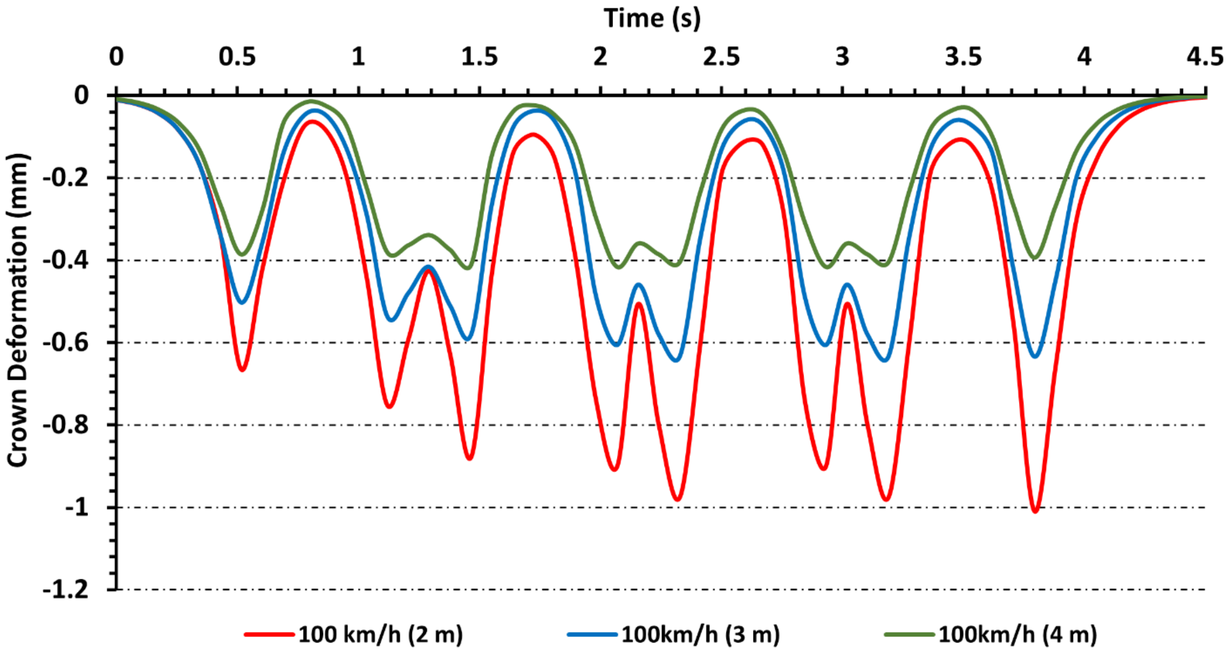

Figure 3.14 Deformation of the crown over time as a result of a 100 km/h train crossing over soil cover depths of 2, 3, and 4 m.

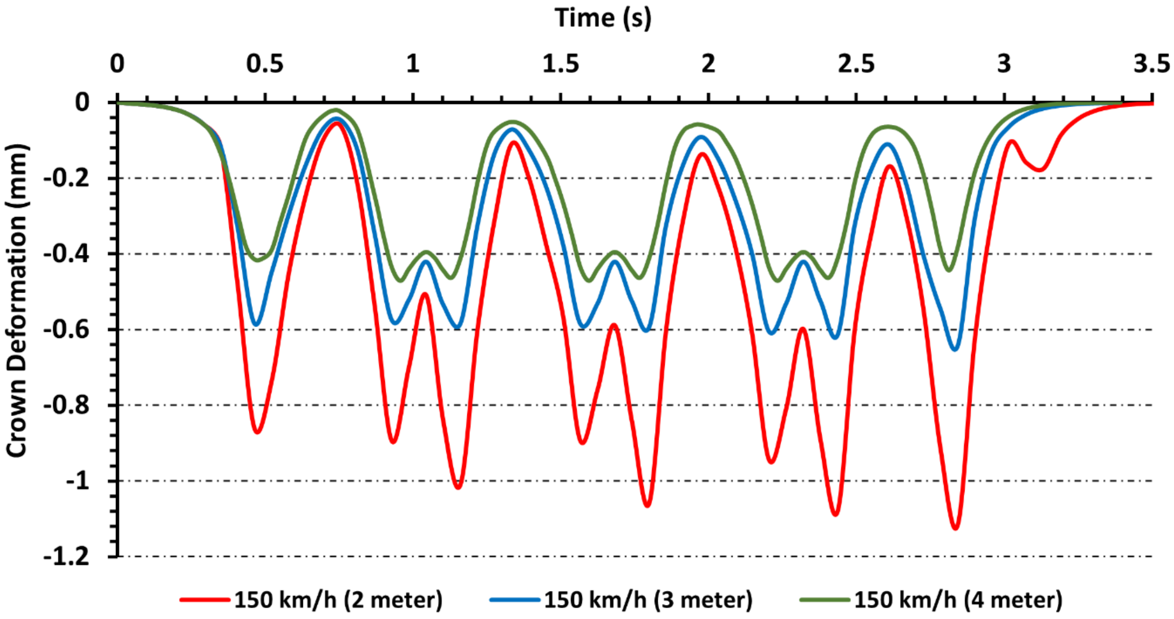

Figure 3.15 Deformation of the crown over time as a result of a 150 km/h train crossing over soil cover depths of 2, 3, and 4 m.

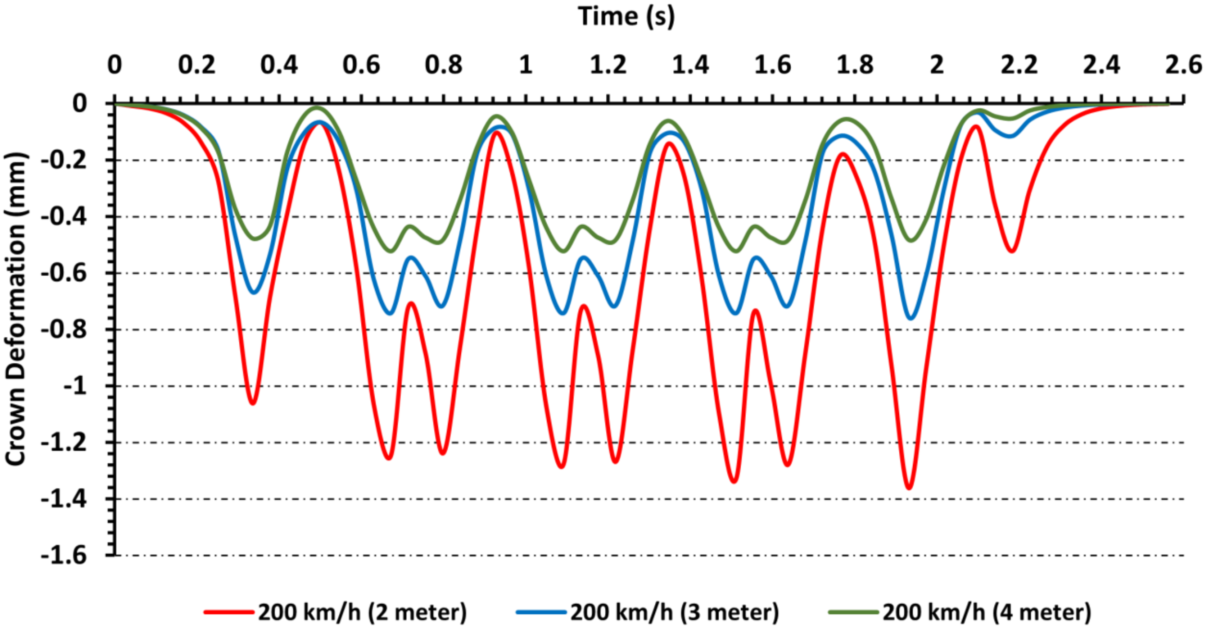

Figure 3.16 Deformation of the crown over time as a result of a 200 km/h train crossing over soil cover depths of 2, 3, and 4 m.

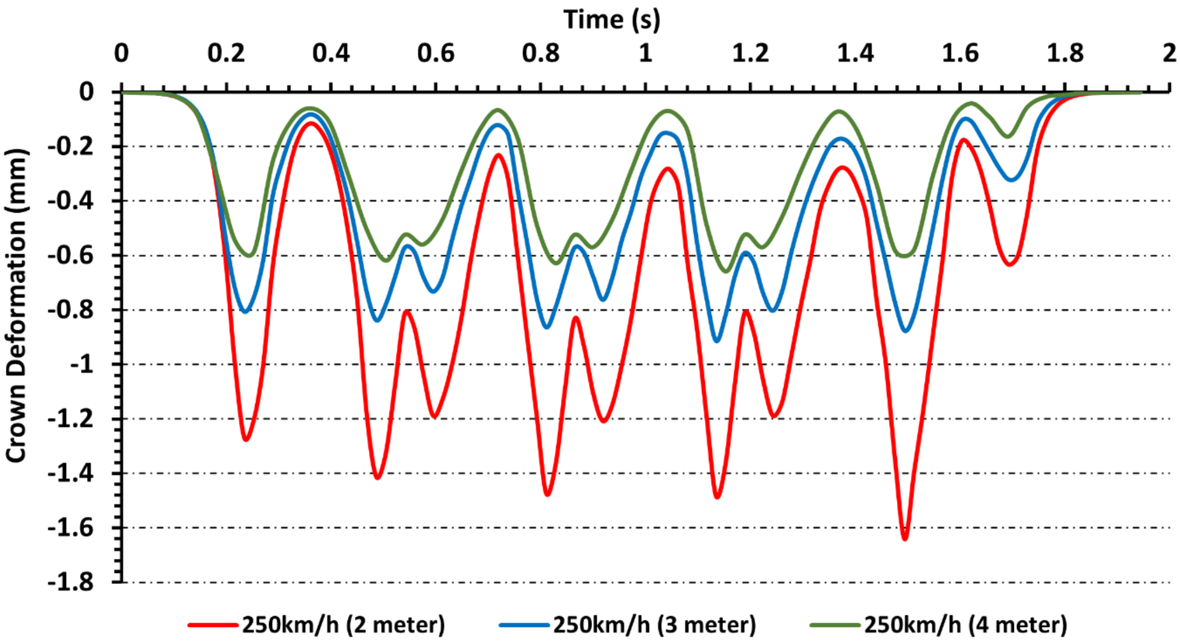

Figure 3.17 Deformation of the crown over time as a result of a 250 km/h train crossing over soil cover depths of 2, 3, and 4 m.

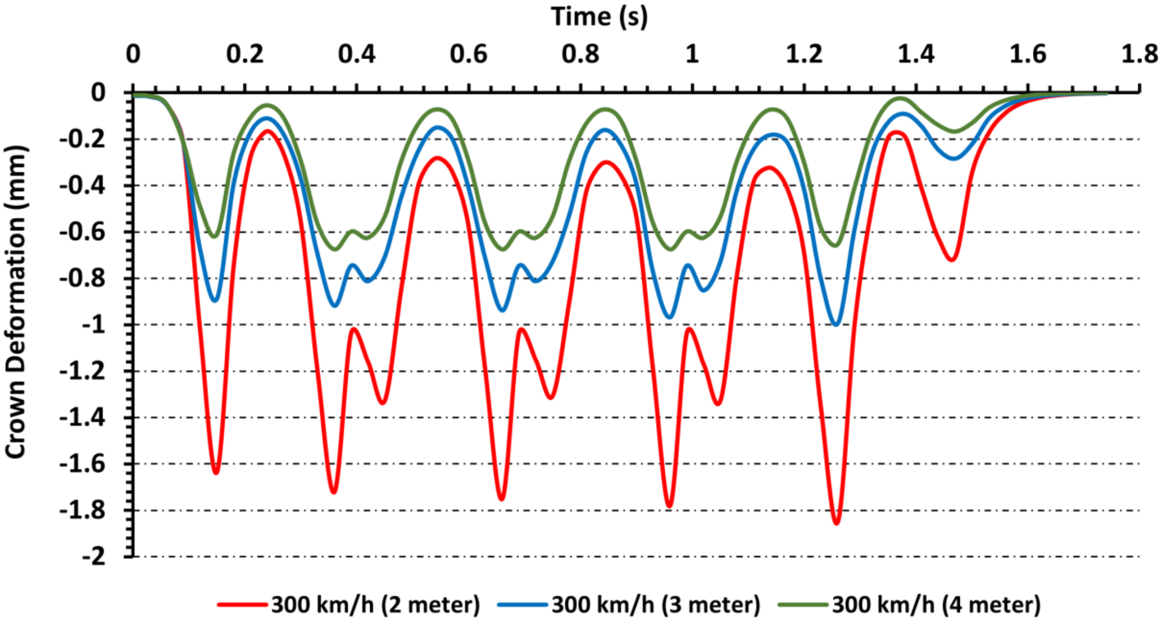

Figure 3.18 Deformation of the crown over time as a result of a 300 km/h train crossing over soil cover depths of 2, 3, and 4 m.

3.7.2 Thrust Force

To evaluate thrust forces, measurements were carried out in two scenarios: static conditions and while high-speed trains were passing. The study included three different soil cover depths: 2, 3, and 4 m. Thrust forces were systematically assessed across a speed range of 100 km/h to 300 km/h. This thorough examination of thrust forces at different speeds and soil cover depths has unveiled several significant trends and discoveries, as depicted in Fig 3.19.

The relationship between train speed and thrust forces predominantly follows a non linear trend, signifying that thrust forces exhibit a consistent increase with higher speeds. This direct association between speed and thrust forces implies that higher-speed trains impose greater stresses on the bridge structure. This phenomenon is consistent across all examined soil cover depths. Remarkably, even at a speed of 100 km/h, thrust forces are already elevated when compared to the static scenario. This suggests that even moderately high speeds can introduce additional stress to the bridge structure, emphasizing the dynamic nature of high-speed train loads. As the train's speed escalates to 150 km/h, 200 km/h, and beyond, thrust forces exhibit a noticeable and sustained upward trajectory.

Fig 3.20 presents a comparative analysis of the influence of dynamic loading on thrust forces at various soil cover depths. The results demonstrate a notable disparity in thrust forces between a depth of 2 meters and depths of 3 meters and 4 meters. Specifically, when subjected to dynamic loading at a speed of 300 km/h, the thrust forces experienced at 3 and 4 m are approximately 59.5% and 74% lower, respectively, compared to the forces observed at 2 m. This finding emphasizes that shallower soil cover depths exhibit reduced efficacy in stress mitigation, making them less preferable for environments with high-speed rail applications. A distinct threshold effect emerges, resulting in a substantial and conspicuous surge in thrust forces, with this effect being particularly pronounced when considering a 2 m soil cover depth. Specifically, the transition from 250 km/h to 300 km/h results in a remarkable increase of approximately 10.7 kN/m in thrust forces, which stands in stark contrast to the mere 1.53 kN/m variation observed in the speed range from 100 km/h to 200 km/h. This discrepancy demonstrates a substantial 85.7 % decrease in variance between these two speed intervals.

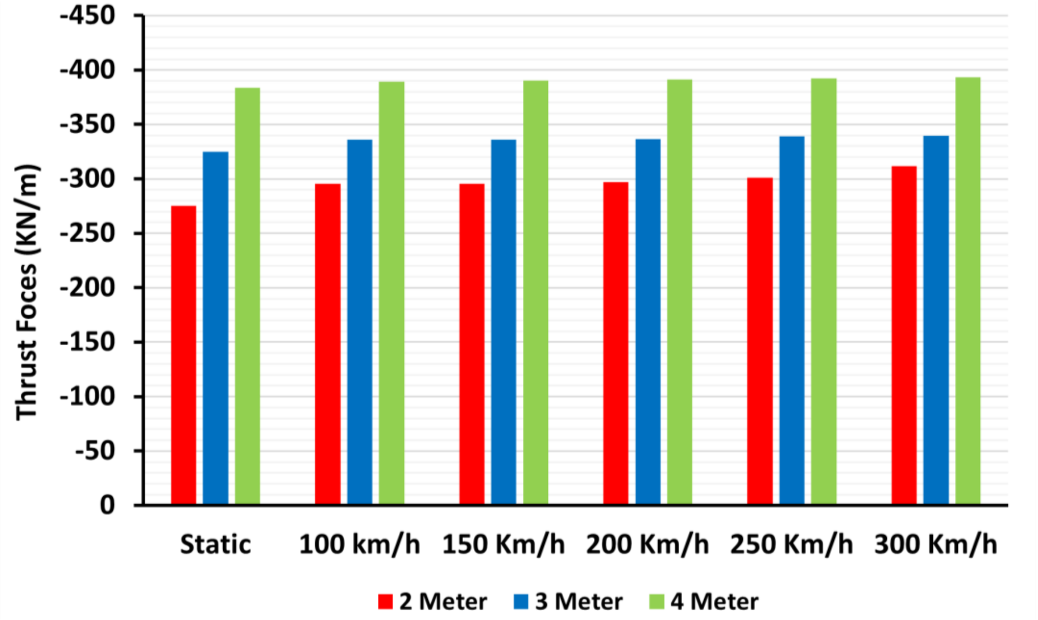

Fig 3.19 The influence of different high-speed trains on thrust forces at soil cover depths of 2, 3, and 4 m.

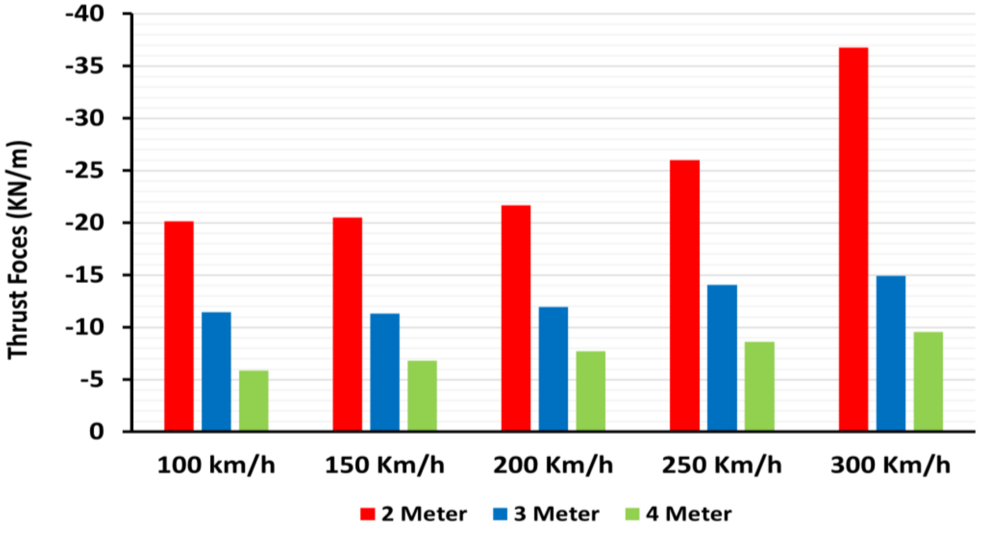

Fig 3.20 different high-speed trains dynamic effect on thrust forces at soil cover depths of 2, 3, and 4 m.

3.7.3 Bending Moment

This section presents analysis of a soil metal bridge's behavior concerning bending moments on the crown at varying soil cover depths 2, 3, and 4 m and speeds ranging from 100 km/h to 300 km/h. One significant finding of this study is the identification of the maximum achievable bending moment on the crown of the soil metal bridge, which registers at -10.20 kN.m. This value is specifically observed during the contraction stages of the bridge's behavior, highlighting the dynamic nature of bending moments experienced by the structure. It is worth noting that the change bending moment induced by the passage of trains, specifically resulting from the axis traveling over the bridge's crown, averages at a relatively small value of 0.06 kN·m. This value is considered negligible in the context of the overall structural behavior. To visually represent these findings, Figure 3.20 provides a graphical depiction of how different speeds impact the maximum bending moments encountered by the soil metal bridge crown across various soil cover depths. The bending moment diagram of the soil metal bridge, subjected to dynamic loading, closely mirrors a consistent profile, with slight fluctuations in both the peak and trough values. Specifically, we are focusing on the bending moment for the scenario involving a 300 km/h train speed and a 2 m soil cover depth, as illustrated in Figure 3.21. This observation implies that, throughout the dynamic loading event, the bridge's structural response maintains a generally similar pattern of bending moments.

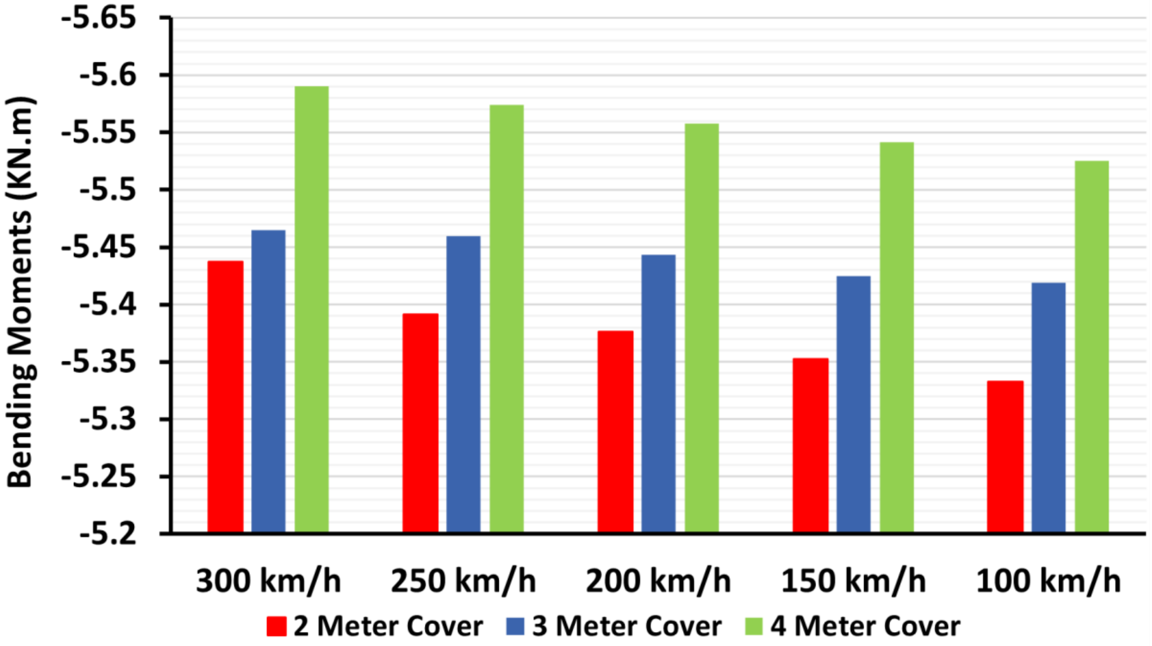

Figure 3.19 The influence of different high-speed trains on Bending Moment at soil cover depths of 2, 3, and 4 m.

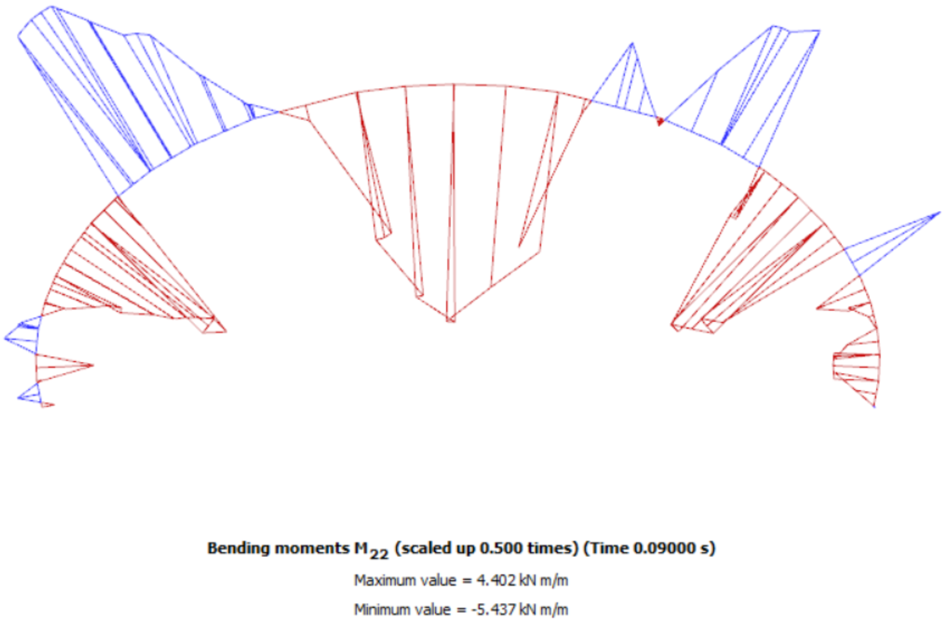

Figure 3.20 Bending moment corresponding to 300 km/h traveling train speed with a soil cover depth of 2 m.

One discernible trend in the analysis pertains to the influence of train speed on the bending moment experienced at the crown of the structure. As the velocity of trains surges, there is a corresponding increase in the magnitude of negative bending moments. This negative bending signifies a downward or tension force exerted upon the structure. This behavior finds its roots in the dynamic forces generated by high-speed trains. The acceleration to higher speeds prompts these trains to impose greater dynamic loads upon both the track and the structures situated above or beneath the track. Consequently, the dynamic forces contribute significantly to the augmentation of bending moments.

Another aspect of the analysis is the effect of soil cover depth on the bending moment, when evaluating various soil cover depths under identical speeds, a clear correlation emerges deeper soil cover corresponds to elevated bending moments. This correlation can be attributed to the mechanics of soil interaction. Deeper layers of soil provide enhanced resistance against the downward forces induced by passing trains. Consequently, structures ensconced within deeper soil cover contend with more substantial bending moments, as the soil adeptly opposes the applied loads.

The sensitivity of bending moment to changes in train speed emerges as an intriguing facet of the analysis. While there is a discernible shift in bending moment as speed varies, this shift transpires at a gradual pace. In essence, minor fluctuations in train speed do not yield drastic alterations in bending moment. Nonetheless, as train speed approaches the 300 km/h mark, a more pronounced upswing in bending moment becomes apparent. Analogous to the sensitivity to speed, the relationship between soil cover depth and bending moment displays gradual alterations. Nevertheless, the consistency of the trend remains evident greater soil cover depth invariably corresponds to higher bending moments. This constancy underscores the notion that structures ensconced within shallow soil cover are subject to comparatively lower bending forces, given the lesser resistance posed by the shallower soil layers.

3.8 Conclusion

In this chapter, an orthodox exposition of the findings and insights arising from the analysis of SMB behavior is reviewed. The exploration has encompassed a wide spectrum of conditions, including variations in soil cover depths and the dynamic interplay of train speeds. Through this examination, certain aspects of structural performance that offer practical guidance for the meticulous design and evaluation of soil metal bridges within the context of high-speed train transportation have been unveiled. The examination of soil-metal bridges has been comprehensive, delving deep into their reactions when faced with the dynamic forces produced by high-speed trains. Focus has been directed toward three critical aspects: crown deformation, thrust forces, and bending moments. These specific inquiries have led to the revelation of fundamental insights regarding the inherent structural integrity and vulnerabilities of these bridges when subjected to a range of scenarios. Among the noteworthy findings that have surfaced are:

- **The Influence of Soil Cover Depth:** The analysis unmistakably revealed the paramount importance of soil cover depth in mitigating deformations within soil-metal bridges. Deeper soil cover, as demonstrated across a range of train speeds 100 km/h to 300 km/h, consistently yielded decreased deformations.
- **Train Speed and Deformations:** Another observation from the study was the clear correlation between train speed and deformations. At all tested soil cover depths, higher train speeds led to more significant deformations. This phenomenon highlights the importance of considering train speed in the design, maintenance, and safety assessments

of soil-metal bridges. As high-speed rail networks continue to expand globally, the implications of this finding are substantial.

- **Dynamic Crown Deformation Patterns:** Delving deeper into the dynamics of deformations during train passage, the crown deformation patterns in response to various train speed over different soil cover depth is intricately linked to the position of the train's axis. The crown deformation evolved from an initial stable state through peak deformation and oscillations to a final steady state.
- **Thrust Forces and Speed**: The analysis of thrust forces under static and high-speed train conditions further deepened in understanding of soil-metal bridge behavior, thrust forces increase with higher train speeds, and this correlation is consistent across all soil cover depths. The relationship between speed and thrust forces exhibits a non-linear pattern, with trust forces increasing more rapidly as train speed increases. This non-linearity highlights the heightened vulnerability of the bridge to higher-speed trains, especially in the case of a shallow soil cover depth.
- **Bending Moments and speed**: Change in bending moments induced solely by the passage of trains, particularly from the axis traveling over the bridge's crown, maintain a relatively small average values deemed inconsequential within the broader structural context. However, it's crucial to highlight that the primary focus regarding bending moments pertains to those arising during the construction stage.

These findings, rooted in empirical analysis, hold implications for practical applications across engineering, transportation, and infrastructure development. They underscore the importance of planning and design in ensuring the safety and efficiency of high-speed train networks.

CHAPTER 4 SOIL-STRUCTURE INTERACTION OF HIGH-SPEED TRAINS OVER GEOCELL REINFORCED SOIL METAL BRIDGES

4.1 Introduction

The incorporation of geocells into Soil Metal Bridges (SMBs) introduces an innovative approach poised to impact the transportation industry, offering enhanced performance and potential cost savings. SMBs have demonstrated advantages, providing a blend of design flexibility, cost-effectiveness, and performance compared to traditional bridges. Ranging from 3 to 15 meters in length, these bridges are efficiently assembled using corrugated structural plates, making them a preferred choice for various road and railway projects. Their combination of a thin shell structure and engineered backfill grants flexibility and promises potential long-term cost benefits.

In recent times, geosynthetics have garnered attention as an effective tool for soil reinforcement, with extensive research exploring their behavior. Geogrids, recognized for protecting buried pipes and utilities, consistently exhibit notable reductions in deformation under cyclic loads, as evidenced by studies conducted by researchers such as Davarci et al. (2014) and Ferreira et al. (2015). These investigations have specifically highlighted the potential of geocells in the realm of geosynthetic-reinforced soil, showcasing a promising synergy with SMBs that has the potential to redefine construction standards and usher in a new era of transportation engineering marked by superior performance and cost-effectiveness.

Geocells, constructed from three-dimensional panels using high-strength polymers like polyethylene or polyolefin, have emerged as a transformative force, surpassing the performance of alternative soil reinforcement methods. Studies by Kargar et al. (2016) and Zhang et al. (2018) have underscored the reinforcement capabilities of geocells, forming interconnected cells that effectively confine surrounding materials and prevent lateral soil spread under applied loads. This confinement transforms geocells into resilient mattresses, redistributing loads over a broader area. Geocell reinforcement's efficacy depends on factors like geometric characteristics, material tensile strength, subgrade and fill compaction, and soil cover thickness. Optimizing these parameters enables geocells to maximize their potential, enhancing SMB performance by significantly increasing bearing capacity and reducing settlements compared to unreinforced soil.

Geocells have demonstrated their effectiveness in a wide range of geotechnical applications, encompassing embankments, foundations, retaining walls, and slopes. Through lateral confinement, geocells enhance the subgrade's bearing capacity, minimize settlements beneath footings and embankments, and bolster slopes against potential failure by curbing the lateral spread of infill materials. The integration of geocell reinforcement with Soil Metal Bridges (SMBs) brings forth a multitude of benefits. The enhanced bearing capacity, reduced settlements, and improved stability provided by geocells significantly contribute to the overall construction of SMBs. Moreover, geocells offer a cost-effective solution for optimizing SMBs performance, ensuring the bridges' longevity and structural integrity under diverse loading conditions. The adaptability of geocell-reinforced SMBs allows for efficient customization to meet specific project requirements, establishing them as highly versatile components in road and railway infrastructure development.

4.2 Three-Dimensional Modeling in Analyzing Culvert Behavior

Analyzing and designing SMBs presents significant challenges due to their complex behavior under various loading conditions. Traditional two-dimensional 2D models have limitations in capturing the actual deformation responses of SMBs accurately. In this paper, three-dimensional 3D finite element FE modeling has been utilised to investigate the geocell reinforcement with an aim to enhance the accuracy, load-carrying capacity, and stability of SMBs. Several relevant studies have highlighted the importance of considering the 3D nature of SMBs and the potential benefits of geocells in improving their structural performance. For instance, El-Sawy (2003) research demonstrates the significance of employing three-dimensional 3D modeling techniques in analyzing the behavior of culverts under the influence of truckloads. The study uses 3D Finite Element analyses to examine soil steel culverts. By considering two different soil modulus values Es = 30 and 80 MPa and two culvert behaviors isotropic and orthotropic, El-Sawy's work emphasizes the importance of 3D modeling in capturing the complexities of culvert response. Through comparative assessments, the study reveals that 3D modeling offers a more accurate representation of culvert behavior compared to traditional two-dimensional 2D approaches. Specifically, the results highlight how 3D modeling accounts for the better modeling of orthotropic culvert corrugated plates, leading to improved agreement with experimental data.

Sezen et al. 2008 conducted an extensive investigation into the field performance of four existing pipe-arch culverts located beneath highways. Their research considered a range of crucial factors such as backfill height, loading conditions, age of placement, and culvert geometry when selecting the culverts for analysis. Through static and dynamic load tests, they explored the response of these culverts to various conditions. The results revealed that the height of the backfill had a significant influence on culvert response, with the largest deflections occurring at or near the crown and shoulders of the culverts. Symmetrical deflection patterns were observed for symmetrical loading around the longitudinal vertical plane through the crown. Dynamic loading produced deflections approximately 10–20% smaller than static loading, and the speed of the test trucks had varying effects on different culverts. Strain gauge measurements indicated that the crown of the culverts experienced tension and compression resembling beam flexure during loading, with some asymmetry attributed to culvert plate geometry and potential irregularities in soil pressure distribution. Culvert deflections decreased nonlinearly with increasing soil backfill depth, highlighting that deflections and strains increased significantly when the backfill depth was less than 0.9 m.

1.1 Effectiveness of Geocells

Geocell reinforcement has gained significant attention as an effective alternative for soil stabilization and protection of underground utilities. There have been various studies that have examined the effectiveness of geocells and compared their performance with other soil reinforcement techniques. A study by Dash et al. (2004) showcased the remarkable load-carrying capacity improvement offered by geocells. The researchers found that geocells increased the load capacity of reinforced soil up to three times compared to unreinforced soil. Furthermore, Hegde et al. (2015) investigated geocells as a soil reinforcement technique for protecting underground utilities from cyclic loads and reported that geocells significantly reduced deformation and provided improved protection for these utilities. Tafreshi et al. (2010) conducted a comparative study between planar geotextiles and three-dimensional geotextiles. They concluded that geocell reinforcement is stiffer, carries greater loading, and experiences less settlement than equivalent planar reinforcement systems. The elastic modulus of the geocell was identified as a key factor affecting the performance of geocell-reinforced sand by Pokharel et al. (2010). Additionally, Dash (2010) explored the influence of soil relative density on the performance of geocell-reinforced sand foundations and suggested higher soil compaction for effective utilization of geocell reinforcement. Dash (2012) further emphasized the impact of geocell characteristics, such as strength, stiffness, aperture size, and rib orientation, on the performance of reinforced sand foundations. Neto et al. (2013) proposed an analytical approach to predict the bearing capacity of geocell-reinforced soil, considering the geometric characteristics of geocell reinforcement. Davarifard et al. (2015) presented a simplified method for predicting the load-settlement response of geocell-reinforced sand, incorporating the effects of soil and reinforcement stiffness. Figure 4.1 presents data on the bearing pressure-settlement of footings on both unreinforced and geocell-reinforced beds with no embedment depth. This figure demonstrates that as the number of geocell layers increases indicating a deeper reinforced zone, both stiffness and bearing pressure at a given settlement level increase significantly.

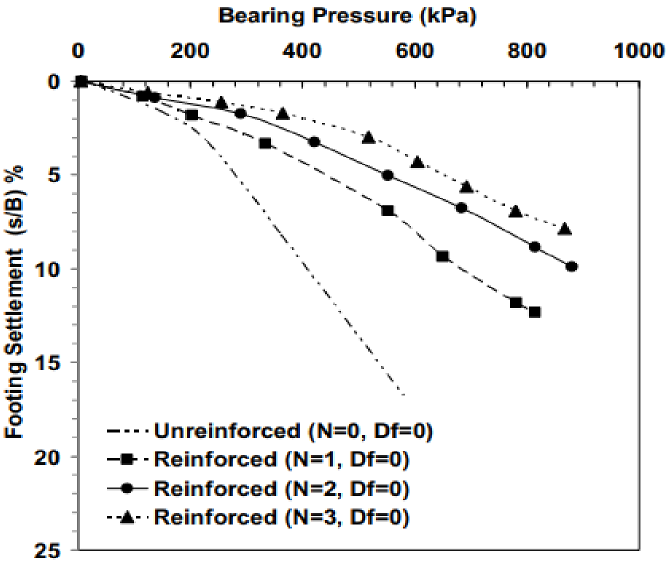

(a)

Figure 4.1 Variation of bearing pressure with footing settlement (Davarifard et al., 2015).

The data in Figure 4.2 also highlights that the benefits of geocell reinforcement become more pronounced as the footing settlement increases. This improved performance is attributed to the internal confinement provided by geocell reinforcement, which depends on factors such as the tensile strength of the reinforcement, friction at the soil-reinforcement interface, and the confining stress generated within the geocell pocket due to passive resistance offered by the 3D structure of the geocell.

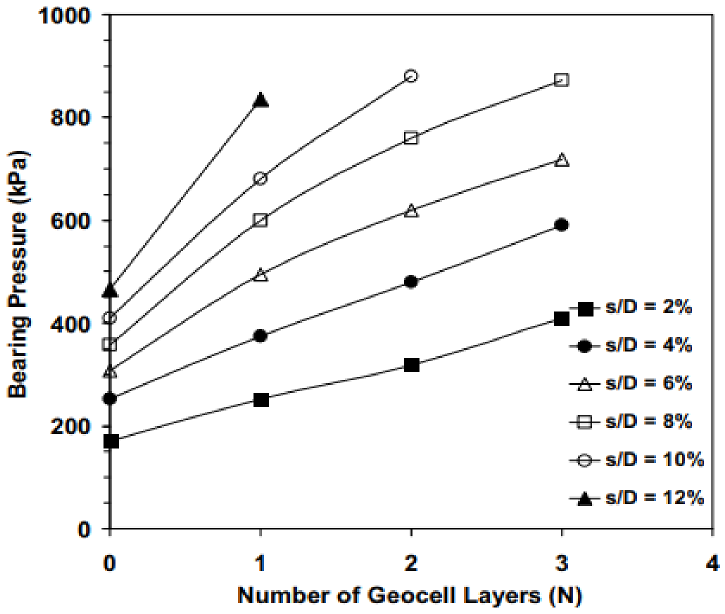

(b)

Figure 4.2 Variation of bearing pressure number with various geocell layers count at different values of settlement (Davarifard et al., 2015).

Laboratory tests have been instrumental in evaluating the improvement effect of geocell reinforcements under vertical loading. Tafreshi et al. (2010) compared the bearing capacity improvement between planar geotextiles and three-dimensional geotextiles, highlighting the superior performance of geocell reinforcement. Pokharel et al. (2010) investigated the parameters influencing the behavior of single geocell-reinforced soil under static loading and identified the elastic modulus of the geocell as a significant factor. To further understand the behavior of geocell-reinforced soil, large-scale triaxial tests using encased soil samples have been conducted. (Chen et al. 2013; Khedkar et al., 2009; and Nair et al., 2015) reported that the shear strength of sand increased due to induced apparent cohesion from confinement offered by geocells. Additionally, Bathurst et al. (1993) and Rajagopal et al. (1999) observed an increase in apparent cohesion with the strain at failure of the geocell and the diameter of the geocell pockets.

Lekshmi (2016) conducted plate load tests under repeated loading to examine the effects of geocell reinforcement in unpaved granular layers. The study compared the permanent deformation of reinforced and unreinforced sections and observed that geocell reinforcement effectively reduced permanent deformation compared to the unreinforced sections. It was noted that both reinforced and unreinforced sections experienced an increase in total and permanent deformation with an increase in the number of loading cycles. However, the rate of permanent deformation was higher during the initial cycles and decreased as the number of cycles increased. Furthermore, the permanent deformation per cycle was significantly higher in the unreinforced sections compared to the reinforced sections. The study also revealed that the resilient deformation in the reinforced sections was substantially lower than that in the unreinforced sections.

Lekshmi (2016) statistical analysis of the resilient deformation data showed that the mean value of resilient deformation was higher in the unreinforced sections. Additionally, the coefficient of variation of resilient deformation was higher in the unreinforced sections, indicating that the resilient deformation in the unreinforced sections exhibited more deviation from the mean value compared to the reinforced sections. Calculations of the resilient modulus demonstrated that the reinforced sections had significantly higher resilient modulus values compared to the unreinforced sections. This observation highlights the ability of geocell reinforcement to improve the resilient response of soil metal bridges, thereby reducing deformation under cyclic loading. One important finding from the Lekshmi (2016) study was that increasing the thickness of the reinforced section resulted in a decrease in permanent deformation or rut depth. Rut depth reduction analyses indicated that even 150 mm reinforced sections performed significantly better than their unreinforced counterparts during the long-term operation of pavements. This reduction in rut depth not only enhances the structural integrity of the soil metal bridge but also offers potential savings in aggregate materials, leading to a reduction in carbon footprint.

Mahgoub and El Naggar (2020) conducted a study to evaluate the advantages of a coupled stress-bridging system utilizing Tire-Derived Aggregate TDA and geocells for buried metal culverts. The objective was to investigate the interaction between the soil and structure while assessing the system's performance in mitigating surface settlement and reducing culvert stresses. Six full-scale tests were conducted, accompanied by the development of 3D finite-element models to analyze the underlying mechanisms. Additionally, a comprehensive parametric study was undertaken to examine the influence of various factors on the system's effectiveness. The findings yielded several noteworthy conclusions. The results indicated a significant reduction in culvert stresses when TDA was employed as a backfill material above the culverts. However, it was observed that punching shear failure occurred in the top layer. In the initial test configuration, the inclusion of geocell reinforcement resulted in an approximate 40% increase in the ultimate load capacity, effectively preventing soil failure from spreading. The geocell layer acted as a stress-absorbing medium, proficiently distributing tension forces and enhancing stress distribution beneath the loaded area. The width of the geocell layer did not have a substantial impact on the performance, as long as it exceeded 0.8 times the culvert diameter. Hence, it is recommended that the geocell layer should be 0.5 m wider than the trench, covering the loaded area adequately. Optimum results were obtained when the geocell layer was positioned directly beneath the loaded area, as deeper placement led to noticeable increases in surface settlement. Increasing the number of geocell layers exhibited a positive influence on the stiffness of the top granular layer, enhancing stress bridging over the buried culvert and reducing surface settlement. Moreover, incorporating stiffer granular materials in the top layer, in conjunction with TDA, significantly amplified the stress-arching mechanism over the culverts. Interestingly, in certain scenarios, the introduction of a geocell layer with weaker materials produced comparable behavior to using stronger materials without a geocell layer. The efficacy of geocell reinforcement varied depending on the depth of the culverts. Shallow depths yielded substantial improvements in transferred pressure and surface settlement when geocells were utilized. However, for backfill cover depths ranging from 2 times to 3 times the culvert diameter, the enhancements resulting from geocell reinforcement were more moderate. Furthermore, the impact of the geocell layer on system behavior was marginal when the culvert placement depth exceeded 3 times the culvert diameter.

4.3 Numerical Modelling

4.3.1 Geocell Numerical Modelling

Geocell has been modeled as an equivalent material with greater cohesion than the surrounding infill soil while matching the friction angle of the infill. This design is achieved through the application of membrane stress within the geocell walls, which effectively confines soil particles, resulting in an apparent increase in cohesion within the soil (Henkel and Gilbert, 1952). The additional confining stress, denoted as $\Delta\sigma_3$, is a fundamental factor in this modeling process. It is described by Henkel and Gilbert (1952) and is determined by various parameters such as the diameter D of the sample at a specific axial strain at soil failure ε_a, circumferential strain of soil at failure ε_c, the initial diameter of the geocell pocket D_o, and finally, the modulus of the membrane M. The modulus of the membrane is a key variable that can be obtained from load-strain curves generated in wide-width tensile strength tests on geogrids. The geocell additional confining stress equation by Henkel and Gilbert (1952) is given as:

$$\Delta\sigma_3 = \frac{2M\varepsilon_c}{D}\frac{1}{1-\varepsilon_c} = \frac{2M\left(1-\sqrt{1-\varepsilon_a}\right)}{D_o 1-\varepsilon_a} \tag{50}$$

Bathurst and Karpurapu (1993) conducted triaxial compression tests on a single cell reinforced granular soil sample to further validate the geocell's effects on soil behavior. They constructed a Mohr circle for both reinforced and unreinforced soil and estimated apparent cohesion. The results indicated that due to the confinement effect of the geocell, the cell pressure σ_3 increased to $\sigma_3 + \Delta\sigma_3$, and normal stress σ_1 also increased to σ_1^r.

More empirical research conducted by Rajagopal et al. (1999), where they performed triaxial tests on various geocell-reinforced sand samples. Their findings offer valuable insights into the geocell's impact on soil mechanics and cohesion. In their study, Rajagopal et al. (1999) investigated the behavior of single-cell and multi-cell reinforced sand samples. They reached the conclusion that the most accurate estimation of apparent cohesion was obtained when there were at least three interconnected cells within the geocell structure. This suggests that the structural configuration of the geocell, particularly the interconnections between cells, plays a crucial role in determining its effectiveness in enhancing soil cohesion. Furthermore, Rajagopal et al. (1999) provided a specific formula for calculating the apparent cohesion induced by the geocell layer as:

$$C_r = \frac{\Delta\sigma_3\sqrt{K_p}}{2} \tag{51}$$

Where, K_p represents the passive earth pressure coefficient, and $\Delta\sigma_3$ stands for the extra confining stress generated by the geocell's membrane stress. To determine the cohesive strength of the reinforced layer, the apparent cohesion induced by the geocell is combined with the native cohesion of the infill soil.

The modeling of geocell behavior has evolved through analytical studies, as highlighted by Mitchell et al. (1979). In their work, analytical solutions were developed to assess the load-carrying capacity of base courses reinforced with grid cells like geocells. The analytical method considered various failure modes, including bearing capacity, bending, durability, excessive rutting, cell penetration of subgrade, cell bursting, and cell wall buckling. This comprehensive approach aimed to capture the diverse failure mechanisms that could occur in geocell-reinforced soil systems. One of the challenges in geocell modeling, as pointed out by Mitchell et al. (1979), is the complex structure of geocell itself and the stress-dependent nature of sand stiffness. These complexities make it difficult to accurately estimate the modulus of geocell, a crucial parameter in modeling geocell behavior. Latha (2000) contributed to geocell modeling by proposing an empirical relation that establishes a connection between the modulus numbers of the soil. This empirical relation likely aids in simplifying the estimation of soil properties within geocell-reinforced systems, where Kr and Ke represent the modulus numbers of the geocell-soil composite and unreinforced soil, respectively. The Young's modulus parameter Ke corresponds to the modulus number in the hyperbolic model Duncan and Chang (1970), and M represents the tensile stiffness of the geocell material. Latha (2000) equation is given as:

$$K_r = K_e + 200M^{0.16} \tag{52}$$

To express the Young's modulus of geocell-reinforced sand E_g, an empirical nonlinear equation has been developed, as described by Latha (2000) and Rajagopal et al. (2001). This equation considers the atmospheric pressure P_a, the secant modulus of the geocell material M, confining pressure σ_3, the Young's modulus parameter of unreinforced sand K_u, and the modulus exponent of unreinforced soil n. This equation takes the form:

$$E_g = P_a(K_u + 200M^{0.16})\left(\frac{\sigma_3}{P_a}\right)^n \tag{53}$$

4.3.2 Numerical Modeling of Honeycomb Geocell

Numerical modeling of geocells has evolved significantly, from early 2D approaches to sophisticated 3D simulations that account for the stress-dependent behavior of soil and the complex geometry of geocells. Precise modeling of honeycomb geocells holds a central position in comprehending the interaction of these structures with soil and other materials. Geocells are three-dimensional structures, and their shape and curvature significantly influence their mechanical behavior when subjected to various loads and environmental conditions. The first step in modeling honeycomb geocells in Plaxis3D is to capture their actual shape. This is achieved by digitizing photographs taken from the top of the geocell. The digitization process allows for the extraction of the geocell's geometry, which can then be translated into a numerical model. Additionally, the curvature of the geocell is represented by a sinusoidal curve. Once the digitization is complete, AutoCAD is employed to create an accurate representation of each honeycomb geocell as represented in Figure 37. The dimensions of the geocell are crucial, and in this case, the model covers a total area of 15 x 9 m to match the real-life size required for the soil-metal bridge application. The next step involves importing the AutoCAD-drafted geocell into Plaxis3D. The geocell's geometry is represented in Plaxis3D as polycurves. geogrid elements are assigned to the polycurves representing the geocell's geometry. This step is essential for defining the reinforcement structure within the model. Geogrid elements are used to simulate the geocell's interaction with the surrounding soil. To match the real-life honeycomb geocells, the imported polycurves are extruded by 0.15 m in Plaxis3D.

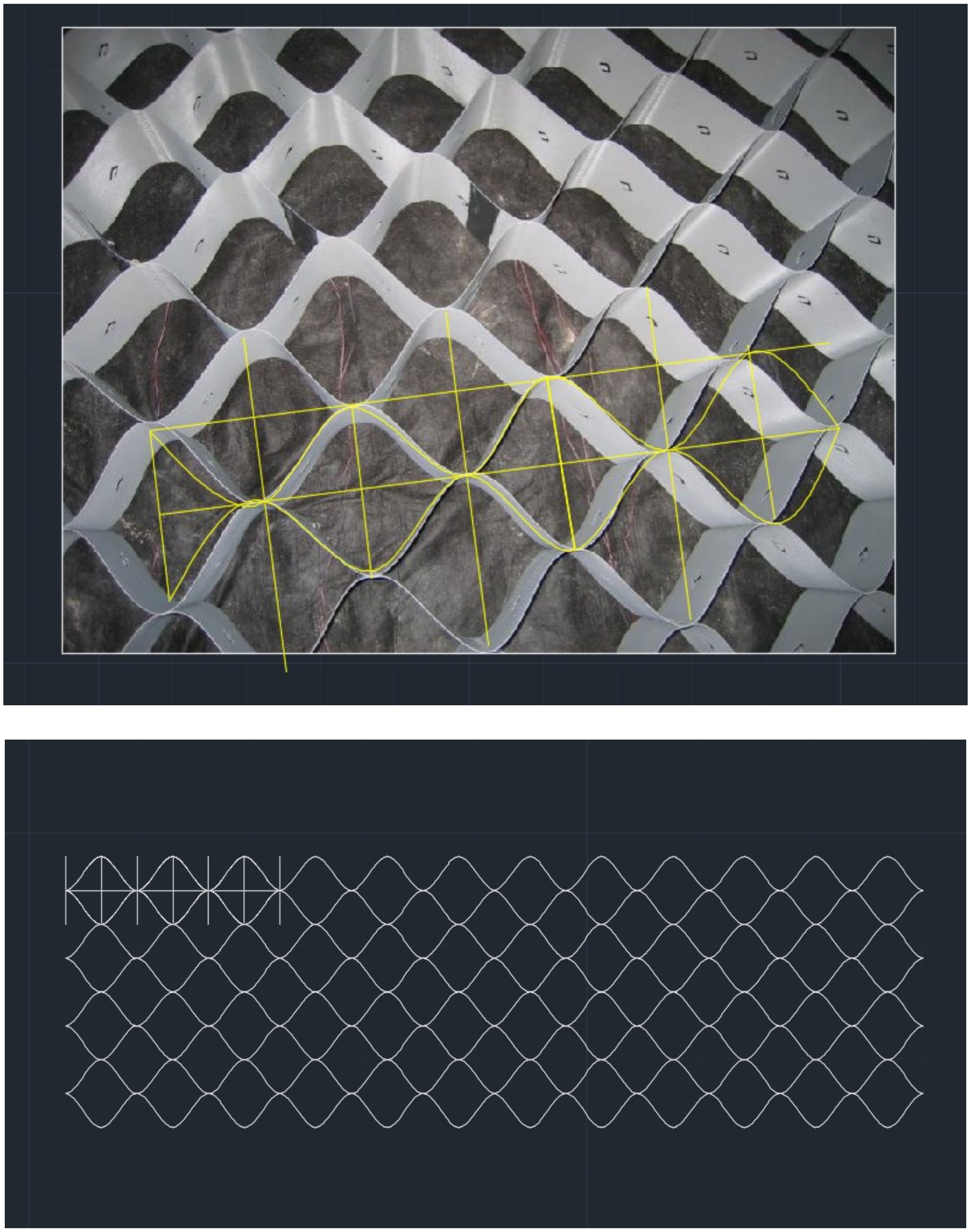

Figure 3 AutoCAD representation of Geocell drafting

This extrusion accurately represents the three-dimensional nature of geocells. To investigate the mechanisms of interaction between the geocell reinforcement and surrounding soil, interface elements are added. These elements correspond to pairs of nodes, aligning with soil element or

Geogrid nodes. Properly defining the interface elements is essential for capturing the stress distribution at the interfaces of different materials accurately.

4.4 Parametric Modeling and Conditions

In this extensive research undertaking, three distinct models have been crafted to explore the use of geocell reinforcement in a challenging context. These models are specifically designed to address the scenario of weak soil backfill beneath a high-speed train track where trains traverse at speeds of up to 300 km/h. The core objective of this study is the thorough evaluation of the structural stability of the soil-metal bridge SMB system under these demanding conditions. The models are differentiated by their geocell configurations. The first model integrates a solitary geocell layer positioned at a depth of 40 cm below the ballast layer. The second model incorporates a dual layer geocell system with a 30 cm vertical gap between these two layers. A visual representation of this geocell placement concerning the SMBs can be observed in Figure 4.3, which illustrates the precise positioning of geocells in accordance with SMBs.

It's vital to underline that the boundary conditions and structural dimensions applied to the SMBs in these models remain uniform and consistent. The importance of boundary conditions in the analysis lies in their influence on the mesh generation and subsequent deformation capture. A "very fine" global coarseness was applied to create meshes for each model, with specific emphasis on refining the metal plates' mesh to accurately represent deformation. The mesh refinement, guided by relative element size factors, ensured consistency and efficiency in the analysis process. Regarding boundary conditions, default settings were maintained throughout, including a free upper surface, fixed sides to restrict lateral movements, and a fully fixed bottom to prevent vertical movement. The interface between the soil and the Corrugated Metal Plate (CMP) was intricately modeled using specialized interface elements designed for capturing contact surface behavior between materials with differing properties. The use of weak soil as backfill in such a scenario is not typically considered ideal for ensuring structural rigidity. This is particularly crucial when high-speed trains are involved, as their passage exerts significant dynamic loads on the bridge and its supporting soil. The presence of geocell reinforcement in this study is intriguing, as it seeks to fully explore the potential and effectiveness of geocell technology in improving the performance of the soil-bridge system under these challenging conditions.

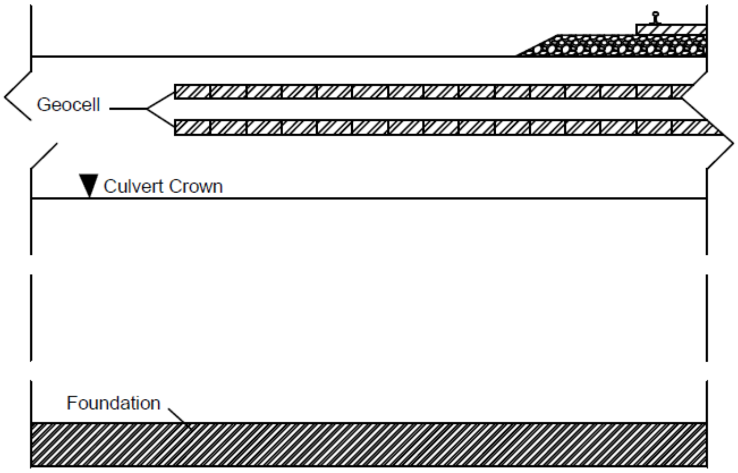

Figure 4.4 Geocell layout and positioning in accordance with SMBs

Table 4.1 Weak soil material properties

Properties	Weak Soil	Unit
Soil Model	HSs	-
Drainage Type	Drained	-
γ_{unsat}	15	kN/m^3
γ_{sat}	15	kN/m^3
E_{50}^{ref}	15e3	kN/m^2

E_{oed}^{ref}	12e3	kN/m^2
E_{ur}^{ref}	45e3	kN/m^2
v_{ur}	0.3	-
G_o^{ref}	-	kN/m^2
$\gamma_{0.7}$	-	-
m	0.5	-
c'_{ref}	0	kN/m^2
$\varphi\ phi$	30	°
ψ psi	0	°

The effectiveness of geocell reinforcement is closely tied to various parameters, both related to the soil and the geocell itself. These parameters are presented in detail in Table One, allowing for a comprehensive understanding of how different soil and geocell characteristics impact the performance of the models. Understanding these parameters is pivotal to comprehending the outcomes of the study and to draw meaningful conclusions regarding the suitability of geocell reinforcement in such scenarios. From a structural engineering perspective, this research not only provides insights into the behavior of the soil-bridge system but also offers valuable data for designing and optimizing railway infrastructure in regions where weak soil conditions are prevalent.

4.5 Results and Discussions

4.5.1 Crown Deformation

The multifaceted challenges contributing to geocell failure, such as soil conditions exceeding load-bearing capacity, suboptimal design, and shear banding induction in soft soils, are further emphasized when considering the impact of dynamic loads from high-speed trains. These loads pose a substantial challenge, overwhelming the geocell's stabilization capacity and causing localized deformation and stress concentration. The rapid and repetitive loading, not aligned with the intended geocell function, underscores the imperative need for optimization in geocell design based on specific soil conditions and loading requirements.

This need for optimization becomes particularly apparent when examining the deformation data presented in Figure 4.3. The data illustrates a clear trend of increasing deformation over time in all three cases. Initially t=0, no deformation is observed in any case, but as time progresses, distinctions emerge. In the scenario without Geocell reinforcement, the deformation gradually increases, reaching approximately -3.21 mm at t=1.26 seconds. In contrast, cases with Geocell reinforcement, whether one or two layers, experience a significant upsurge in deformation, with values of approximately -4.78 and -5.75 mm, respectively, at the same time point.

Analyzing the deformation data unveils a comprehensive perspective on how the presence of Geocell reinforcement influences crown deformation during dynamic loading. Numerically, it is evident that Geocell reinforcement leads to increased deformation compared to the scenario without Geocell. For one Geocell layer, the maximum deformation is approximately 70.70% higher than the no Geocell case, signifying a substantial increase. In the case of two Geocell layers, the maximum deformation is approximately 79.12% higher than the no Geocell case, indicating an even more significant increase in deformation. This linkage highlights the intricate relationship between geocell challenges and their tangible effects on deformation under dynamic loading conditions.

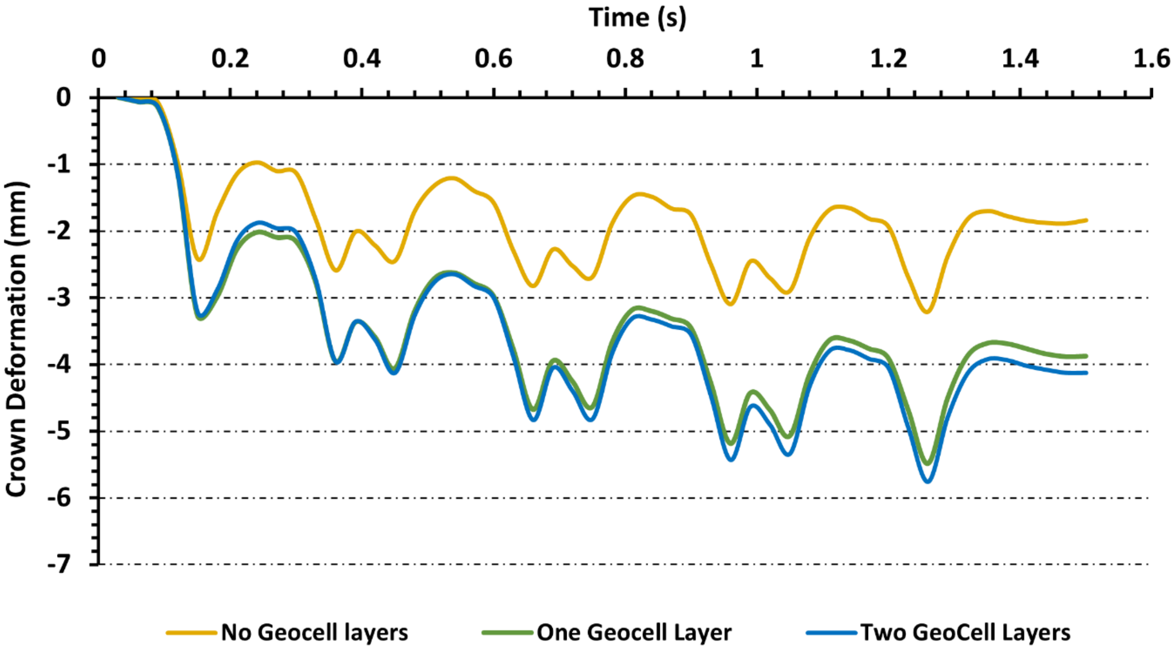

Figure 4.5 Crown Deformation over time for a traveling train speed of 300km/h

The anticipation that Geocell reinforcement would alleviate deformation has been contradicted by the results. This unexpected outcome challenges the widely accepted belief that Geocell reinforcement consistently diminishes deformation in soft soils subjected to high-speed train loads. The observed behavior implies that the soft soil in these particular scenarios exhibits a high degree of compressibility, rendering the Geocell structure ineffective in mitigating lateral displacement and stress concentration induced by the dynamic train loads. In summary, the behavior of the three cases can be summarized as follows:

No Geocell Reinforcement:

- The case without Geocell reinforcement exhibits consistently lower deformation values compared to the cases with Geocell reinforcement at the early stages of the analysis.

- As time advances, the deformation in this case gradually increases, but it maintains a lower rate of increase compared to the cases with Geocell reinforcement.

One Geocell Layer:

- Initially, the case with one Geocell layer shows the least deformation, signifying the early effectiveness of Geocell reinforcement in restricting deformation.
- However, as time elapses, the deformation in this case surpasses that of the case with no Geocell reinforcement, and the rate of increase in deformation is significant.

Two Geocell Layers:

- The case with two Geocell layers initially exhibits lower deformation than the case with one Geocell layer, but higher deformation compared to the case with no Geocell reinforcement.
- Similar to the case with one Geocell layer, the deformation increases significantly over time, surpassing the case with no Geocell reinforcement.

The behavior of the Geocell reinforcement in response to the high-speed train loading can be comprehensively analyzed by examining the deformations it experienced in all three directions: x, y, and z. Figures 4.4 to 4.7 provide a visual representation of these deformations, offering insights into the observed phenomena. It becomes evident that the region of deformations primarily occurs in the z direction and is primarily concentrated beneath the ballast layer where the majority of soil stress is concentrated. This observation implies that the Geocell structure became dislocated from each other, ultimately leading to its failure in fulfilling its intended purpose.

In examining the deformations in the z direction, it is clear that the Geocell reinforcement did not function as expected. The Geocell structure should have effectively distributed the load and mitigated deformations in this direction. However, the significant deformations concentrated beneath the ballast layer indicate that the Geocell was unable to withstand the immense pressure and lateral forces imposed by the high-speed train. As a result, the Geocell elements became dislocated, and the soil beneath the ballast layer experienced substantial deformation. This unexpected behavior challenges the conventional understanding of Geocell reinforcement, which is generally regarded as a reliable method for limiting deformation in soft soils. Moreover, it is crucial to note that the behavior of the Geocell reinforcement differed between the top and bottom layers. The bottom layer of Geocell experienced comparatively less deformation, which is evident in Figures 4.4 to 4.6. This variation in behavior was particularly noteworthy, as the conventional expectation was that the Geocell structure, especially when applied in multiple layers, would enhance its ability to reduce deformations on the sub-ballast mat SMB crown.

Initially, during the first 0.3 seconds of loading, the Geocell reinforcement in the bottom layer did exhibit some success in limiting deformations on the SMB crown. However, as time progressed, it became apparent that the accumulative vertical displacement led to increased vertical deformation on the crown. This behavior can be attributed to Geocell's inability to maintain its intended structural integrity and effective load distribution over an extended duration. In essence, the Geocell reinforcement, despite its initial promise, demonstrated an inability to withstand the extreme pressures and lateral forces exerted by the high-speed train on the soft soil beneath the ballast layer. This unexpected behavior has challenged the conventional wisdom that Geocell reinforcement is universally effective in reducing deformation in such scenarios. The dislocation of Geocell elements and the resulting concentration of deformations beneath the ballast layer suggest that the soil in this specific case exhibits high compressibility, making it highly susceptible to deformation under dynamic train loads.

This unanticipated outcome calls for a reevaluation of Geocell reinforcement strategies in scenarios involving soft soils and high-speed train loads. It highlights the need for a more comprehensive understanding of soil behavior and the limitations of Geocell structures in specific contexts. Additionally, it emphasizes the importance of considering the dynamic nature of loading, which may have different effects compared to static loading conditions.

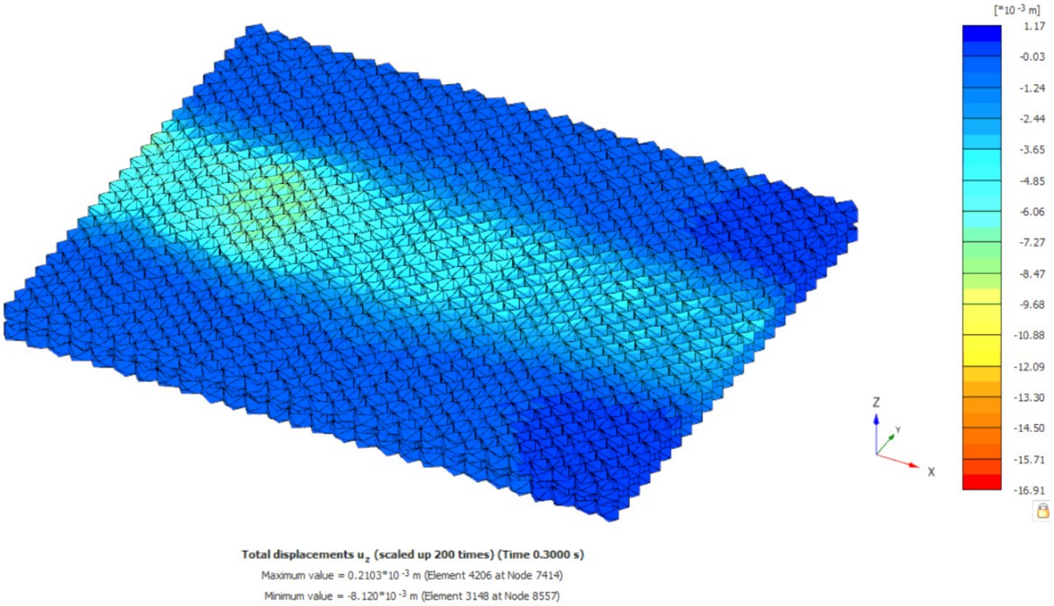

Total displacements u_z (scaled up 200 times) (Time 0.3000 s)

Maximum value = 0.2103*10 $^{-3}$ m (Element 4206 at Node 7414)

Minimum value = -8.120*10 $^{-3}$ m (Element 3148 at Node 8557)

Figure 4.6 Honeycomb Geocell top layer Z-direction deformations at 0.3 seconds

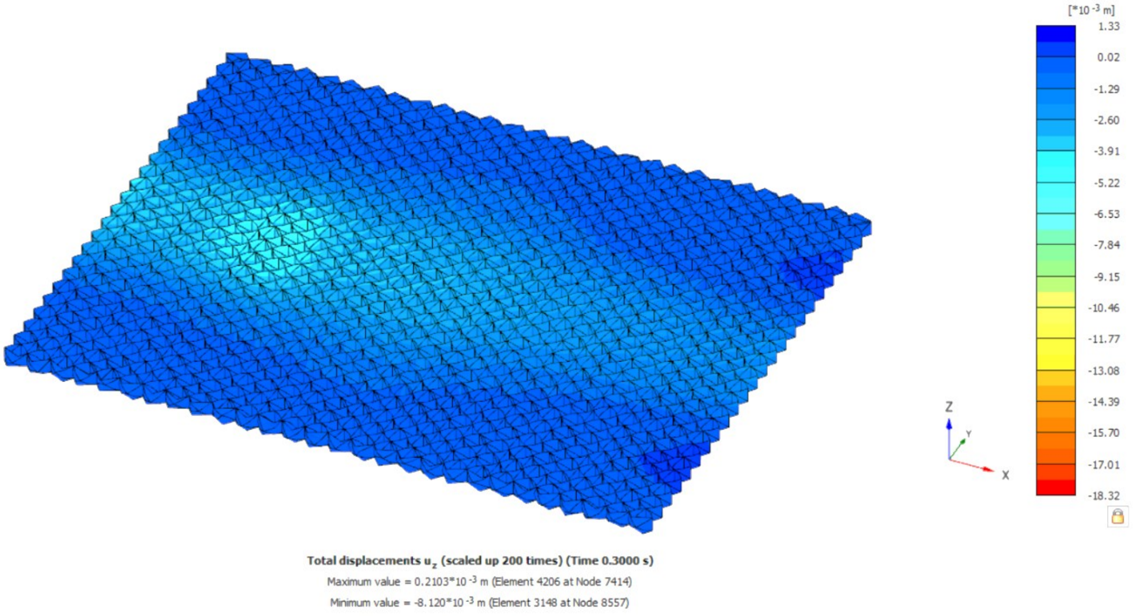

Total displacements u_z (scaled up 200 times) (Time 0.3000 s)

Maximum value = $0.2103*10^{-3}$ m (Element 4206 at Node 7414)

Minimum value = $-8.120*10^{-3}$ m (Element 3148 at Node 8557)

Figure 4.7 Honeycomb Geocell bottom layer Z-direction deformations at 0.3 seconds

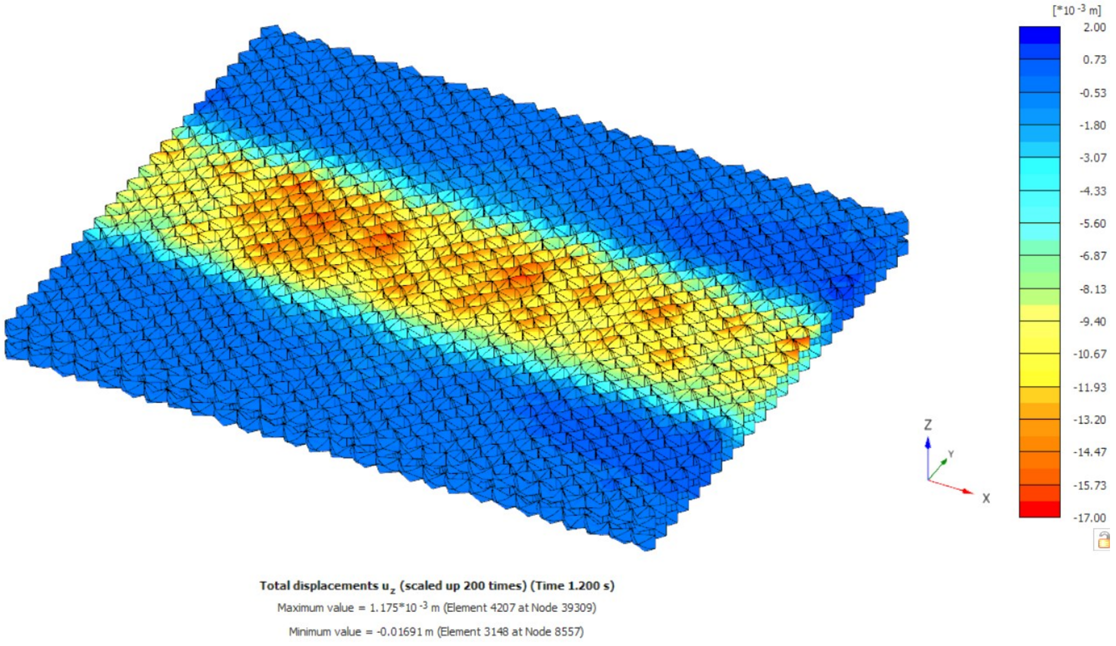

Total displacements u_z (scaled up 200 times) (Time 1.200 s)

Maximum value = $1.175*10^{-3}$ m (Element 4207 at Node 39309)

Minimum value = -0.01691 m (Element 3148 at Node 8557)

Figure 4.8 Honeycomb Geocell top layer Z-direction deformations at 1.2 seconds

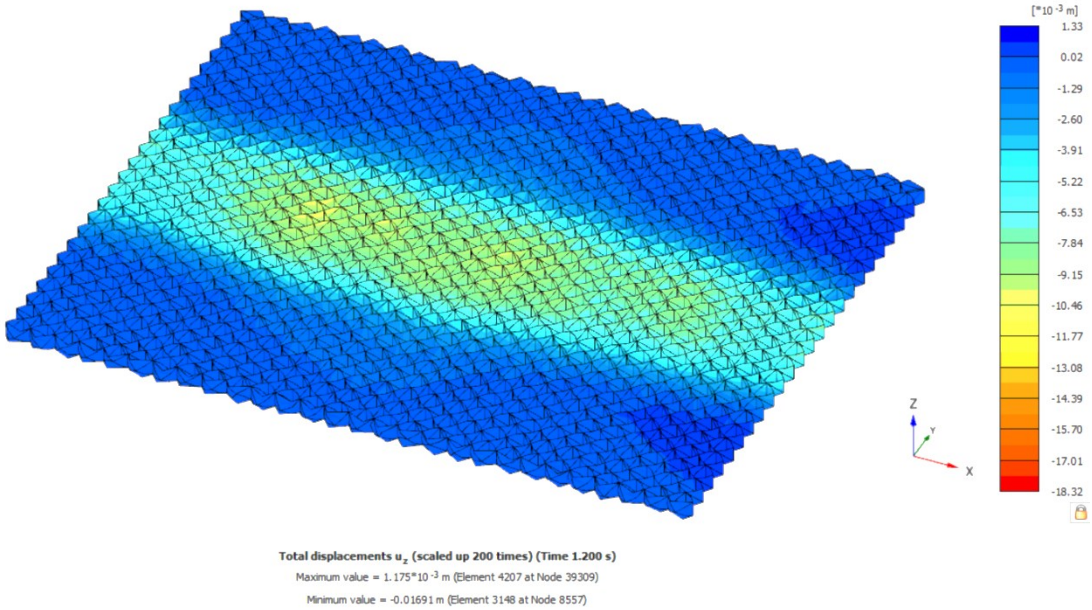

Figure 4.9 Honeycomb Geocell bottom layer Z-direction deformations at 1.2 seconds

4.5.2 Crown Accelerations

4.5.2.1 Z-Direction Acceleration

The acceleration behavior of a soil-metal bridge crown during the passage of a high-speed train operating at 300 km/h has been studied across three scenarios: No Geocell Layers, One Geocell Layer, and Two Geocell Layers. This investigation provides valuable insights into the dynamic behavior of the crown under varying levels of Geocell reinforcement.

The acceleration behavior in the absence of Geocell layers exhibits a diverse range of values. Figure 4.8 presents a mix of positive and negative values, where negative values denote downward acceleration, while positive values signify upward acceleration. During the passage of the train, the acceleration values vary widely, ranging from a minimum of -13.972 m/s² to a maximum of 22.055 m/s².

In the presence of One Geocell Layer, the acceleration behavior continues to display a combination of both positive and negative values. This indicates that the Geocell reinforcement does not eliminate the dynamic forces acting on the crown. The acceleration values with One Geocell Layer vary between -11.649 m/s² downward and 31.972 m/s² upward. With the highest level of reinforcement, Two Geocell Layers, the acceleration pattern remains diverse, with a mix of positive and negative values. The acceleration values in this scenario range from -26.753 m/s² downward to 32.741 m/s² upward.

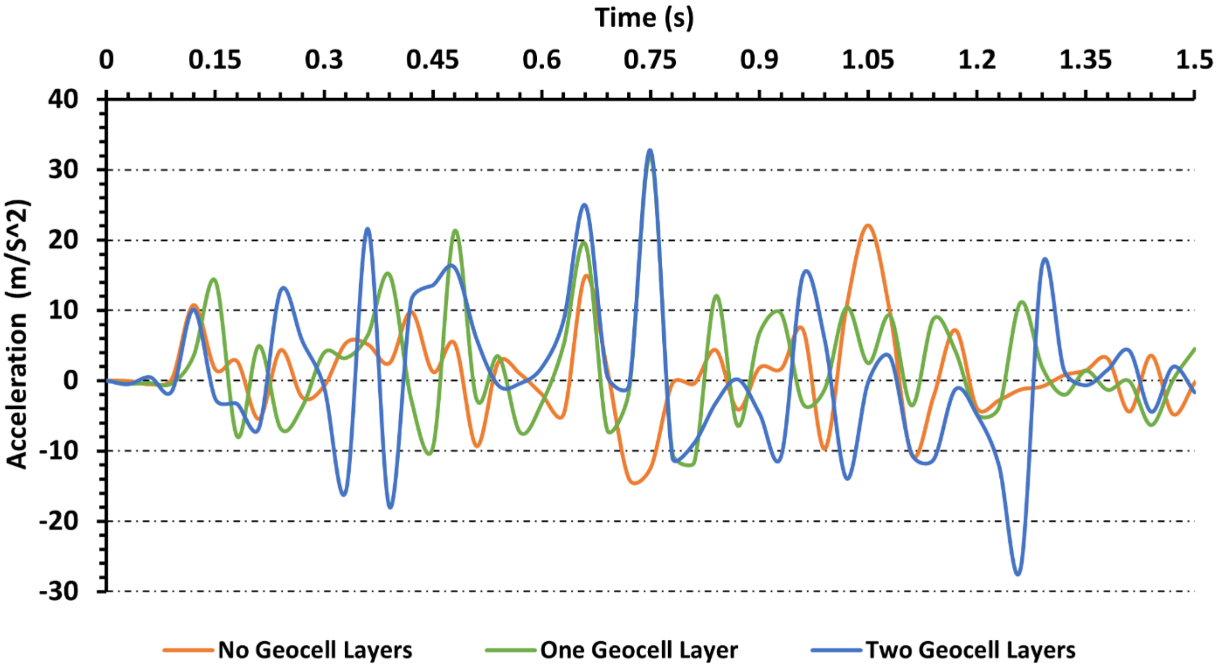

Figure 4.10 Crown Acceleration in Z-direction as a function of time for a traveling train speed of 300km/h

In all three scenarios, the acceleration behavior is characterized by diverse values, indicating significant variations in the forces acting on the bridge crown. This suggests that the Geocell reinforcement, even with Two Geocell Layers, does not completely eliminate the dynamic forces.

One notable observation is the presence of higher peak acceleration values in scenarios with Geocell Layers. In the case of Two Geocell Layers, the maximum acceleration reaches 32.741 m/s^2, which is notably higher than in the scenario with No Geocell Layers 22.055 m/s^2.

The phenomenon of higher accelerations in reinforced cases with Geocells can be attributed to the complex interplay of various factors. Geocells are engineered to confine and stabilize the soil, which is an effective technique for mitigating deformations and improving load-bearing capacity in geotechnical applications. However, in the context of soil-metal bridge crowns subjected to high-speed train loads, the presence of Geocells can paradoxically lead to higher accelerations. This seemingly counterintuitive effect can be explained through a detailed analysis of the mechanics involved. Geocells serve as confinement structures that envelop the soil beneath them. They are typically constructed using interconnected cells, forming a lattice-like framework. The intention behind this is to confine the soil within the cells, effectively restraining its lateral movement. This confinement restricts the lateral expansion of the soil, increasing the stress within the confined region, particularly right above the crown. High-speed trains generate dynamic effects, such as vibration and oscillation, in addition to static loads. The dynamic nature of these effects can exacerbate stress concentration. When the train passes over the bridge, it generates dynamic forces that act on the soil. The Geocells, while effective in stabilizing static loads, may not be as effective in dealing with these dynamic forces. The soil may undergo oscillations and vibrate within the confined region, amplifying the localized stress.

The confinement of the soil by Geocells can also lead to accumulated vertical displacement. As the train passes, the soil compresses but cannot expand laterally due to Geocells. This cumulative vertical displacement further contributes to stress concentration, as the soil cannot release the dynamic load efficiently, leading to higher accelerations. In the absence of Geocells, the dynamic loads from a high-speed train are distributed more uniformly across the soil-metal bridge crown. The soil can spread laterally, allowing for a broader distribution of these loads. However, the introduction of Geocells interrupts this distribution. While Geocells effectively confine the soil within their cells, the dynamic train loads cannot be evenly distributed across the entire bridge crown. This results in a concentrated load on the area directly above the crown, leading to localized stress concentration. The soil beneath the bridge crown has a certain degree of compressibility. When subjected to dynamic loads, it undergoes deformation. The confinement imposed by Geocells impedes this deformation, leading to the development of excess stresses within the soil. The resistance to deformation provided by the Geocells means that the soil cannot dissipate the dynamic load efficiently, and as a result, the stress is concentrated in a smaller area directly above the crown.

4.5.2.2 X-Direction Acceleration

Unlike the z-direction deformations, which primarily focus on the vertical stability of the bridge, geocell layers exhibit a distinct and positive influence on x-direction accelerations as shown in Figure 4.9. Let's delve deeper into how geocell layers enhance these accelerations and contribute to a more stable bridge structure. Geocell layers provide lateral confinement to the soil within the bridge structure. This confinement serves to stabilize the soil, limiting its lateral movement. In the absence of geocell layers, soil particles can shift and slide during the passage of a high-speed train, leading to unpredictable and often detrimental variations in accelerations. With geocell layers in place, the soil is effectively "held" in position, reducing its ability to move laterally. This enhanced stability ensures that the bridge remains resilient against the lateral forces generated by the train's motion. As a result, the bridge exhibits a more consistent and less erratic response in the x-direction, reducing the likelihood of extreme accelerations.

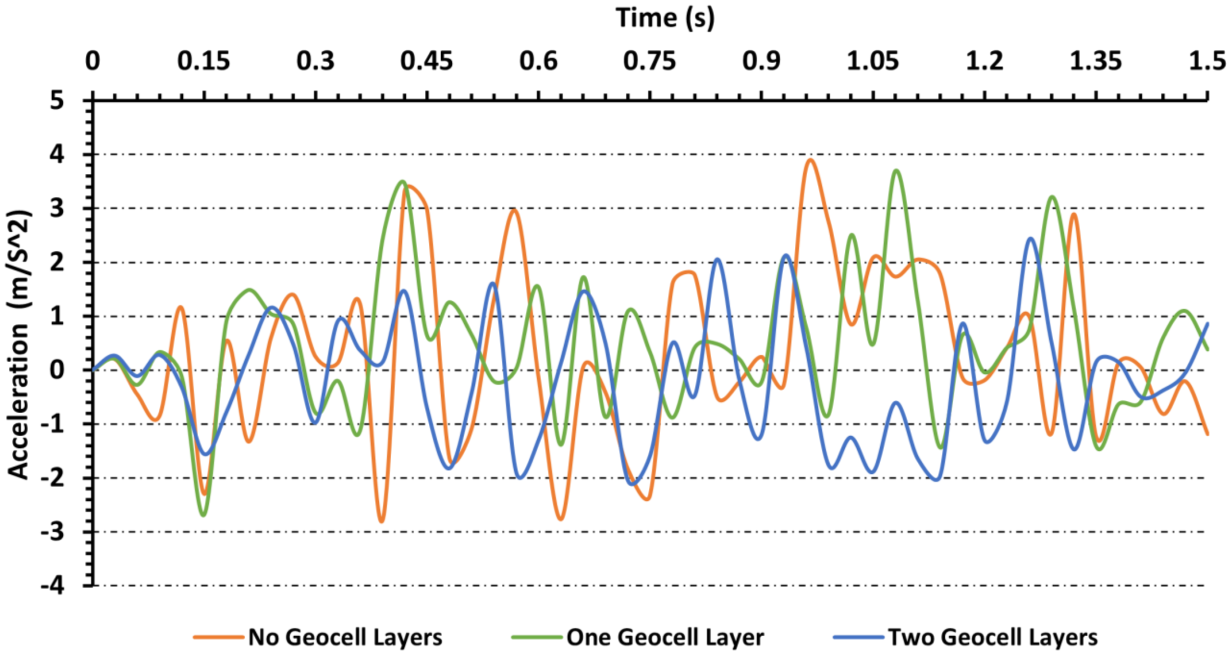

Figure 4.11 Crown Acceleration in X-direction as a function of time for a traveling train speed of 300km/h

In this scenario, where no geocell layers are employed, the bridge experiences a wide spectrum of acceleration. The maximum acceleration, observed at 3.76 m/s² at t=0.96 seconds, indicates a force in the same direction as the train's movement. In contrast, the minimum acceleration stands at -2.79 m/s² at t=0.39 seconds, signifying an opposing force, contrary to the train's motion. Incorporating a single geocell layer, the bridge displays a pattern akin to the case without geocell layers, albeit with notable distinctions. The maximum acceleration, recorded at 3.70 m/s² at t=1.08 seconds, is slightly lower, while the minimum acceleration is -2.68 m/s² at t=0.15 seconds. This suggests that the introduction of a geocell layer has a positive impact on mitigating positive and negative accelerations. In the third scenario, with two geocell layers, the bridge showcases maximum and minimum accelerations. The maximum acceleration, at 2.43 m/s² at t=1.26 seconds, remains positive, while the minimum is -2.05 m/s² at t=0.72 seconds. The presence of two geocell layers continues to provide stability to the bridge's acceleration behavior.

Comparing the case where single geocell layer is employed, to the case with no geocell layers, notable differences in acceleration patterns in the x-direction become apparent. The maximum acceleration experiences a marginal decrease, falling from 3.76 m/s² in to 3.70 m/s², representing a 1.59% reduction. This minor reduction suggests that the introduction of a single geocell layer has a modest impact on mitigating the peak positive acceleration, contributing to a slightly more stable bridge structure. On the other hand, the minimum acceleration exhibits a noteworthy improvement, decreasing from -2.79 m/s² to -2.68 m/s², marking a 3.94% rise. Overall, a single geocell layer can lead to improvements in minimizing negative accelerations while modestly affecting maximum accelerations, contributing to enhanced bridge stability. When comparing two geocell layers performance, with no geocell layers, striking differences in x-direction acceleration patterns emerge. The maximum acceleration experiences a significant decrease, declining from 3.76 m/s² to 2.43 m/s², marking a substantial 35.64% reduction. Additionally, the minimum acceleration in Case 3 exhibits a remarkable improvement, increasing from -2.79 m/s² to -2.05 m/s², indicating a substantial 26.52% increase. This underscores that two geocell layers reduce opposing forces acting against the train's motion, resulting in a bridge with more consistent and less erratic acceleration behavior.

4.5.2.3 Y-Direction Acceleration

In the analysis of the impact of geocell layers on acceleration patterns during the passage of high-speed trains, it becomes evident that these geosynthetic reinforcements enhance the stability of soil-metal bridges When examining the acceleration values for different scenarios as represented in Figure 4.10, the differences are striking. In the absence of geocell layers, the maximum acceleration reaches a substantial 13.31 m/s², signifying a notable force acting on the bridge structure. Additionally, the minimum acceleration dips to a significant -9.60 m/s², indicating substantial uncontrolled soil movement.

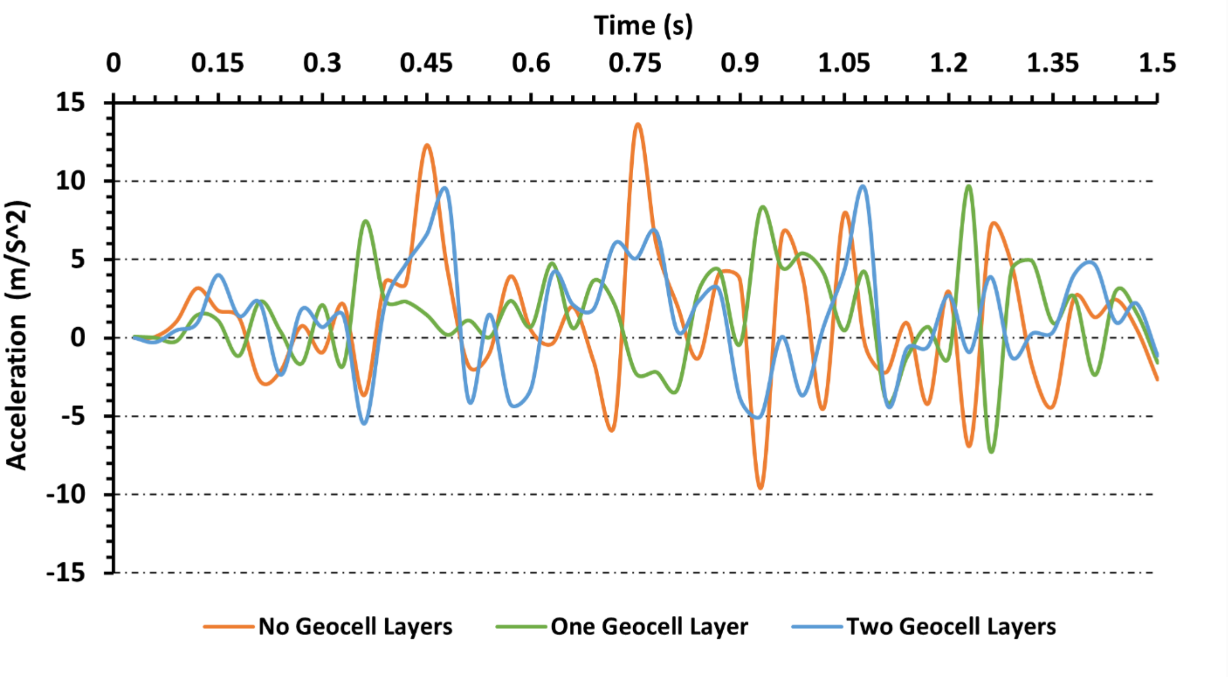

Figure 4.12 Crown Acceleration in Y-direction as a function of time for a traveling train speed of 300km/h

However, when one geocell layer is introduced, we observe a reduction in the maximum acceleration to 9.6203 m/s². This reduction of approximately 27.6% signifies a crucial stabilization effect. Meanwhile, the minimum acceleration, now at -7.2 m/s², also experiences a decrease, highlighting the geocell's efficacy in restraining soil movement. The most striking results are observed with two geocell layers. Here, the maximum acceleration further diminishes to 9.43 m/s², indicating a pivotal stabilizing effect provided by these geocells. Notably, the minimum acceleration is -5.48 m/s², reflecting a significant improvement compared to the case with no geocell layers.

To quantify the impact more precisely, the percentage reduction has been calculated in acceleration values concerning the scenario without geocell layers. The percentages reveal the extent of improvement. As for the one geocell layer, the maximum acceleration experiences a 27.6% reduction, and the minimum acceleration is reduced by 24.6%. On the other hand, the two Geocell Layers maximum acceleration sees a substantial 29.1% reduction, and the minimum acceleration is reduced by an even more impressive 43.1%.

4.5.3 Thrust Force

The observed differences in the performance of geocell under compaction loading and dynamic loading, particularly in the context of thrust forces on the crown of the soil-metal bridge during the passage of a train at 300 km/h, provide valuable insights into the behavior of geocell layers in mitigating these forces. The thrust forces, as indicated in the provided data, exhibit distinct patterns and relationships in the three cases; no geocell layers, one geocell layer, and two geocell layers.

Firstly, the analysis as shown in Figure 4.11 illustrates a consistent decrease in thrust forces as the number of geocell layers increases. This reduction is particularly noticeable in the initial thrust forces recorded before train passage. Without any geocell layers, the initial thrust force is 224.08 KN/m. With one geocell layer, this force decreases to 200.04 KN/m, and with two geocell layers, it further decreases to 198.45 KN/m. This trend aligns with expectations, as geocell layers are known to enhance the load-bearing capacity of soils, specially in static loading.

To provide a more comprehensive understanding of the patterns and relationships, it's essential to go through the time-dependent graph. Figure 4.11 includes thrust forces measured at different time intervals as the train passes over the bridge. Analyzing the behavior of thrust forces over time can shed light on the dynamic response of the geocell layers.

The first pattern is that the thrust forces in all cases tend to increase over time. This can be attributed to dynamic loading, as the train's passage generates cyclic loads that are transmitted to the soil bridge. However, it's crucial to highlight that this increase is less pronounced in cases with geocell layers. In the case with no geocell layers, the thrust force rises from -250.85 KN/m to -259.94 KN/m over the 1.5-second observation period. With one geocell layer, the increase is from -252.28 KN/m to -258.42 KN/m, and with two geocell layers, it rises from -246.52 KN/m to -252.71 KN/m.

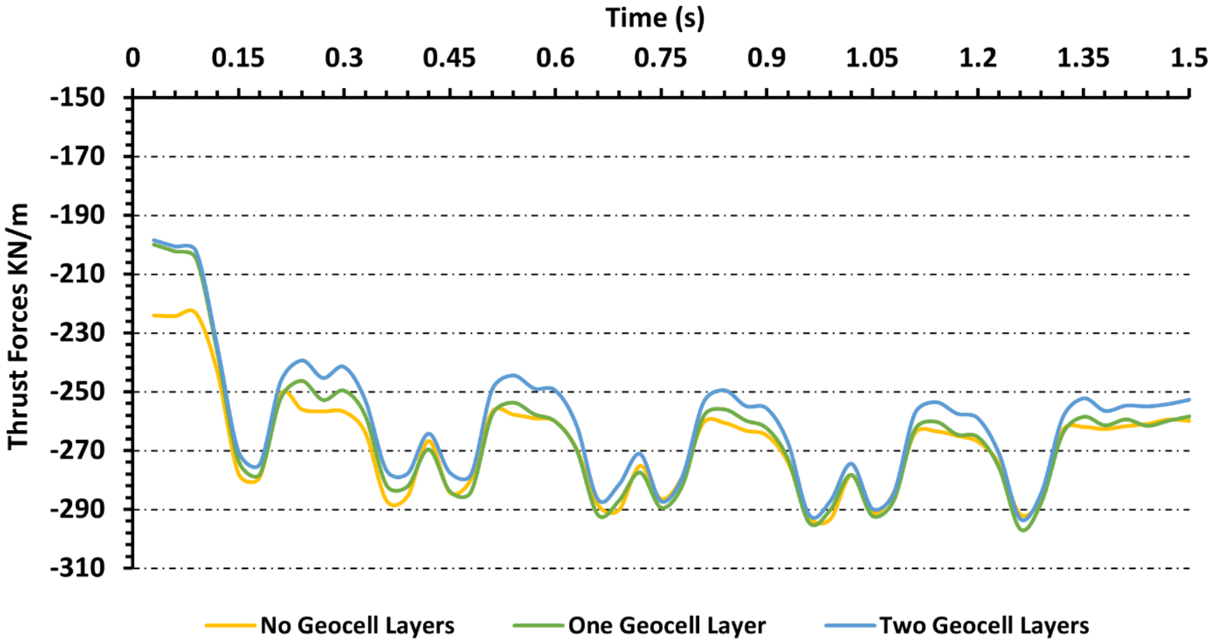

While thrust forces do increase with time in all cases, the rate of increase is slower in the presence of geocell layers. This reflects the ability of geocell layers to distribute and dissipate the dynamic loads more effectively, reducing the immediate impact and long-term consequences on the soil bridge. The extent of this reduction varies between cases with different numbers of geocell layers, but the consistent trend is the reduction in thrust forces. Expressing the reduction in thrust forces as percentages offers a more precise measurement of the improvement achieved with geocell layers. The percentages provide a clear indication of the relative decrease in thrust forces, allowing for straightforward interpretation. In the case with one geocell layer, a reduction of approximately 0.58% indicates that the presence of a single geocell layer has a modest but discernible effect in lowering thrust forces compared to the scenario with no geocell layer. Similarly, the larger reduction of approximately 2.78% with two geocell layers signifies a more substantial improvement. The maximum thrust force recorded in the no geocell layers case is -292.62 KN, while in the two geocell layers case, it is -293.34 KN. This indicates that the presence of geocell layers does not eliminate the possibility of high thrust forces, but it does limit their magnitude, as the maximum thrust force is lower in cases with geocell layers.

Geocell layers provide enhanced confinement to the underlying soil. This confinement increases the lateral restraint on soil particles, preventing them from shifting laterally during loading events. In compaction loading, the applied forces are relatively static and distributed over a larger area, allowing the geocell layers to effectively confine the soil, reducing lateral deformation. As a result, thrust forces are mitigated, and the initial thrust is significantly reduced. The second reason for the observed behavior lies in the frequency and cyclic nature of dynamic loading. When a train passes over the bridge at high speeds, it generates a series of dynamic loading cycles that induce cyclic stress and strain in both the soil and the geocell layers. This cyclic loading has a different impact on geocell layers compared to the steady and gradual compaction forces.

Geocell layers are effective at resisting static loads and maintaining their integrity under such conditions. However, the rapid and repetitive loading and unloading cycles during dynamic loading can lead to material fatigue in the geocell structure. Over time, this fatigue can result in reduced effectiveness in containing and distributing the loads, leading to increased thrust forces. Additionally, dynamic loading may lead to localized deformation or displacement of the geocell layers, causing uneven stress distribution and varying thrust forces. The third key reason for the observed behavior is the viscoelastic nature of geocell materials and their damping effect on dynamic loads. Geocell layers are typically composed of materials with viscoelastic properties, which means they exhibit a combination of elastic reversible and viscous irreversible behavior. This viscoelasticity allows geocell layers to deform and recover under static loads, effectively distributing the forces. However, under dynamic loading, the damping effect becomes more prominent. As dynamic loads are applied to the geocell layers, the material undergoes repeated deformation and recovery cycles. The viscous component of the geocell material dissipates a portion of the dynamic energy, reducing the magnitude of the transmitted forces. While this damping effect can be beneficial in mitigating the impact of dynamic loads, it also contributes to the observed behavior of geocell layers performing better in compaction loading, where static forces predominate.

4.6 Conclusion

This study aimed to scrutinize the intricate interaction between high-speed trains and soft soil, specifically assessing the effectiveness of geocell reinforcement. The investigation focused on the substantial forces and vibrations imposed on the ground as trains, traveling at speeds of 300 km/h. A methodical examination was imperative to comprehend these dynamics thoroughly. Employing a multifaceted approach, three models were explored: one lacking geocell reinforcement, one strengthened with a single layer of Honeycomb-Geocell, and a third model fortified with two layers of Honeycomb-Geocell. This approach served as our navigational guide through unexplored scientific terrain.

The finding of the research was the unanticipated escalation in crown deformation upon the introduction of geocell reinforcement. This deviation from conventional expectations challenged a well-established belief in civil engineering, where geocell reinforcement had been deemed a dependable solution for mitigating deformation in soft soils subjected to dynamic loads. This unexpected revelation prompted a deeper investigation into the underlying mechanisms responsible for this counterintuitive phenomenon. The intricacies of understanding the dynamics of high-speed trains on soft soil are intricately tied to the distinctive properties of these soils. Soft soils, characterized by low shear strength and high compressibility, are particularly susceptible to deformation under the influence of dynamic loads and vibrations. The inadequate shear strength renders the soil incapable of effectively supporting the dynamic loads imposed by high-speed trains, resulting in consequential ground movements and vibrations within the soft soil.

Geocell structures, designed to confine and stabilize the soil, are engineered to restrict lateral soil movement and control deformation effectively. However, in this specific analysis, their limitations came to the forefront. Instead of successfully containing the soil, the extreme compressibility of the soft soil and the high dynamic loads generated by the trains exceeded the capacity of geocell reinforcement. This scenario resulted in higher displacement and, paradoxically, exacerbated deformation. The study uncovered a fundamental truth - geocell reinforcement is not a one-size-fits-all solution. Instead, it must be judiciously applied, taking into account specific soil properties and loading conditions. This newfound knowledge has implications that extend far beyond the confines of the research, reshaping the way civil engineers approach soft soil dynamics. One of the key insights unearthed was the phenomenon of stress concentration directly above the soft soil crown. When geocell structures failed to confine the soil effectively, stress concentrated in this area, culminating in higher deformation on the crown itself. The concentration of stress above the soft soil crown was intricately associated with the structural failure of geocells, introducing an additional layer of complexity to the entire scenario. This study emphasized the role of stress concentration as a contributing factor to the aggravation of deformation following the introduction of geocell reinforcement.

The quantification of deformation data elucidated the magnitude of the unanticipated increase in deformation upon the introduction of geocell reinforcement. The numerical analysis portrayed a distinct scenario, where a single geocell layer yielded a maximum deformation approximately 70.71% higher than the scenario devoid of geocell. Augmenting the complexity, the inclusion of two geocell layers further exacerbated the situation, resulting in a remarkable 79.12% increase in deformation compared to the geocell-absent case. These quantitative findings accentuate the profound implications derived from the research. The dislocation of geocell elements and the concentration of deformations beneath the ballast layer challenged the conventional paradigm of geocell reinforcement in mitigating deformation in soft soils subjected to dynamic train loads.

The culmination of the research necessitates a reassessment of geocell reinforcement strategies in scenarios involving soft soils and high-speed train loads. The unforeseen consequence of geocell reinforcement intensifying deformation underscores the imperative for a nuanced and context-specific approach. The design parameters of geocells, encompassing cell size, height, and material properties, must undergo optimization tailored to specific soil conditions and loading requirements. The erstwhile universal approach is no longer defensible, and the findings underscore the pivotal role of customization and precision. A crucial takeaway from our research is the imperative to account for the dynamic nature of loading. Traditional geocell reinforcement strategies have historically been conceived with static loads in mind. However, the introduction of dynamic forces by high-speed trains injects a new stratum of complexity. The rapid motion, vibrations, and ground movements induced by these trains engender a dynamic environment with a profound impact on soft soil.

CHAPTER 5 CONCLUSION

The role of soil cover depth in mitigating deformations within Soil-Metal Bridges (SMBs) has been examined across various high-speed train velocities (100 km/h to 300 km/h). Deeper soil cover consistently leads to reduced deformations, offering crucial insights for SMB design under diverse conditions. The observed correlation between higher train speeds and increased deformations emphasizes the need for meticulous consideration of train speed in SMB design, particularly as global high-speed rail networks expand.

Exploring the dynamics of deformations during high-speed train passage, the study reveals complex patterns of crown deformation responsive to varying train speeds and soil cover depths. These patterns provide nuanced insights into the mechanical responses of SMBs to dynamic loading, essential for predictive modeling and optimizing structural performance.

Shifting attention to geocell reinforcement in soft soil dynamics, the examination involves three models: one without geocell reinforcement, one with a single layer, and another with two layers of Honeycomb-Geocell. The unexpected revelation challenges prevailing beliefs as geocell reinforcement unexpectedly exacerbates crown deformation.

Understanding high-speed train dynamics on soft soil is intricately linked to the distinctive properties of these soils, characterized by low shear strength and high compressibility. Geocell structures designed for soil confinement and stabilization exhibit limitations in this context, resulting in increased displacement and exacerbated deformation.

The realization that geocell reinforcement is not a universally applicable solution emphasizes the need for customization and precision in geocell design, reshaping the approach adopted by civil engineers in addressing the complexities of soft soil dynamics. Stress concentration directly above the soft soil crown emerges as a contributing factor to the exacerbation of deformation following geocell reinforcement.

Quantitative analysis underscores these findings, with a single geocell layer resulting in a maximum deformation approximately 70.71% higher than scenarios without geocell. Introducing two geocell layers further amplifies deformation by 79.12%, highlighting the profound implications of this research.

In conclusion, these integrated findings contribute to a comprehensive understanding of the challenges and dynamics inherent in SMBs subjected to high-speed train loads and the limitations of geocell reinforcement in soft soil scenarios. They advocate for a paradigm shift in engineering practices, urging a nuanced and bespoke approach for the resilient structural design and safety of these critical infrastructures.

REFERENCES

Aagah, O., & Aryannejad, S. 2014. Dynamic analysis of soil-steel composite railway bridges Master of Science. KTH Royal Institute of Technology, Sweden.

AASHTO, 2012. LRFD bridge design specifications. Washington, DC: American Association of State Highway and Transportation Officials.

Abdel-Sayed, G. Salib, R, S. Minimum depth of soil cover above soil-steel bridges. 2002. Journal of geotechnical and geoenvironmental engineering, American Society of Civil Engineers. DOI: 10.1061/ASCE1090-02412002128:8672.

Andersson, H. Sundquist, and R. Karoumi, "FULL SCALE TESTS AND STRUCTURAL EVALUATION OF SOIL-STEEL FLEXIBLE CULVERTS FOR HIGH-SPEED RAILWAYS," in II European Conference, BURIED FLEXIBLE STEEL STRUCTURES", 2012.

Asha M. Nair, G. Madhavi Latha. Large Diameter Triaxial Tests on Geosynthetic-Reinforced Granular Subbases, 2015, Journal of Materials in Civil Engineering,04014148-27-4. doi:10.1061/ASCEMT.1943-5533.0001088

ASTM D2487 2006 Standard practice for classification of soils for engineering purposes Unified soil classification system. American Society for Testing Materials ASTM International, West Conshohocken, Pennsylvania.

ASTM D698-00ae1 2007 Standard test methods for laboratory compaction characteristics of soil using standard effort 12,400 ft-lbf/ft3 600 kN-m/m3. American Society for Testing Materials ASTM International, West Conshohocken, Pennsylvania.

ASTM. 2017. A796/A796M. Standard practice for structural design of corrugated steel pipe, pipe-arches, and arches for storm and sanitary sewers and other. ASTM international, West Conshohocken, Pa. doi:10.1520/A0796_A0796M-17A.

Bagli, S.P. A tryst with geosynthetics. Indian Geotech. J. 2022, 52, 1003–1053.

Bakht, B. 1980, August. Live load testing of soil-steel structures. SRR-80-4. Ontario Ministry of Transportation and Communication, Policy Planning and Research Division.

Bathe, K.J. 1982. Finite element analysis in engineering analysis. Prentice-Hall, New Jersey.

Bathurst, R.J.; Karpurapu, R. Large-Scale Triaxial Compression Testing of Geocell-Reinforced Granular Soils. Geotech. Test. J.1993, 16, 296–303.

Bayoglu Flener E. Testing the response of box-type soilsteel structures under static service loads. Journal of Bridge Engineering. 2010;151:90-97.

Bayoglu Flener, E. Soil-structure interaction for integral bridges and culverts. 2004. Royal Institute of Technology – Division of structural design and bridges. Stockholm, Sweden. Licentiate thesis.

Beben, D. Dynamic amplification factors of corrugated steel plate culverts. 2012. Elsevier, Science Direct.

Biabani, M.M.; Ngo, N.T.; Indraratna, B. Performance evaluation of railway subballast stabilised with geocell based on pull-out testing. Geotext. Geomembr. 2016, 43, 569–581.

Binquet J, Lee LK 1975 Bearing capacity tests on reinforced earth slabs. J Geotech Eng Div ASCE 10112:1241–1255.

Biswas A, Murali Krishna A, Dash SK 2013 Influence of subgrade strength on the performance of geocell-reinforced foundation systems. Geosynth Int 206:376–388.

Burakbey Davarci, Murat Ornek & Yakup Turedi 2014 Model studies of multiedge footings on geogrid-reinforced sand, European Journal of Environmental and Civil Engineering,18:2, 190-205, DOI: 10.1080/19648189.2013.854726

Bush DI, Jenner CG, Bassett RH 1990 The design and construction of geocell foundation mattress supporting embankments over soft ground. Geotext Geomembr 9:83–98.

Chen RH, Wu CP, Huang FC, Shen CW 2013 Numerical analysis of geocell-reinforced retaining structures. Geotext Geomembr 39:51–62. https://doi.org/10.1016/j.geotexmem.2013.07.003

Corrugated steel pipe institute CSPI and American Iron and Steel Institute, 2007. Handbook of steel drainage & highway construction products. 2nd ed. Ontario: American Iron and Steel Institute.

Cowland JW, Wong SCK 1993 Performance of a road embankment on soft clay supported on a geocell mattress foundation. Geotext Geomembr 128:687–705.

CSA Canadian Standards Association, 2014. Canadian Highway Bridge Design Code 6-14. 11th ed. Canada: CSA Canadian Standards Association.

D.I. Bush, C.G. Jenner, R.H. Bassett, the design and construction of geocell foundation mattresses supporting embankments over soft grounds, Geotext. Geomembr. 9 1 1990 83–98.

Damian Beben. Corrugated Steel Plate Culvert Response to Service Train Loads Journal of Performance of Constructed Facilities Volume 28, Issue 2. https://doi.org/10.1061/ASCECF.1943-5509.0000422

Dash SK, Rajagopal K, Krishnaswamy NR 2004 Performance of different geosynthetic reinforcement materials in sand foundations. Geosynth Int 11:1

Dash, S. K. 2012.“Effect of geocell type on load carrying mechanisms ofgeocell-reinforced sand foundations.”Int. J. Geomech.12 5: 537–548. https://doi.org/10.1061/ASCEGM.1943-5622.

Dash, S.K. Influence of relative density of soil on performance of geocell-reinforced sand foundations. J. Mater. Civ. Eng. 2010, 22, 523–528.

Dash, S.K.; Krishnaswamy, N.R.; Rajagopal, K. Bearing capacity of strip footings supported on geocell-reinforced sand. Geotext. Geomembr. 2001, 19, 235–255.

Dash, S.K.; Rajagopal, K.; Krishnaswamy, N.R. Behavior of geocell-reinforced sand beds under strip loading. Can. Geotech. J. 2007, 43, 905–916

Dash, S.K.; Reddy, P.D.T.; Raghukanth, S.T.G. Subgrade modulus of geocell-reinforced sand foundations. Proc. Inst. Civ. Eng. Ground Improv. 2008, 160, 79–117.

Davarifard, S.; Tafreshi, S.M. Plate load tests of multi-layered geocell reinforced bed considering embedment depth of footing. Procedia Earth Planet. Sci. 2015, 15, 105–110.

Dean R, Lothian E 1990 Embankment construction problems over deep variable soft deposits using a geocell mattress. Proceedings of performance of reinforced soil structures, British Geotechnical Society, London UK. pp 443–447.

Du, G. Pettersson, L., and Karoumi, R., 2018. Soil-steel composite bridge: An alternative design solution for short spans considering ICA. Journal of Cleaner Production. 189,647-661.

Du. G. 2015. Life cycle assessment of bridges, model development and case studies [PhD thesis]. KTH Royal Institute of Technology.

Duncan JM . Behaviour and design of longspan metal culvert structures. J. Geotech. Eng. Div. Proc. Am. Soc. Civil Eng. 1979; 105GT3: 399-418.

Duncan JM, Chang CY 1970 Non-linear analysis of stress and strain in soils. J Soil Mech Found Div 96:1629–1653

Duncan JM, Drawsky RH. Design Procedure for Flexible Metal Culvert Structures. Report No UCB /GT/ 83-02, 2nd edn. Department of Civil Engineering, University of California: Berkeley, CA, 1983.

Duncan JM. Soil-Culvert Interaction Method for Design of Metal Culverts. Transportation Research Record 678 Tolerable Movement of Bridge Foundations, Sand Drains, K-Test, Slopes, and Culverts. Transportation Research Board, National Academy of Sciences: Washington, DC, 1978.

Duncan, J.M., 1979. Behavior and design of long-span metal culverts. Journal of the Geotechnical Engineering Division, 105 3, 399 418.

Duncan, J.M., Chang, C.Y. 1970. Nonlinear analysis of stress and strain in soil. ASCE J. of the Soil Mech. And found. Div., 96, 1629–1653.

El-Sawy, K, M. Three-dimensional modeling of soil-steel culverts under the effect of truckloads. 2003. Elsevier, Science Direct. DOI: 10.1016/S0263-82310300022- 3.

Elshimi TM, Moore ID. Modeling the Effects of Backfilling and Soil Compaction beside Shallow Buried Pipes. J Pipeline Syst Eng Pract 2013; 44: 04013004.

Esmaeili, M., Zakeri, J. & Abdulrazagh, P. Minimum depth of soil cover above long-span soil-steel railway bridges. Int J Adv Struct Eng 5, 7 2013. https://doi.org/10.1186/2008-6695-5-7.

Eurocode 1: Actions on structures - Part 2: Traffic loads on bridges [Authority: The European Union Per Regulation 305/2011, Directive 98/34/EC, Directive 2004/18/EC], EN 1991-2 2003

European Committee of Standardization, Translated by Swedish Standards Institute. SS-EN 1991-2: Actions on structures – Part 2: Traffic loads on bridges. 2011. Swedish Standards institute. 1st Edition. Stockholm, Sweden.

Ferreira, F.B., Vieira, C.S., Lopes, M.L., 2015. Direct shear behaviour of residual soil–-geosynthetic interfaces – influence of soil moisture content, soil density and geosynthetic type. geosynthetics Int 22 3, 257–272.

Field testing of a Long-Span arch steel culvert Railway Bridge over Skivarpsån, Sweden. Part III - Report 91. 2003. Royal Institute of Technology Division of structural design and bridges. Stockholm, Sweden.

Flener, E. B., and R. Karoumi. 2009. "Dynamic testing of a soil-steel composite railway bridge." Eng. Struct. 31 12: 2803–2811. https://doi.org/10.1016/j.engstruct.2009.07.028.

Garcia, R.S.; Neto, J.A. Stress-dependent method for calculating the modulus improvement factor in geocell-reinforced soil layers. Geotext. Geomembr. 2021, 48, 145–157.

Gedela, R.; Karpurapu, R. Influence of pocket shape on numerical response of geocell reinforced foundation systems. Geosynth. Int. 2021, 28, 327–337.

Hegde, A.; Sitharam, T.G. 3-Dimensional numerical modelling of geocell reinforced sand beds. Geotext. Geomembr. 2015, 42, 171–181.

Hegde, A.; Sitharam, T.G. Experiment and 3D-numerical studies on soft clay bed reinforced with different types of cellular confinement systems. Transp. Geotech. 2017, 10, 73–84.

Hegde, A.; Sitharam, T.G. Experimental and numerical studies on footings supported on geocell reinforced sand and clay beds. Int. J. Geotech. Eng. 2013, 7, 345–353

Henkel, D.J.; Gilbert, G.D. The effect of the rubber membrane on the measured triaxial compression strength of clay specimens. Geotechnique 1951, 3, 20–29.

Hicher, P. 1996. Elastic properties of soils. J Geotech Eng ASCE, 1228:641–648. 116

Islam Ezzeldin, Hany El Naggar, Numerical Modelling of Induced Stresses in Buried Corrugated Metal Structures due to Compaction Efforts, Transportation Geotechnics, Volume 32, 2022, 100706, ISSN 2214-3912, https://doi.org/10.1016/j.trgeo.2021.100706.

J.O. Avesani Neto, B.S. Bueno, and M.M. Futai A bearing capacity calculation method for soil reinforced with a geocell. Geosynthetics International 2013 20:3, 129-142

Jones CJFP 1996 Earth reinforcement and soil structures. Thomas Telford Publication, London.

k. j. Bathe, Finite Element Procedures in Engineering Analysis, Prentice-Hall, 1982.

K.M. El-Sawy, Three-dimensional modeling of soil-steel culverts under the effect of truckloads, Thin-Walled Struct. 41 2003 747–768, http://dx.doi.org/10. 1016/S0263-82310300022-3.

Kargar, M.; Mir Mohammad Hosseini, S.M. Effect of reinforcement geometry on the performance of a reduced-scale strip footing model supported on geocell-reinforced sand. Sci. Iran. 2017, 24, 96–109.

Khalaj, O.; Moghaddas Tafreshi, S.N.; Mask, B.; Dawson, A.R. Improvement of pavement foundation response with multi-layers of geocell reinforcement: Cyclic plate load test. Geomech. Eng. 2015, 9, 373–395.

Kondner, R.L. 1963. A hyperbolic stress strain formulation for sands. 2. Pan. Am. ICOSFE Brazil, 1, 289–324.

Krishnaswamy, N.R.; Rajagopal, K.; Latha, G.M. Model studies on geocell supported embankments constructed over a soft clay foundation. Geotech. Test. J. 2000, 23, 44–49.

Kunecki B. Field Test and Three-Dimensional Numerical Analysis of Soil–Steel Tunnel during Backfilling. Transportation Research Record. 2014;24621:55-60.

Lal, D.; Sankar, N.; Chandrakaran, S. Behaviour of square footing on sand reinforced with coir geocell. Arab. J. Geosci. 2017, 10, 345.

Lambert S, Nicot F, Gotteland P 2011 Uniaxial compressive behaviour of scrapped tire and sand filled wire netted geocell with a geotextile envelop. Geotext Geomembr 29:483–490.

Latha GM 2000 Investigations on the behaviour of geocell supported embankments. Ph.D Thesis, Indian Institute of Technology Madras, Chennai, India.

Latha GM, Vidya SM 2007 Effects of reinforcement form on the behaviour of geosynthetic reinforced sand. Geotext Geomembr 251:23–32.

Latha, G.M. Geocells for transportation geotechnical applications. Indian Geotech. J. 2021, 50, 602–613.

Latha, G.M.; Somwanshi, A. Effect of reinforcement form on the bearing capacity of square footings on sand. Geotext. Geomembr. 2009, 27, 399–412.

Lekshmi S, Prabhu SS, Pratibha R, Babu GS 2016 Behavior of geocell-reinforced granular base under repeated loading. Transp Geotech 9:17–30

Leshchinsky, B.; Ling, H. Effects of geocell confinement on strength and deformation behavior of gravel. J. Geotech. Geoenvironment. Eng. 2013, 120, 339–351.

Łydżba D, Różański A, Sobótka M, Stefaniuk D, Chudy G, Wróblewski T. Mechanical behaviour of soil-steel structure subjected to live loads and different water conditions. Arch Inst Civ Eng. 2017;23:163-174.

M.S. Khedkar, J.N. Mandal,Pullout behaviour of cellular reinforcements, Geotextiles and Geomembranes,Volume 27, Issue 4,2009, Pages 262-271,ISSN 0266-1144, https://doi.org/10.1016/j.geotexmem.2008.12.003.

Machelski C, Antoniszyn G. Load rate of the circumferential sector of soil-steel bridge structures. Archives of Civil and Mechanical engineering. 2005;54:85-102.

Machelski C. Dependence of deformation of soil-shell structure on the direction of load passage. Roads and Bridges 2014;13:223-233.

Madhavi Latha, G.; Dash, S.K.; Rajagopal, K. Equivalent continuum simulations of geocell reinforced sand beds supporting strip footings. Geotech. Geol. Eng. 2008, 26, 387–398.

Maheshwari, P.; Babu, G.S. Nonlinear deformation analysis of geocell reinforcement in pavements. Int. J. Geomech. 2017, 17, 03916043.

Mahgoub A, El Naggar H. Coupled TDA-geocell stress bridging system for metal pipes. J Geotech Geoenviron Eng, ASCE. 2020;1467. DOI: 10.1061/ASCEGT.1943-5606.0002279.

Mai, V. T., Moore, I. D., & Hoult, N. A. 2014b. Performance of two-dimensional analysis: Deteriorated metal culverts under surface live load. Tunelling and Underground Space Technology, 42, 152-160. doi: 10.1016/j.tust.2014.02.015

Maleska T, Bęben D. Behaviour of the soil-steel bridge with different soil cover height under seismic excitations. Bridge Maintenance, Safety, Management, Life-Cycle Sustainability and Innovations. CRC Press; 2021;1801-1808.

Maleska T, Bęben D. Numerical analysis of a soil-steel bridge during backfilling using various shell models. Engineering Structures. 2019;196:109358.

Mańko Z, Bęben, D. Research on steel shell of a road bridge made of corrugated plates during backfilling. Journal of Bridge Engineering. 2005;105:592-603.

Manual SUDAS. Statewide Urban Design And Specifications. Institute of Transportation: Iowa State University, USA; 2017.

McGrath TJ, Selig ET, Webb MC, Zoladz GV. Pipe interaction with the backfill envelope. FHWA-RD-98-191 1999.

Mehdipour, I.; Ghazavi, M.; Moayed, R.Z. Numerical study on stability analysis of geocell reinforced slopes by considering the bending effect. Geotext. Geomembr. 2013, 37, 23–34.

Mellat, P. Dynamic analysis of soil-steel composite bridges for high speed railway traffic. 2012. Royal Institute of Technology – Division of structural engineering and bridges. Stockholm, Sweden.

Meyer, K.G. Managing Degraded off-Highway Vehicle Trails in Wet, Unstable, and Sensitive Environments; USDA Forest Service, Technology and Development Program, Missoula Technology and Development Center: Missoula, MT, USA, 2002.

Mhaiskar, S.Y.; Mandal, J.N. Investigations on soft clay subgrade strengthening using geocells. Constr. Build. Mater. 1996, 10, 281–286.

Mitchell JK, Kao TC, Kavazanijiam E 1979 Analysis of grid cell reinforced pavement bases. Technical report GL-79-8, U.S. Army waterways experiment station, Vicksburg

Mohsen Kargar & S. Majdeddin Mir Mohammad Hosseini 2018 Influence of reinforcement stiffness and strength on load-settlement response of geocell-reinforced sand bases, European Journal of Environmental and Civil Engineering, 22:5, 596-613, DOI: 10.1080/19648189.2016.1214181

Muthukumar, S.; Sakthivelu, A.; Shanmugasundaram, K.; Mahendran, N.; Ravichandran, V. Performance assessment of square footing on jute geocell-reinforced sand. Int. J. Geosynth. Ground Eng. 2019, 5, 25.

OHBDC. 1991. Ontario highway bridge design code. Ministry of Transportation of Ontario, Downsview, Ont.

Paul J 1988 Reinforced soil system in embankments-construction practices. In: Proceedings of the international geotechnical symposium on practice of earth reinforcement, Fukuoka, Japan, October, pp 461–466.

Pettersson L, Flener EB, Sundquist H. Design of soil–steel composite bridges. Structural Engineering International. 2015; 252:159-172.

Pettersson, L. and Sundquist, H., 2014. Design of soil steel composite bridges. 5th ed. Stockholm: KTH Royal Institute of Technology.

Pettersson, L., Flener, E.B., and Sundquist, H., 2015. Design of soil steel composite bridges. Structural Engineering International, 25 2, 159-172.

Pipinato. A. and De Miranda, M. 2016. Chapter 10: Steel and composite bridges. In: A Pipinato, ed. Innovative Bridge Design Handbook. Construction, Rehabilitation and Maintenance. Oxford: Butterworth-Heinemann. 247-271.

Pittino G, Golser J. Structural plate steel underpasses during backfilling-how to minimize the bending moment. FLAC and Numerical Modeling in Geomechanics. 2006:001-007.

Pokharel, S.K. Experimental Study on Geocell-Reinforced Bases under Static and Dynamic Loading. Ph.D. Thesis, University of Kansas, Lawrence, KS, USA, 2010.

Rafal F. Obrzud, Andrzej Truty, THE HARDENING SOIL MODEL - A PRACTICAL GUIDEBOOK, Z Soil.PC 100701 report revised 21.10.2018Schanz, T., Vermeer, P.A. 1998. Special issue on pre-failure deformation behaviour of geomaterials. Géotechnique, 48, 383–387.

Rajagopal K, Krishnaswamy NR, Latha GM 1999 Behaviour of sand confined with single and multiple geocells. Geotext Geomembr 17:171–184

Rajagopal, K.; Krishnaswamy, N.R.; Latha, G.M. Behavior of sand confined with single and multiple geocells. Geotext. Geomembr. 1999, 17, 171–184.

Rea, C.; Mitchell, J.K. Sand Reinforcement Using Paper Grid Cells; ASCE Spring Convention and Exhibit: Pittsburgh, PA, USA, 1978; pp. 24–28.

S.N. Moghaddas Tafreshi, P. Sharifi, A.R. Dawson, Performance of circular footings on sand by use of multiple-geocell or -planar geotextile reinforcing layers, Soils and Foundations, Volume 56, Issue 6, 2016, Pages 984-997, ISSN 0038-0806, https://doi.org/10.1016/j.sandf.2016.11.004.

Safi, M., 2012. LCC applications for bridges and integration with BMS [Licentiate thesis]. KTH Royal Institute of Technology.

Sanat K. Pokharel, Jie Han, Dov Leshchinsky, Robert L. Parsons, Izhar Halahmi, Investigation of factors influencing behavior of single geocell reinforced bases under static loading, Geotextiles and Geomembranes, Volume 28, Issue 6, 2010, Pages 570-578, ISSN 0266-1144, https://doi.org/10.1016/j.geotexmem.2010.06.002.

Saride, S.; Gowrisetti, S.; Sitharam, T.G.; Puppala, A.J. Numerical simulation of geocell-reinforced sand and clay. Proc. Inst. Civ. Eng. Ground Improv. 2009, 161, 185–198.

Schanz, T., Vermeer, P.A., Bonnier, P.G.: Formulation and Verification of the Hardening Soil Model. In: Brinkgreve ed. Beyond 2000 in Computational Geotechnics, pp. 281–290. Balkema, Rotterdam 1999

Sezen, H.; Yeau, K.Y.; Fox, P.J. In-Situ load testing of corrugated steel pipe-arch culverts. J. Perform. Constr. Facil. 2008, 22, 245–252, https://doi.org/10.1061/ASCE0887-3828200822:4245

Sherin, K.S.; Chandrakaran, S.; Sankar, N. Effect of geocell geometry and multi-layer system on the performance of geocell reinforced sand under a square footing. Int. J. Geosynth. Ground Eng. 2017, 3, 20.

Shin, E.C.; Kang, H.H.; Park, J.J. Reinforcement efficiency of bearing capacity with geocell shape and filling materials. KSCE J. Civ. Eng. 2017, 21, 1627–1655.

Sireesh, S.; Sitharam, T.G.; Dash, S.K. Bearing capacity of circular footing on geocell–sand mattress overlying clay bed with void. Geotext. Geomembr. 2009, 27, 89–98.

Sitharam, T.G.; Sireesh, S. Effects of base geogrid on geocell-reinforced foundation beds. Geomech. Geoengin. Int. J. 2006, 1, 207–216.

Sitharam, T.G.; Sireesh, S.; Dash, S.K. Model studies of a circular footing supported on geocell-reinforced clay. Can. Geotech. J.2005, 41, 693–703.

Sobótka M, Łydżba D. Live load effect in soil-steel flexible culvert: role of apparent cohesion of backfill. Eur J Environ Civ Eng. 2019:1-15.

Sobótka M. Numerical simulation of hysteretic live load effect in soil-steel bridge. Stud Geotech Mech. 2014; 361:103-109.

Sobótka M. Shape optimization of flexible soil-steel culverts taking non-stationary loads into account. Structures. 2020; 23:612-620.

Soos von, P., 2001. Properties of Soil and Rock in German, Grundbau- taschenbuch, vol. 1, 6th Ed., Ernst and Son, Berlin, pp. 117–201.

Sutubadi, H, M. Khatibi, R, B. Effect of soil propertieson stabilityof soil-steel culverts. Turkish journal of Engineering & environmental science. DOI: 10.3906/muh1203-11

Tafreshi SNM, Khalaj O, Dawson AR 2013 Pilot-scale load tests of a combined multilayered geocell and rubber-reinforced foundation. Geosynth Int 203:143–161.

Tafreshi, S.M.; Dawson, A.R. Comparison of bearing capacity of a strip footing on sand with geocell and with planar forms of geotextile reinforcement. Geotext. Geomembr. 2010, 28, 72–114.

Tafreshi, S.M.; Shaghaghi, T.; Mehrjardi, G.T.; Dawson, A.R.; Ghadrdan, M. A simplified method for predicting the settlement of circular footings on multi-layered geocell-reinforced non-cohesive soils. Geotext. Geomembr. 2015, 42, 332–343.

Taleb B, Moore ID. Metal culvert response to earth loading performance of two-dimensional analysis.” Transportation Research Record 1656, Transportation Research Board, Washington, DC 1999: 25–36.

Taleb, B., and Moore, I. D. 1999. “Metal culvert response to earth loading performance of two-dimensional analysis.” Transportation Research Record 1656, Transportation Research Board, Washington, DC, 25–36.

Tanyu BF, Aydilek AH, Lau AW, Edil TB, Benson CH 2013 Laboratory evaluation of geocell-reinforced gravel subbase over poor subgrades. Geosynth Int 202:46–71.

Thallak, S.G.; Saride, S.; Dash, S.K. Performance of surface footing on geocell-reinforced soft clay beds. Geotech. Geol. Eng. 2007, 25, 499–514.

Truty, and R. F. Obrzud, "The hardening soil model-a practical guide book". Technical Report ZSoil.PC 100701, Zace Services Ltd , p. 216, 2018.

Vidal H 1969 The principle of reinforced earth. Highw Res Rec 282.

Viggiani, G. and Atkinson, J. 1995. Stiffness of fine-grained soil at very small strain. G´eotechnique, 452:249–265. 93, 116, 117, 148

Wadi A, Pettersson L, Karoumi R. Flexible culverts in sloping terrain: Numerical simulation of soil loading effects. Eng Struct. 2015; 101:111-124.

Wadi A. Soil-Steel Composite Bridges: Research advances and application. Doctoral dissertation: Kungliga tekniska högskolan; 2019.

Wang, G.Y.; Zhang, J.P.; Zhao, J.W. Numerical analysis of geocell protective slope stability. Appl. Mech. Mater. 2013, 352, 505–610.

WEBB, SELIG, SUSSMANN, MCGRATH Field Tests of a Large-Span Metal Culvert. TRANSPORTATION RESEARCH RECORD 1653. Paper No. 99-0425

Webster, S.L.;Watkins, J.E. Investigation of Construction Techniques for Tactical Bridge Approach Roads across Soft Ground; US Waterways Experiment Station: Vicksburg, MS, USA, 1977; Volume 2.

White L H, Layer P J. The Corrugated Metal Conduit as A Compression Ring. Highway Research Board. Proceedings of the 29th Annual Meeting, Washington, D.C. USA, 1960 pp 389–97.

White L, H. and Layer P, J., 1960. The corrugated metal conduit as a compression ring. Highway Research Board Proceedings, 39, 389-397.

Yang, X. Numerical Analyses of Geocell-Reinforced Granular Soils under Static and Repeated Loads. Ph.D. Thesis, University of Kansas, Lawrence, KS, USA, 2010.

Yeau, Y, K. Sezen, H. Fox, J, P. Load performance of in situ corrugated steel highway culverts. 2009. Journal of performance of constructed facilities, American Society of Civil Engineers. DOI: 10.1061/ASCE0887- 3828200923:132.

Yeau, Y, K. Sezen, H. Fox, J, P. Simulation of behavior of in-service metal culverts. 2013. Journal of pipeline systems engineering and practice, American Society of Civil Engineers. DOI: 10.1061/ASCEPS.1949-1204.0000158.

Zhang L, Zhou S, Zhao H, Deng Y 2018 Performance of geosynthetic-reinforced and pile-supported embankment with consideration of soil arching. J Eng Mech 14412:06018005

Zhang, L.; Zhao, M.; Zou, X.; Zhao, H. Deformation analysis of geocell reinforcement using Winkler model. Comput. Geotech. 2009, 36, 977–983.